# A COMPARATIVE STUDY ON ANALYTICAL MODELLING OF BONDWIRES FOR POWER AMPLIFIER DESIGN APPLICATIONS

A THESIS SUBMITTED TO
THE GRADUATE SCHOOL OF NATURAL AND APPLIED SCIENCES
OF
MIDDLE EAST TECHNICAL UNIVERSITY

BY

UĞUR SEDEF

IN PARTIAL FULFILLMENT OF THE REQUIREMENTS
FOR
THE DEGREE OF MASTER OF SCIENCE
IN
ELECTRICAL AND ELECTRONICS ENGINEERING

NOVEMBER 2024

Approval of the thesis:

**A COMPARATIVE STUDY ON ANALYTICAL MODELLING OF BONDWIRES FOR POWER AMPLIFIER DESIGN APPLICATIONS**

submitted by **UĞUR SEDEF** in partial fulfillment of the requirements for the degree of **Master of Science in Electrical and Electronics Engineering Department, Middle East Technical University** by,

Prof. Dr. Naci Emre Altun
Dean, Graduate School of **Natural and Applied Sciences** _____

Prof. Dr. İlkay Ulusoy
Head of Department, **Electrical and Electronics Engineering** _____

Assist. Prof. Dr. Ahmet Cemal Durgun
Supervisor, **Electrical and Electronics Engineering** _____

**Examining Committee Members:**

Prof. Dr. Gülbin Dural
Electrical and Electronics Engineering, METU _____

Assist. Prof. Dr. Ahmet Cemal Durgun
Electrical and Electronics Engineering, METU _____

Prof. Dr. Sencer Koç
Electrical and Electronics Engineering, METU _____

Prof. Dr. Vakur B. Ertürk
Electrical and Electronics Engineering, Bilkent University _____

Assoc. Prof. Dr. Lale Alatan
Electrical and Electronics Engineering, METU _____

Date:29.11.2024

**I hereby declare that all information in this document has been obtained and presented in accordance with academic rules and ethical conduct. I also declare that, as required by these rules and conduct, I have fully cited and referenced all material and results that are not original to this work.**

Name, Surname: Uğur Sedef

Signature :

# ABSTRACT

## A COMPARATIVE STUDY ON ANALYTICAL MODELLING OF BONDWIRES FOR POWER AMPLIFIER DESIGN APPLICATIONS

Sedef, Uğur
M.S., Department of Electrical and Electronics Engineering
Supervisor: Assist. Prof. Dr. Ahmet Cemal Durgun

November 2024, 118 pages

Accurate modeling of bond-wires is crucial for optimizing circuit performance. This thesis evaluates eight analytical models considering geometry- and frequency-dependent characteristics, such as inductance, resistance, and capacitance to the ground plane. Starting with DC resistance and inductance, frequency effects and capacitance are sequentially included, culminating in models addressing grounding effects. Lumped element values from each model were validated against analytical calculations and ANSYS-Q3D results, achieving errors below 5% for inductance and resistance and under 15% for capacitance. The comprehensive models, Model-3 (accounting for DC resistance, inductance, mutual inductance, and capacitance) and Model-6 (including frequency and grounding effects), were further validated against HFSS simulations. As complexity increased, the models aligned more closely with HFSS, particularly at higher frequencies. Model-6 proved suitable for bond-wire analysis in power amplifiers, specifically for connections between a die transistor and another substrate. It was integrated with an 8-11 GHz MMIC PA (output power: 43 dBm) and evaluated in four configurations: two single-wire cases of varying lengths and two double-wire cases with shorter and longer wires. For single-wire cases, Model-6 showed

a maximum discrepancy of 0.4 dB in output power compared to HFSS, with gain and power-added efficiency (PAE) differences below 0.4 dB and 5%, respectively. Double-wire configurations, with reduced inductance, achieved impedance closer to 50 ohms, yielding output power differences under 0.3 dB and gain and PAE deviations of 0.2 dB and 4%. Implemented in MATLAB, the model enabled rapid predictions and iterative design optimization, outperforming time-intensive 3D simulations. These results highlight Model-6's efficacy in analyzing and optimizing bond-wire effects in RF power amplifiers.

Keywords: Bond-wire, Lumped Element, Analytical Model, Inductance, HFSS

# ÖZ

## GÜÇ YÜKSELTEÇ TASARIM UYGULAMALARI İÇİN BAĞ TELLERİNİN ANALİTİK MODELLERİNİN KARŞILAŞTIRILMASI

Sedef, Uğur
Yüksek Lisans, Elektrik ve Elektronik Mühendisliği Bölümü
Tez Yöneticisi: Dr. Öğr. Üyesi. Ahmet Cemal Durgun

Kasım 2024 , 118 sayfa

Bağ teli (bond-wire) modellemesi, devre performansını optimize etmek için kritik bir öneme sahiptir. Bu tez, geometriye ve frekansa bağlı özellikleri, örneğin endüktans, direnç ve toprak düzlemine olan kapasitansı dikkate alan sekiz analitik modeli değerlendirmektedir. DC direnci ve endüktansı ile başlayan analiz, sırasıyla frekans etkileri ve kapasitansı da içerecek şekilde genişletilmiş ve topraklama etkilerini ele alan modellerle sonuçlanmıştır. Her modelin yığılmış eleman değerleri, analitik hesaplamalar ve ANSYS-Q3D sonuçlarıyla doğrulanmış ve endüktans ve direnç için %5'in, kapasitans için ise %15'in altında hatalar elde edilmiştir.

En kapsamlı modeller olan Model-3 (DC direnci, endüktans, karşılıklı endüktans ve kapasitansı içeren) ve Model-6 (frekans ve topraklama etkilerini de içeren) ayrıca HFSS simülasyonlarıyla doğrulanmıştır. Model karmaşıklığı arttıkça, özellikle yüksek frekanslarda, HFSS ile uyum artmıştır. Model-6, özellikle bir çip transistörü ile başka bir alt tabaka arasındaki bağlantılar için güç amplifikatörlerinde bağ teli analizi için uygun bulunmuştur. 8-11 GHz MMIC güç amplifikatörü (çıkış gücü: 43 dBm) ile entegre edilen model, dört farklı konfigürasyonda değerlendirilmiştir: iki farklı

uzunlukta tek telli durum ve kısa ile uzun tellere sahip iki çift telli durum.

Tek telli durumlar için, Model-6'nın HFSS ile karşılaştırıldığında çıkış gücünde en fazla 0,4 dB fark gösterdiği, kazanç ve güç-ekleme verimliliği (PAE) farklılıklarının ise sırasıyla 0,4 dB ve %5'in altında olduğu görülmüştür. Çift telli durumlarda, azalan endüktans, tel empedansını 50 ohm'a yaklaştırmış ve çıkış gücünde 0,3 dB'nin altında, kazanç ve PAE'de sırasıyla 0,2 dB ve %4 farkla sonuçlanmıştır. MATLAB'de uygulanan model, hızlı tahminler ve bağ teli etkileri üzerine içgörüler sunarak, verimli optimizasyon ve iteratif tasarım süreçlerini mümkün kılmıştır. Bu yaklaşım, zaman alıcı 3D simülasyonlara kıyasla önemli avantajlar sağlamaktadır.

Anahtar Kelimeler: Bağ Teli, Yığılı Eleman, Analitik Model, Endüktans, HFSS

To my mother and father

## ACKNOWLEDGMENTS

I would like to extend my profound gratitude to my thesis adviser, Ahmet Cemal Durgun, for his tremendous advice, trust, and insights along this trip. His insights and guidance have been important in influencing this thesis and my scholarly development. Also, I wish to express my sincere gratitude to my thesis jury for their time, effort, and insightful critiques that contributed to the refinement of this work.

A very special thanks to Semra Sultan Uzun, for her unwavering support, both materially and emotionally, throughout this thesis process. Her constant encouragement and motivation have been a cornerstone of my perseverance during challenging times. Her presence by my side has been a source of immense strength and meaning to me, and I am profoundly grateful for all that she has done.

I am profoundly grateful to my friends, Cansu Yıldırım, Efe Berkay Yitim, Melih Can Zerin, Derya Sarmısak, and Umur Doğan, for their unwavering motivation and support during this trip. I consider myself blessed to own such remarkable companions in my life.

I would like to express my heartfelt gratitude to my company, ASELSAN, and my colleagues for their invaluable support throughout my thesis process. Their continuous interest, resources, and opportunities have played a significant role in the successful completion of this work. I am especially grateful to Murat Koç, Volkan Açıkel, Kağan Berk Tanaydın, and Engin Can Çiçek for their unwavering availability in addressing my inquiries, as well as for their technical expertise, encouragement, and guidance during this journey.

I am profoundly indebted to my esteemed parents, Ahizer Sedef and Hüseyin Sedef. I can never completely repay them for their unwavering love and support, which enabled me to concentrate on my academics and academic endeavors. Finally, I wish to express my gratitude to my brother, Ufuk Sedef, and my siblings Hasret Sedef Adıgüzel, and İnci Dere, for their unwavering support and concern during this trip.

## TABLE OF CONTENTS

ABSTRACT . . . . . v

ÖZ . . . . . vii

ACKNOWLEDGMENTS . . . . . x

TABLE OF CONTENTS . . . . . xi

LIST OF TABLES . . . . . xiv

LIST OF FIGURES . . . . . xvi

LIST OF ABBREVIATIONS . . . . . xxiv

CHAPTERS

1 INTRODUCTION . . . . . 1

1.1 Background . . . . . 1

1.1.1 RF Power Amplifiers . . . . . 1

1.1.2 Packaging . . . . . 2

1.2 Motivation and Problem Definition . . . . . 3

1.3 Literature Review . . . . . 4

1.4 Contributions and Novelties . . . . . 6

1.5 The Outline of the Thesis . . . . . 6

2 NUMERICAL MODELLING OF BONDWIRES . . . . . 7

2.1 Packaged Transistor . . . . . 7

2.1.1 Transistor . . . . . 7
2.1.2 Bondwire and Package Parasitic . . . . . 9
2.2 3D MODEL . . . . . 13
2.2.1 HFSS . . . . . 13
2.2.2 Q3D . . . . . 15
2.3 Effect of Geometric Dimensions of Bondwire . . . . . 16
2.3.1 Length . . . . . 17
2.3.1.1 Effect of $d_{bp}$ . . . . . 17
2.3.1.2 Effect of $L_{hmax}$ . . . . . 20
2.3.2 Effect of Radius of Bond wire . . . . . 21
2.4 Effect of Number of Bondwires . . . . . 23
2.5 Effect of Material . . . . . 24
3 LUMPED ELEMENT MODEL OF WIRE-BOND . . . . . 25
3.1 Single wire Model . . . . . 25
3.1.1 Inductance Derivation . . . . . 26
3.1.1.1 Partial Self-Inductance of Bond-wire . . . . . 26
External Self Inductance . . . . . 27
Internal Self Inductance . . . . . 33
3.1.2 Resistance . . . . . 38
3.1.3 Capacitance . . . . . 44
3.1.4 Ground Plane Effect . . . . . 47
3.1.5 Comparison Of The Models with HFSS Simulation Results . . 50
3.2 Double Wire Model . . . . . 66

3.2.1 Mutual inductance of Parallel Bond-wires Carrying a Signal . 66

3.2.2 Interaction with Image of Wires . . . . . 69

3.2.3 Comparison Of The Models with HFSS Simulation Results for Double Wire Configuration . . . . . 72

4 APPLICATION: POWER AMPLIFIERS . . . . . 87

4.1 Wirebond Usage on MMIC . . . . . 87

4.2 Comparison of The Lumped Element Models with HFSS Results . . 88

4.2.1 Single Wire Cases . . . . . 88

4.2.2 Double Wire Cases . . . . . 91

5 CONCLUSION . . . . . 95

REFERENCES . . . . . 99

A HFSS SETUP . . . . . 105

B Q3D SETUP . . . . . 113

C CAUSAL RELATIONSHIP BETWEEN RESISTANCE AND INTERNAL INDUCTANCE . . . . . 117

## LIST OF TABLES

TABLES

Table 2.1 Setup for HFSS Simulation . . . . . 15

Table 2.2 Effect of Distance Between Pads of Bondwire ($d_{bp}$) on DC R, L, C Values of Bondwire - Q3D . . . . . 18

Table 2.3 Effect of Height of Bondwire ($L_{hmax}$) on DC R, L, C Values of Bondwire - Q3D . . . . . 20

Table 2.4 Effect of Radius of Bondwire ($r_{bw}$) on DC R, L, C Values of Bondwire - Q3D . . . . . 22

Table 3.1 Comparison of DC Inductance for Analytical Solution and Q3D Simulation with Different $d_{bp}$ Values for $L_{hmax} = 200\mu m$ and $r_{bw} = 12.5\mu m$ 36

Table 3.2 Comparison of DC Inductance for Analytical Solution and Q3D Simulation with Different $L_{hmax}$ Values for $d_{bp} = 1000\mu m$ and $r_{bw} = 12.5\mu m$ . . . . . 36

Table 3.3 Comparison of DC Inductance for Analytical Solution and Q3D Simulation with Different $r_{bw}$ Values for $d_{bp} = 1000\mu m$ and $L_{hmax} = 200\mu m$ 36

Table 3.4 Comparison of DC Resistance for Analytical Solution and Q3D Simulation with Different $d_{bp}$ Values for $L_{hmax} = 200\mu m$ and $r_{bw} = 12.5\mu m$ 40

Table 3.5 Comparison of DC Resistance for Analytical Solution and Q3D Simulation with Different $L_{hmax}$ Values for $d_{bp} = 1000\mu m$ and $r_{bw} = 12.5\mu m$ . . . . . 40

Table 3.6 Comparison of DC Resistance for Analytical Solution and Q3D Simulation with Different $r_{\text{bw}}$ Values for $d_{\text{bp}} = 1000\mu m$ and $L_{\text{hmax}} = 200\mu m$ 40

Table 3.7 Comparison of Capacitance to Ground Plane of Analytical Solution and Q3D Simulation For Different $d_{bp}$ Values . . . . . 46

Table 3.8 Comparison of Capacitance to Ground Plane of Analytical Solution and Q3D Simulation For Different $L_{hmax}$ Values . . . . . 46

Table 3.9 Comparison of Capacitance to Ground Plane of Analytical Solution and Q3D Simulation For Different Radius of Wire ($r_{bw}$) Values . . . . . 47

Table 3.10 Mutual Inductances to Ground Plane of a Single Wire for Different $d_{bp}$ Values . . . . . 49

Table 3.11 Mutual Inductances to Gorund Plane of a Single Wire for Different $L_{hmax}$ Values . . . . . 50

Table 3.12 Mutual Inductances to Ground Plane of a Single Wire for Different $r_{bw}$ Values . . . . . 50

Table 3.13 Mutual Inductance of Double Wires with Different Parameters . . . 69

Table A.1 Comparison of Wave Port and Lumped Port . . . . . 108

## LIST OF FIGURES

FIGURES


Figure 2.1 A group Die transistor on a wafer [19] . . . . . 8

Figure 2.2 A Die Transistor With Its Gate and Drain [20] . . . . . 9

Figure 2.3 Assembly of a Die Transistor and Package [21] . . . . . 10

Figure 2.4 Fabrication of Bonding Process [22] . . . . . 11

Figure 2.5 Output Power For Die [24] . . . . . 12

Figure 2.6 Output Power for Packaged Transistor [25] . . . . . 12

Figure 2.7 A 3D Model Geometry of bondwire from HFSS . . . . . 13

Figure 2.8 Visualization of Integration Line and Deembedding for Waveport 14

Figure 2.9 Geometry of a bondwire in Q3D . . . . . 16

Figure 2.10 Gaussian Shaped bondwire Dimensions . . . . . 17

Figure 2.11 Frequency Dependent Inductance for Different $d_{bp}$ Values . . . . 18

Figure 2.12 Frequency Dependent Resistance for Different ($d_{bp}$) Values . . . 19

Figure 2.13 $S_{21}$ (dB) for Different $d_{bp}$ Values . . . . . 19

Figure 2.14 Frequency Dependent Inductance for Different $L_{hmax}$ values . . . 20

Figure 2.15 Frequency Dependent Resistance for Different $L_{hmax}$ values . . . 21

Figure 2.16 $S_{21}$ (dB) for Different $L_{hmax}$ Values . . . . . 21

Figure 2.17 Frequency Dependent Inductance for Different Radius values . . 22

Figure 2.18 $S_{21}$ (dB) for Different Radius of Wire Values . . . . . 23

Figure 2.19 Magnitude of $S_{21}$ Comparison of Single, Double and Triple bondwire in Parallel . . . . . 24

Figure 3.1 Lumped Element Model of A Single Bondwire [30] . . . . . 26

Figure 3.2 Closed Current Loop and Magnetic Potential Vectors on One of the Segments [35] . . . . . 27

Figure 3.3 Filament Current and Created Magnetic Flux around the wire . . 29

Figure 3.4 Defining Dimensions . . . . . 30

Figure 3.5 Models used to represent the shape of bond wire interconnects; (a) semicircle; (b) JEDEC; (c) proposed model in [17]; (d) manufactured bond wire using the wedge–wedge bonding process as example. . 31

Figure 3.6 Gaussian Shaped Bond-wire Dimensions . . . . . 32

Figure 3.7 Internal Inductance Region [38] . . . . . 33

Figure 3.8 Frequency Dependent Inductance Values of Q3D and Analytical Solution for Different $d_{bp}$ Values . . . . . 37

Figure 3.9 Frequency Dependent Inductance Values of Q3D and Analytical Solution for Different $L_{hmax}$ Values . . . . . 37

Figure 3.10 Frequency Dependent Inductance Values of Q3D and Analytical Solution for Different Radius Values . . . . . 38

Figure 3.11 Skin Depth vs Frequency . . . . . 39

Figure 3.12 Frequency Dependent Resistance Value Comparison of Q3D and Analytical Solution For Different $d_{bp}$ Values . . . . . 41

Figure 3.13 Frequency Dependent Resistance Value Comparison of Q3D and Analytical Solution For Different $L_{hmax}$ Values . . . . . 41

Figure 3.14 Frequency Dependent Resistance Value Comparison of Q3D and Analytical Solution For Different $r_{bw}$ Values . . . . . 42

Figure 3.15 Frequency Dependent Resistance Comparison of Simple formula used in the thesis and Bessel Based Formula . . . . . 43

Figure 3.16 Frequency Dependent Inductance (Internal Inductance) Comparison of Simple formula used in the thesis and Bessel Based Formula 43

Figure 3.17 a) - b) A complex function maps of half of the circular wire with radius R . . . . . 45

Figure 3.18 Mutual Inductance to Ground Plane Using Image Theory . . . . 48

Figure 3.19 Ground Plane Mutual Inductance Effect . . . . . 49

Figure 3.20 Cumulatively Created Lumped Element Models for a Single Wire 51

Figure 3.21 Asymmetrical and Symmetrical Models . . . . . 52

Figure 3.22 Comparison of Asymmetrical and Symmetrical Models with HFSS 52

Figure 3.23 Single Wire-Comparison of $S_{11}$ on Smith Chart for $d_{bp} = 1500\,\mu m$, $L_{hmax} = 200\,\mu m$, $r_{bw} = 12.5\,\mu m$ . . . . . 53

Figure 3.24 Single Wire-Comparison of $S_{11}$ on Smith Chart for $d_{bp} = 750\,\mu m$, $L_{hmax} = 200\,\mu m$, $r_{bw} = 12.5\,\mu m$ . . . . . 54

Figure 3.25 Single Wire - NMSE of Complex $S_{11}$ along Frequency Band for Different $d_{bp}$ Values - $d_{bp}$ Sweep, $L_{hmax} = 200\,\mu m$, $r_{bw} = 12.5\,\mu m$, (NMSE is calculated over 0.05-20 GHz) . . . . . 56

Figure 3.26 Single Wire - NMSE of Complex $S_{21}$ along Frequency Band for Different $d_{bp}$ Values - $d_{bp}$ Sweep, $L_{hmax} = 200\,\mu m$, $r_{bw} = 12.5\,\mu m$, (NMSE is calculated over 0.05-20 GHz) . . . . . 56

Figure 3.27 Single Wire - NMSE of Complex $S_{11}$ calculated from $d_{bp}$ sweep at A Frequency. - Frequency Sweep, $L_{hmax} = 200\,\mu m$, $r_{bw} = 12.5\,\mu m$, (NMSE is calculated over $d_{bp} = 750 - 1500\,\mu m$) . . . . . 57

Figure 3.28 Single Wire - NMSE of Complex $S_{21}$ calculated from $d_{\text{bp}}$ sweep at A Frequency. - Frequency Sweep, $L_{hmax} = 200\,\mu m$, $r_{bw} = 12.5\,\mu m$, (NMSE is calculated over $d_{bp} = 750 - 1500\,\mu m$) . . . . . 58

Figure 3.29 Single Wire - NMSE of Complex $S_{11}$ along Frequency Band for Different $L_{\text{hmax}}$ Values - $L_{hmax}$ Sweep, $d_{bp} = 1000\,\mu m$, $r_{bw} = 12.5\,\mu m$, (NMSE is calculated over 0.05-20 GHz) . . . . . 59

Figure 3.30 Single Wire - NMSE of Complex $S_{21}$ along Frequency Band for Different $L_{\text{hmax}}$ Values - $L_{hmax}$ Sweep, $d_{bp} = 1000\,\mu m$, $r_{bw} = 12.5\,\mu m$, (NMSE is calculated over 0.05-20 GHz) . . . . . 59

Figure 3.31 Single Wire - NMSE of Complex $S_{11}$ calculated from $L_{\text{hmax}}$ sweep at A Frequency. - Frequency Sweep, $d_{bp} = 1000\,\mu m$, $r_{bw} = 12.5\,\mu m$, (NMSE is calculated over $L_{hmax} = 200 - 600\,\mu m$) . . . . . 60

Figure 3.32 Single Wire - NMSE of Complex $S_{21}$ calculated from $L_{\text{hmax}}$ sweep at A Frequency. - Frequency Sweep, $d_{bp} = 1000\,\mu m$, $r_{bw} = 12.5\,\mu m$, (NMSE is calculated over $L_{hmax} = 200 - 600\,\mu m$) . . . . . 60

Figure 3.33 Single Wire - NMSE of Complex $S_{11}$ along Frequency Band for Different $r_{\text{bw}}$ Values - $r_{bw}$ Sweep, $d_{bp} = 1000\,\mu m$, $L_{hmax} = 200\,\mu m$, (NMSE is calculated over 0.05-20 GHz) . . . . . 61

Figure 3.34 Single Wire - NMSE of Complex $S_{21}$ along Frequency Band for Different $r_{\text{bw}}$ Values - $r_{bw}$ Sweep, $d_{bp} = 1000\,\mu m$, $L_{hmax} = 200\,\mu m$, (NMSE is calculated over 0.05-20 GHz) . . . . . 61

Figure 3.35 Single Wire - NMSE of Complex $S_{11}$ calculated from $r_{\text{bw}}$ sweep at A Frequency. - Frequency Sweep, $d_{bp} = 1000\,\mu m$, $L_{hmax} = 200\,\mu m$, (NMSE is calculated over $r_{bw} = 12.5 - 37.5\,\mu m$) . . . . . 62

Figure 3.36 Single Wire - NMSE of Complex $S_{21}$ calculated from $r_{\text{bw}}$ sweep at A Frequency. - Frequency Sweep, $d_{bp} = 1000\,\mu m$, $L_{hmax} = 200\,\mu m$, (NMSE is calculated over $r_{bw} = 12.5 - 37.5\,\mu m$) . . . . . 63

Figure 3.37 Single Wire - NMSE of Complex $S_{11}$ with respect to Q3D for $d_{\text{bp}}$. - $d_{bp}$ Sweep, $L_{hmax} = 200\,\mu m$, $r_{bw} = 12.5\,\mu m$, (NMSE is calculated over 0.05-20 GHz) . . . . . 64

Figure 3.38 Single Wire - NMSE of Complex $S_{11}$ with respect to Q3D for $L_{\text{hmax}}$. - $L_{hmax}$ Sweep, $d_{bp} = 1000\,\mu m$, $r_{bw} = 12.5\,\mu m$, (NMSE is calculated over 0.05-20 GHz) . . . . . 65

Figure 3.39 Single Wire - NMSE of Complex $S_{11}$ with respect to Q3D for $r_{\text{bw}}$. - $r_{bw}$ Sweep, $d_{bp} = 1000\,\mu m$, $L_{hmax} = 200\,\mu m$, (NMSE is calculated over 0.05-20 GHz) . . . . . 65

Figure 3.40 Mutual Inductance Derivation . . . . . 67

Figure 3.41 Mutual Inductance Effect . . . . . 68

Figure 3.42 Double Wire Inductance Network . . . . . 70

Figure 3.43 Double Wires Lumped Element Models . . . . . 72

Figure 3.44 Double Wire-Comparison of $S_{11}$ on Smith Chart for $d_{bp} = 1500\,\mu m$ 74

Figure 3.45 Double Wire-Comparison of $S_{11}$ on Smith Chart for $d_{bp} = 750\,\mu m$ 75

Figure 3.46 Double Wire - NMSE of Complex $S_{11}$ along Frequency Band for Different $d_{\text{bp}}$ Values - $d_{bp}$ Sweep, $L_{hmax} = 200\,\mu m$, $p = 100\,\mu m$, (NMSE is calculated over 0.05-20 GHz) . . . . . 76

Figure 3.47 Double Wire - NMSE of Complex $S_{21}$ along Frequency Band for Different $d_{\text{bp}}$ Values - $d_{bp}$ Sweep, $L_{hmax} = 200\,\mu m$, $p = 100\,\mu m$, (NMSE is calculated over 0.05-20 GHz) . . . . . 76

Figure 3.48 Double Wire - NMSE of Complex $S_{11}$ calculated from $d_{\text{bp}}$ sweep at A Frequency. - Frequency Sweep, $L_{hmax} = 200\,\mu m$, $p = 100\,\mu m$, (NMSE is calculated over $d_{bp} = 750 - 1500\,\mu m$) . . . . . 77

Figure 3.49 Double Wire - NMSE of Complex $S_{21}$ calculated from $d_{\text{bp}}$ sweep at A Frequency. - Frequency Sweep, $L_{hmax} = 200\,\mu m$, $p = 100\,\mu m$, (NMSE is calculated over $d_{bp} = 750 - 1500\,\mu m$) . . . . . 77

Figure 3.50 Double Wire - NMSE of Complex $S_{11}$ along Frequency Band for Different $L_{\text{hmax}}$ Values- $L_{hmax}$ Sweep, $d_{bp} = 1000\,\mu m$, $p = 100\,\mu m$, (NMSE is calculated over 0.05-20 GHz) . . . . . 78

Figure 3.51 Double Wire - NMSE of Complex $S_{21}$ along Frequency Band for Different $L_{\text{hmax}}$ Values- $L_{hmax}$ Sweep, $d_{bp} = 1000\,\mu m$, $p = 100\,\mu m$, (NMSE is calculated over 0.05-20 GHz) . . . . . 78

Figure 3.52 Double Wire - NMSE of Complex $S_{11}$ calculated from $L_{\text{hmax}}$ sweep at A Frequency. - Frequency Sweep, $d_{bp} = 1000\,\mu m$, $p = 100\,\mu m$, (NMSE is calculated over $L_{hmax} = 200 - 600\,\mu m$) . . . . . 79

Figure 3.53 Double Wire - NMSE of Complex $S_{21}$ calculated from $L_{\text{hmax}}$ sweep at A Frequency. - Frequency Sweep, $d_{bp} = 1000\,\mu m$, $p = 100\,\mu m$, (NMSE is calculated over $L_{hmax} = 200 - 600\,\mu m$) . . . . . 79

Figure 3.54 Double Wire - NMSE of Complex $S_{11}$ along Frequency Band for Different $p$ Values - $p$ Sweep, $d_{bp} = 1000\,\mu m$, $L_{hmax} = 200\,\mu m$, (NMSE is calculated over 0.05-20 GHz) . . . . . 80

Figure 3.55 Double Wire - NMSE of Complex $S_{21}$ along Frequency Band for Different $p$ Values - $p$ Sweep, $d_{bp} = 1000\,\mu m$, $L_{hmax} = 200\,\mu m$, (NMSE is calculated over 0.05-20 GHz) . . . . . 80

Figure 3.56 Double Wire - NMSE of Complex $S_{11}$ calculated from $p$ sweep at A Frequency. - Frequency Sweep, $d_{bp} = 1000\,\mu m$, $L_{hmax} = 200\,\mu m$, (NMSE is calculated over $p = 200 - 600\,\mu m$) . . . . . 81

Figure 3.57 Double Wire - NMSE of Complex $S_{21}$ calculated from $p$ sweep at A Frequency. - Frequency Sweep, $d_{bp} = 1000\,\mu m$, $L_{hmax} = 200\,\mu m$, (NMSE is calculated over $p = 200 - 600\,\mu m$) . . . . . 82

Figure 3.58 Comparison of 5 different s2p file for $p$ and Their Mean. . . . . 82

Figure 3.59 Comparison of HFSS data and Model-6 Data for $p = 75\mu m$ . . 83

Figure 3.60 Double Wire - NMSE of Complex $S_{11}$ with respect to Q3D for $d_{\text{bp}}$. - $d_{bp}$ Sweep, $L_{hmax} = 200\,\mu m$, $p = 100\,\mu m$, (NMSE is calculated over 0.05-20 GHz) . . . . . 84

Figure 3.61 Double Wire - NMSE of Complex $S_{11}$ with respect to Q3D for $L_{\text{hmax}}$. - $L_{hmax}$ Sweep, $d_{bp} = 1000\,\mu m$, $p = 100\,\mu m$, (NMSE is calculated over 0.05-20 GHz) . . . . . 84

Figure 3.62 Double Wire - NMSE of Complex $S_{11}$ with respect to Q3D for $p$. - $p$ Sweep, $d_{bp} = 1000\,\mu m$, $L_{hmax} = 200\,\mu m$, (NMSE is calculated over 0.05-20 GHz) . . . . . 85

Figure 4.1 Bonding Process of MMIC PA [47] . . . . . 88

Figure 4.2 Cascaded Simulation with Single Wire in ADS . . . . . 89

Figure 4.3 Comparison of Analytical Model and HFSS in terms of Output Power-Single Wire . . . . . 90

Figure 4.4 Comparison of Analytical Model and HFSS in terms of Gain-Single Wire . . . . . 90

Figure 4.5 Comparison of Analytical Model and HFSS in terms of PAE-Single Wire . . . . . 91

Figure 4.6 Cascaded Simulation with Double Wire in ADS . . . . . 91

Figure 4.7 Comparison of Analytical Model and HFSS in terms of Output Power-Double Wire . . . . . 92

Figure 4.8 Comparison of Analytical Model and HFSS in terms of Gain-Double Wire . . . . . 93

Figure 4.9 Comparison of Analytical Model and HFSS in terms of PAE-Double Wire . . . . . 93

Figure A.1 Visualization of Integration Line and Deembedding for Waveport 107

Figure A.2 Proper Waveport Sizing [18] . . . . . 107

Figure A.3 Lumped Port Visualization . . . . . 108

Figure A.4 Solution Setup for HFSS . . . . . 109

Figure A.5 Sweep Setup for HFSS . . . . . 110

Figure B.1 Defining excitation in Q3D . . . . . 113

Figure B.2 Setup in Q3D . . . . . 114

Figure B.3 Result Screen in Q3D . . . . . 115

## LIST OF ABBREVIATIONS

| | |
|---|---|
| FDTD | Finite Difference Time Domain |
| FEM | Finite Element Method |
| MOM | Method of Moements |
| 3D | 3 Dimensional |
| IC | Integrated Circuits |
| BJT | Bipolar Junction Transistor |
| FET | Field Effect Transistor |
| NMOS | N-Channel Metal-Oxide-Semiconductor |
| PMOS | P-Channel Metal-Oxide-Semiconductor |
| PCB | Printed Circuit Board |
| RF | RAdio Frequency |
| HFSS | High Frequency Structure Simulator |
| DC | Direct Current |
| AC | Alternating Current |
| $L_{hmax}$ | Max Height of Bondwire |
| $d_{bp}$ | Distance Between Pads of Bondwire |
| $r_{bw}$ | Radius of Bondwire |
| $R_{DC}$ | DC Resistance |
| $R_{AC}$ | AC Resistance |
| $L_{DC}$ | DC Inductance |
| $L_{AC}$ | AC Inductance |
| JEDEC | Joint Electron Device Engineering Council |
| PAE | Power Added Efficiency |

# CHAPTER 1

# INTRODUCTION

## 1.1 Background

### 1.1.1 RF Power Amplifiers

Power amplifiers, powered by an external DC source, are essential for increasing RF signals to higher power levels, particularly in applications such as transmitters, space and naval systems, electronic warfare, satellite communications, and wireless networks. The amplification process is driven by transistors using an external DC source, which utilize their nonlinear behavior to increase signal amplitude while maintaining the original frequency and waveform characteristics. However, since the input and output impedance of transistors typically differ from the standard 50 Ω impedance of transmission lines—an impedance chosen for its optimal balance between minimal signal attenuation and maximum power capacity—matching networks are required [1]. These networks ensure that the input and output impedance of the transistors are properly aligned with the 50 Ω standard, thereby facilitating efficient signal amplification.

Power amplifiers are evaluated using the following performance parameters [2]:

- **Power Gain**: This parameter measures the extent to which the input RF signal is amplified by the power amplifier.
- **Efficiency**: It represents how effectively the transistor converts DC power into RF signal at the output stage. It includes two types: overall efficiency and power-added efficiency, considering input power.

- **Linearity** : It refers to capacity of the amplifier to accurately amplify an input signal without causing significant distortion or changes to its waveform. Linearity indicates the class of an power amplifier. Class-A is the most linear amplifier class, while it is also the worst efficient one.

- **Return Loss**: Indicates the quality of input and output impedance matching. It measures the reflection caused by mismatches between input impedance and source (input return loss) or output impedance and load (output return loss).

- **Bandwidth**: Refers to the frequency range over which the amplifier meets performance requirements, including effective matching and amplification.

  RF power amplifiers began to evolve in the late $19^{th}$ century with the generation of RF power through spark gap, arc, and alternator techniques, as discussed in the history of power amplifiers [3]. A substantial amount of progress was achieved by vacuum tubes, which are capable of generating and controlling RF signals. Vacuum tube amplifiers were the industry standard until the mid-1970s, at which point the emphasis transitioned to solid-state devices [3]. This transition marked the introduction of bipolar junction transistors (BJTs), MOSFETs, and, ultimately, GaAs and GaN transistors, which provided enhancements in frequency performance, power output, and efficiency. RF power amplifiers that are more compact, reliable, and energy-efficient were the result of these innovations. These amplifiers are now an essential component of modern communication systems, radar, and other RF technologies.

### 1.1.2 Packaging

RF packages play a crucial role in telecommunications and military applications, with distinct methods tailored for each. While commercial applications typically use affordable plastic enclosures, military applications demand specialized designs to achieve superior performance and reliability. As RF packaging technology advances, factors such as operating frequency, cost, and packaging techniques are evolving rapidly [4].

The choice of packaging and assembly techniques significantly affects a transistor's

performance, reliability, and cost. It is essential to minimize the negative impacts of assembly processes and package parasitics to prevent performance degradation. Additionally, managing the complexity of the package is important to control costs.

Flip-chip and wire-bond packaging are two distinct semiconductor assembly methods with different advantages and applications. Flip-chip packaging involves flipping the semiconductor die and mounting it directly onto a substrate, with electrical connections made through solder bumps. This method offers several benefits, including reduced parasitics, improved thermal management, higher I/O density, and better electrical performance, making it ideal for high-performance applications like processors and high-frequency RF components [5]. However, flip-chip technology is generally more expensive and complex because of the advanced precision required for solder bumping and alignment [6]. On the other hand, wire-bond packaging connects the die to the substrate using fine wires, which makes it more cost-effective and flexible. This method is well-established and widely used in commercial and consumer electronics because of its lower cost and adaptability. However, it suffers from higher parasitics and less efficient thermal management compared to flip-chip, often resulting in larger package sizes. While flip-chip is suited for applications requiring high performance and compact design, wire-bonding is preferable for cost-sensitive and versatile applications [7].

## 1.2 Motivation and Problem Definition

In design of power amplifiers using die transistors, accurate bondwire modeling is crucial. While 3D simulations are detailed, they are often resource-intensive and time-consuming. At this point, analytical modeling offers a practical alternative. Analytical modeling allows for a comprehensive understanding of a bondwire structure's fundamental physical properties and behavior through mathematical expressions, eliminating the need for simulations. This approach offers significant advantages in terms of speed and performance compared to 3D simulations, as analytical models typically require fewer computational resources and yield results more quickly. Additionally, when properly developed, analytical models can achieve a level of accuracy comparable to that of complex 3D simulations. Therefore, when

the key parameters of a bondwire structure are accurately modeled analytically, the structure's performance can be understood without the need for time-consuming and resource-intensive simulations.

## 1.3 Literature Review

As communication technology continues to advance, there is a growing demand for RF devices that can operate at high frequencies. These devices are being developed to meet challenging goals such as achieving high efficiency at low cost while taking up less space, and designing products that are easy to integrate and manufacture. RF amplifiers, which consist of gain stages, low noise amplifiers, and power amplifiers, are placed as the transmitter and receiver front-end in this group, making them a significant subject of academic research. In recent years, packaging has increasingly been applied to RF hardware products because of environmental and thermal issues. Wire-bond packaging is the most preferred type because of its cost-effectiveness, ease of integration with developing technology, and proven reliability. However, the parasitics that it introduces can lead to performance degradation in RF structures, causing issues such as transmission power loss and phase shift [8]. At low frequency bands, the parasitic parameters of the bond wire are negligible and can be approximated to an inductance. However, as the frequency increases, these parasitic parameters become significant and have a substantial impact on transmission power, return loss, and phase shift. Additionally, these parasitics vary with the physical characteristics of the wire, such as thickness, length, material, and number [8]. In the design of power amplifiers, these parasitics directly affect output power, gain, and efficiency. Therefore, it becomes significant to characterize parasitic effects of bond-wire.

Numerous studies in the literature have been conducted on these wire bond structures in order to characterize the parasitic effects. In [9], extraction of the parasitic of the bond-wire is obtained from measurement of scattering parameters of a bond-wire geometry. In [10], to characterize bondwire, a finite difference time domain (FDTD) method and a quasi-static method is proposed. For the method FDTD, a discretization method causing nonuniform mesh and polynomial approximation of the bond-wire structure is mentioned. The results are compared to quasi-static model

composed of lumped element, only inductance, and uniform transmission lines with characteristic impedance and lengths. When examining analytical models in the literature, several key approaches are noted. In [11], a bond wire with a known shape as a function of its dimensions is modeled as an inductance incorporating frequency dependency resulting from skin effect. Additionally, there are studies that model bond wires as lumped element models using the causality relationship between inductance and resistance. For instance, In [12], A model based on causality is presented to characterize the electrical characteristics of multiple bond wires, taking into account the signal frequency and wire shape. This model considers the impact of inductive coupling, frequency-dependent losses, and the capacitance between the wires and the ground plane. Similarly, in [13], it is proposed that resistance and inductance can be determined using the causality relationship from characteristic impedance. For numerical modeling of parasitics, [14] presents a method where a semi-circular shaped bond wire is divided into finite number of sections. For each section, the inductance, capacitance to the ground plane, and resistance are calculated. In the case of multiple parallel bond wires, mutual inductance is included in the overall lumped element RLC model. However, apart from the previously mentioned studies, the frequency dependency of the parameters is generally not accounted for in these models.

In the concept of power amplifier design, bond-wires are used to package bare die transistors in order to protect it from environmental factors. In [15], during packaging process of a bare die transistor, analytically derived lumped element bond-wire model, which considers only inductance without skin effect and resistance, is examined. The footprint area of the matching networks is accordingly optimized. As an another implementation considering matching networks, in [16] the mismatch caused by bond-wire structure is compensated after modelling the bond-wire network as R-L and pad capacitance. Additionally, in [8], by incorporating partial and mutual inductance, a model forming a basis for a harmonic control network that integrates double-bond-wire structure has been developed, which increases the efficiency.

In this thesis, taking [17] as the starting point, 6 different lumped element models are implemented composed of inductance, resistance and capacitance, which are derived analytically. In [11], the author characterizes a bond-wire as self inductance and resistance. In the thesis study, adding a capacitance, mutual inductance to ground

plane and mutual inductance to the other signal paths, the cumulatively developed lumped element models are compared with the results obtained from HFSS.

## 1.4 Contributions and Novelties

The contributions of the thesis are as follows:

- It is observed and demonstrated that the effect of geometric parameters and the number of bond-wires can be detailed and analyzed efficiently using analytical formulas in a short time.
- The bond-wire models, which have predominantly been studied as inductance in previous applications, are systematically examined to assess the impact of additional factors such as frequency effects, capacitance effects, and ground plane effects. This analysis is conducted by integrating insights gathered from the literature.

## 1.5 The Outline of the Thesis

This research centers on the analytical modeling of IC interconnects, with a focus on comparing the results with those obtained from the 3D simulation environment, HFSS [18]. Chapter 2 introduces the problem definition and outlines the simulation setup. After, this chapter explains the effect of geometrical parameters of bondwire structures on resistance, inductance an capacitance. Chapter-3 provides an in-depth analysis of each lumped element that collectively represents a bond wire, including a detailed derivation of inductance for both single and double-wire geometries. The chapter then explores the analytical formulations for resistance and capacitance. Various lumped element models, each reflecting different improvements, are developed. Finally, the analytical results from all models are compared with the simulation outcomes, and the findings are discussed in this section. In Chapter-4, an power amplifier design is carried out at the simulation level using both the simulation and analytical bond models. The results obtained from each approach are compared to evaluate the accuracy and effectiveness of the analytical bondwire models.

# CHAPTER 2

# NUMERICAL MODELLING OF BONDWIRES

In this section, full-wave analysis of a bondwire geometry with ANSYS HFSS tool and quasi static analysis with ANSYS Q3D tool will be mentioned.

## 2.1 Packaged Transistor

### 2.1.1 Transistor

Transistors are primarily classified into two categories: Bipolar Junction Transistors (BJTs) and Field Effect Transistors (FETs). BJTs are further divided into NPN and PNP types. NPN transistors have three terminals—base, emitter, and collector—and operate with current flowing from the emitter to the collector when a small current is applied to the base. PNP transistors also have three terminals, but the current flows from the collector to the emitter when a small current is applied to the base.

FETs are also categorized into NMOS and PMOS types. NMOS transistors use an n-type semiconductor for the channel and are turned on when a positive voltage is applied to the gate relative to the source, allowing current to flow between the drain and source. PMOS transistors use a p-type semiconductor for the channel and are activated when a negative voltage is applied to the gate relative to the source, allowing current to flow between the source and drain.

FETs can be made from various materials. Silicon-based FETs are widely used due to their versatility and cost-effectiveness, and are commonly found in digital circuits, analog applications, power management systems, and consumer electronics. Gallium Arsenide (GaAs) FETs are utilized for their high-frequency performance and effi-

ciency, making them ideal for applications such as RF amplifiers, microwave communication systems, and satellite communications. GaAs FETs are valued for their ability to operate at higher frequencies and with better performance in high-speed and high-frequency applications compared to silicon-based devices. Gallium Nitride (GaN) FETs are preferred for high-power applications due to their high breakdown voltage and excellent thermal conductivity.

A power transistor in its unprocessed form is referred to as a "bare die." This bare die consists of multiple transistors embedded within it and is initially produced as part of a large wafer on a single wafer. The wafer is then sliced into numerous individual segments, with each segment being a separate die containing one integrated circuit. In the Figure 2.1, a wafer and die is shown.

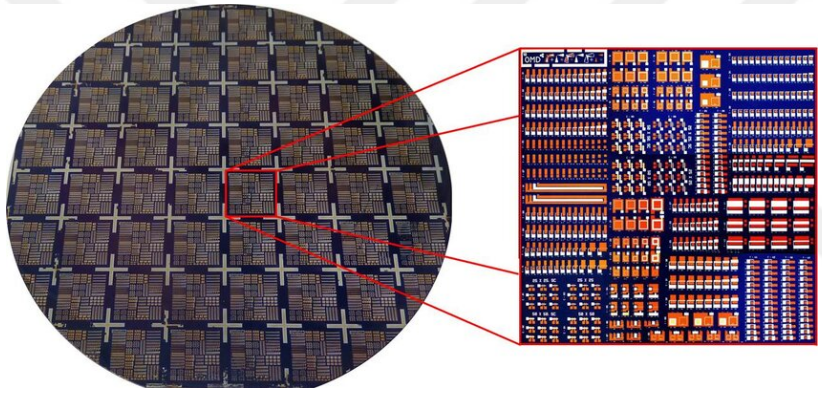


Figure 2.1: A group Die transistor on a wafer [19]

A die transistor is also shown in Figure 2.2. Bare die transistors are generally not used directly in electronic assemblies. Many gate and drain pads are required to facilitate connections to external circuitry. They are challenging to mount onto a printed circuit board (PCB) and can be susceptible to damage and deformation from environmental factors. Consequently, they are usually encased in protective structures to safeguard them mechanically, called as package. Additionally, for high-power applications, managing heat dissipation is essential to prevent performance issues, particularly in RF circuits. Effective packaging ensures proper heat management, maintaining the transistor's reliability and efficiency.

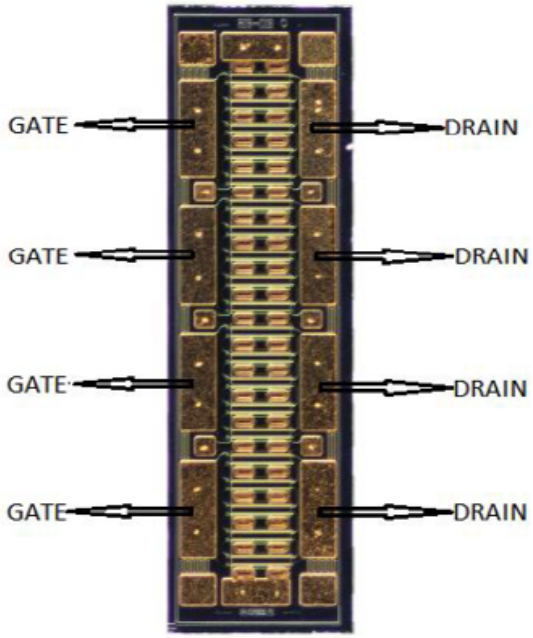



Figure 2.2: A Die Transistor With Its Gate and Drain [20]

### 2.1.2 Bondwire and Package Parasitic

Packaging involves the design and construction of protective enclosures for radio frequency (RF) devices, including transmitters, receivers, and other wireless communication components. The main goal of RF packaging is to create a shielded environment that guards the RF components against electromagnetic interference (EMI), which can adversely affect their performance.

RF packaging employs various techniques and materials, such as conductive metals, plastics, and ceramics, to construct enclosures that contain RF signals and block external noise or interference. The design of these enclosures must also address heat dissipation, mechanical stability, and ease of assembly and disassembly on a PCB.

In the provided example in Figure 2.3, a bare die is combined with an enclosure that meets both mechanical and thermal requirements. This combination results in a packaged transistor from MACOM, a leading global manufacturer of power transistors, as depicted in Figure 2.3[21].

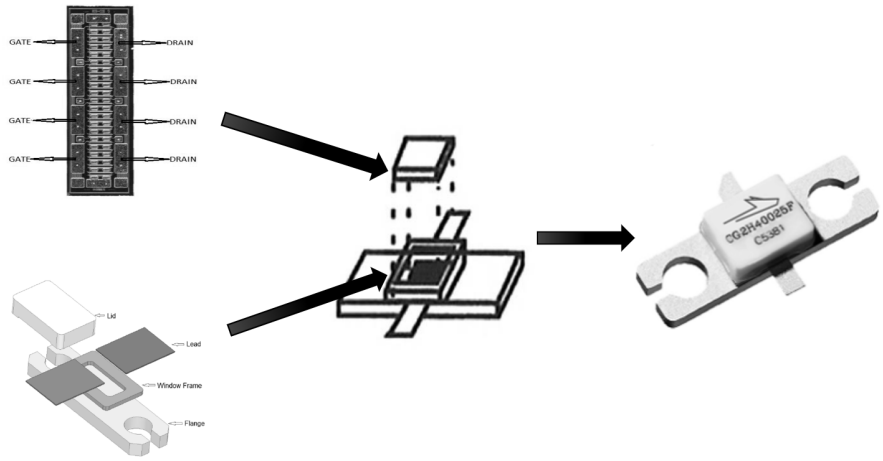



Figure 2.3: Assembly of a Die Transistor and Package [21]

In the presented scenario, a packaged transistor is mounted on a printed circuit board (PCB) through its external leads. To establish electrical connections between the internal pads of the die transistor and the external leads of the packaged transistor, which are soldered onto the PCB, very thin wires known as bond wires are utilized. These bond wires facilitate the critical electrical linkage necessary for the transistor's operation. The use of bond wires ensures precise and reliable connections between the die and the PCB, accommodating the physical and electrical requirements of the device.

Bond wires are typically made from gold due to its superior conductivity and excellent corrosion resistance compared to other materials. However, bond wires can also be made from other materials, such as aluminum, which is often used for its cost-effectiveness and good performance in certain applications, and copper, which offers high conductivity and is utilized in high-performance scenarios. The choice of bond wire material is application-dependent, and various shapes of bond wires are employed to meet specific requirements, as illustrated in the accompanying figures. The production of bond wires involves a precise and sensitive fabrication process, which is depicted in Figure 2.4 [22].

With the transistor now connected to the external circuitry, it benefits from reduced

environmental effects and improved heat dissipation. However, packaging introduces certain parasitic effects that can impact performance. One notable effect is the reduction in output power. The comparison of output power between a die transistor and a packaged transistor highlights a performance degradation as shown in Figure 2.5 and Figure 2.6, respectively. The degradation occurs due to unwanted **self inductance of wire**, **mutual inductance of wires capacitance** and **resistance** of bondwire structures which adversely affect the overall performance of the transistor in its packaged form [23].

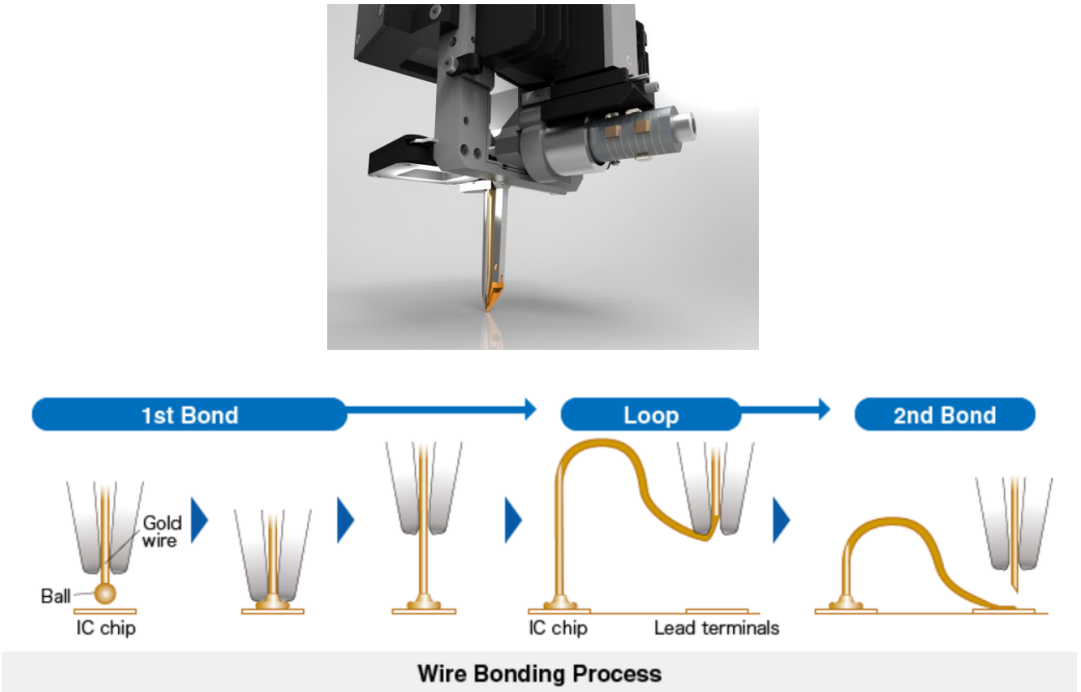



Figure 2.4: Fabrication of Bonding Process [22]

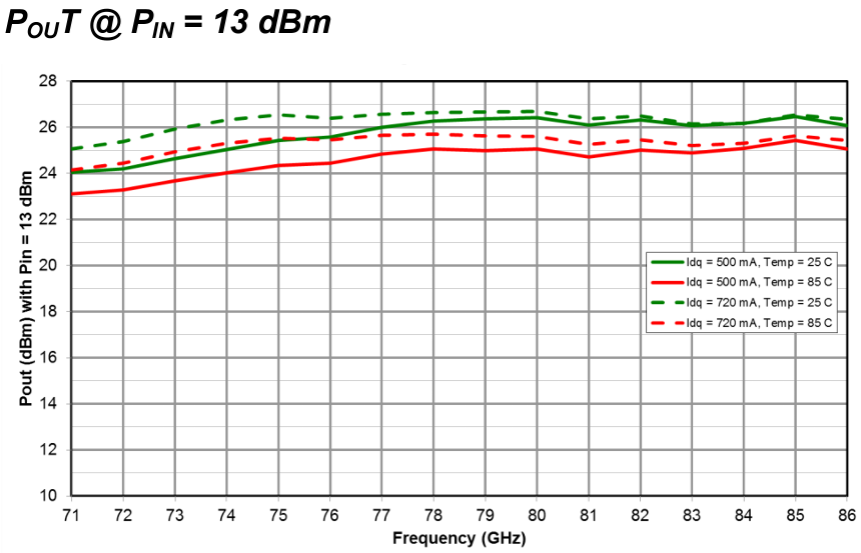



Figure 2.5: Output Power For Die [24]

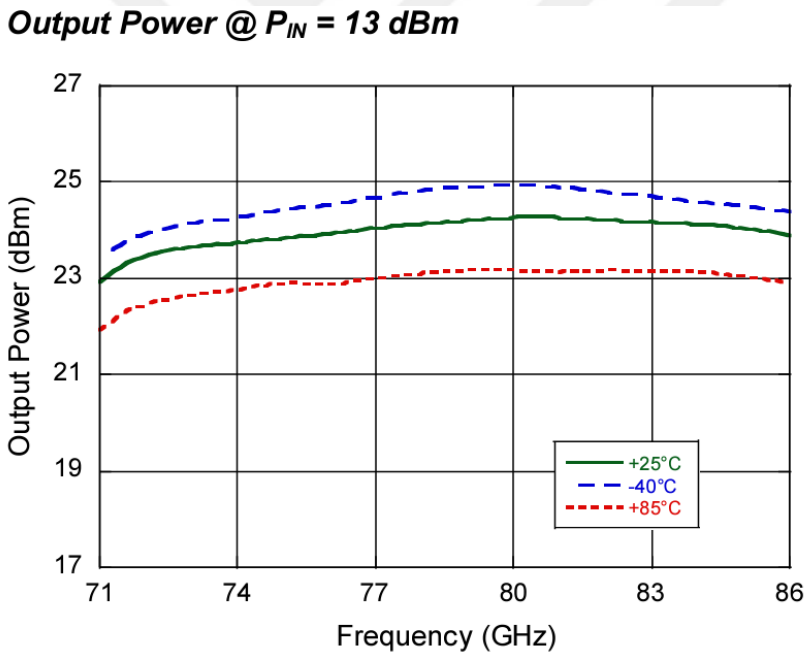



Figure 2.6: Output Power for Packaged Transistor [25]

A significant portion of these parasitic effects arises from the geometry of the wire bonds used in the packaging. In the subsequent section, a comprehensive examination of how variations in geometry affect these parasitic will be presented.

## 2.2 3D MODEL

Understanding the performance parameters of a bondwire structure can be done in different ways. One the methods is analytically modelling the wire while the other one is simulating the wire using 3D electromagnetic simulators like, HFSS and CST. In this thesis, the proposed analytical models are validated by comparing their results with simulation results. The simulations are conducted using ANSYS HFSS, where full-wave analyses were performed.

### 2.2.1 HFSS

Ansys HFSS (High-Frequency Structure Simulator) is a commercial software developed by Ansys. It is designed to solve electromagnetic (EM) structures using finite element method (FEM) solvers. The software allows users to define the geometry, material properties, and frequency ranges for their simulations. Engineers use Ansys HFSS to design and simulate high-speed, high-frequency electronic components and systems, including radar, communication systems, satellites, packaging, microchips, printed circuit boards, IoT products, and other RF devices. The tool addresses various EM issues, such as losses due to attenuation, coupling, radiation, and reflection [18].

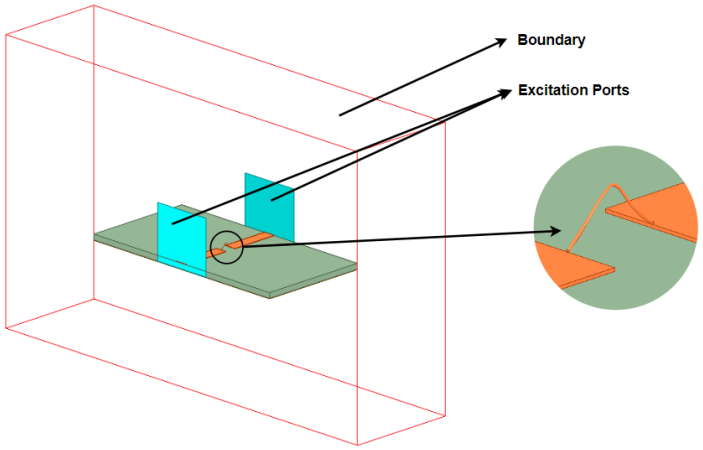



Figure 2.7: A 3D Model Geometry of bondwire from HFSS

While creating a 3D electromagnetic model using HFSS as in Figure 2.7, the steps to follow are in the Appendix A.

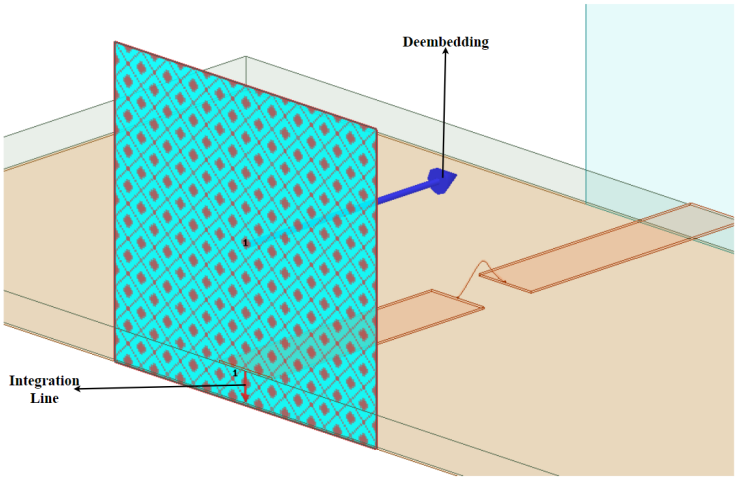



Figure 2.8: Visualization of Integration Line and Deembedding for Waveport

One of the key points here is that deembedding is performed solely to observe the S-parameters of the bondwire. The deembedding operation is illustrated in Figure 2.8. Since deembedding is a capability of the wave port, a wave port is used in the 3D modeling. . Additionally, the solution type, boundary conditions, and setup properties are detailed in the Appendix A. In summary, the selected features are provided in Table 2.1.

Table 2.1: Setup for HFSS Simulation

| | The Chosen Setting | Explanation |
|---|---|---|
| **Solution Type** | **Driven Terminal** | The driven modal solution is ideal for wave port excitation in HFSS because it precisely captures the mode propagation within waveguides, PCB traces ensuring accurate modeling of field distributions and mode interactions at the ports. |
| **Boundaries** | **Radiation Boundary** | It more accurately simulates the open-space conditions, allowing electromagnetic waves to propagate freely without artificial reflections. |
| **Excitation** | **Wave Port and Lumped Port** | Wave port is chosen to observe scattering paramaters of bondwire using deembedding feature of the port. Lumped port is also used to analyze complete model to double check the HFSS results coming from the setup with the wave ports. |
| **Solution Frequency** | **10 GHz** | It is middlle of the frequency range as suggested |
| **Delta-S** | **0.005** | It is recommended to be between 0.005-0.01 |
| **Max. # of Pass** | **20** | To ensure convergence, limit is set to high. |
| **Max. Refinement Per Pass** | **30-50 %** | Choose a maximum refinement per pass that is high enough to maintain accuracy but not so high that it significantly increases computation time. |
| **Sweep Frequency Range** | **1 MHz - 20 GHz** | The limit of the lumped model |

### 2.2.2 Q3D

Ansys Q3D Extractor includes an advanced quasi-static 3D electromagnetic field solver that uses the method of moments (MoM) and is enhanced by the fast multipole method (FMM). Proximity and skin effects, dielectric and ohmic losses, and frequency dependencies are calculated in the results. Q3D Extractor efficiently and quickly extracts 3D parameters such as resistance, both self and mutual inductance, capacitance, and conductance. Inside Q3D, there are DC and AC solvers. The DC resistance solver computes the resistance (R) matrix and can optionally generate plots of current density, voltage, and Joule power losses. The DC inductance solver uses current distributions from the DC resistance solver to calculate the low-frequency limit of the inductance (L) matrix. Q3D's capacitance solver extracts the Maxwell capacitance (C) matrix and the conductance (G) matrix for frequency-dependent lossy dielectric materials. Also, using skin effect, Q3D provides frequency dependent AC resistance and AC inductance solutions. During the package design for chips, Q3D is used to observe parasitic coming from bondwire structures [26]. In the figure below (2.9), a Q3D model of single bondwire to analyze its resistance, self inductance and capacitance to ground plane is shown.

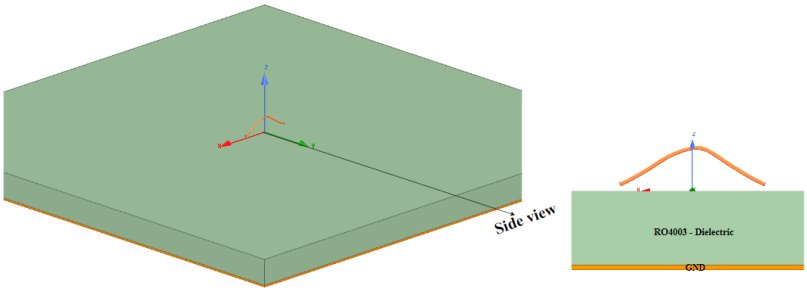



Figure 2.9: Geometry of a bondwire in Q3D

In this geometry, Figure 2.9, a signal net must be defined as the excitation line, and subsequently, the source and sink sides on this signal net should be specified. These features are explained in Appendix B.

## 2.3 Effect of Geometric Dimensions of Bondwire

For a bondwire geometry, the length and radius are critical to analyze the parasitic [27]. In order to analyze the effects, it is thought that the bondwire has a shape of Gaussian function, which is defined in Equation 2.1, as in Figure 2.10. Here, $d_{bp}$ is the distance between solder pad of bondwire, $L_{hmax}$ is the maximum heigth of the wire and $r_{bw}$ is the radius. Therefore, the analysis progresses through this structure in the next subsections.

$$f(x) = ae^{-bx^2} \tag{2.1}$$

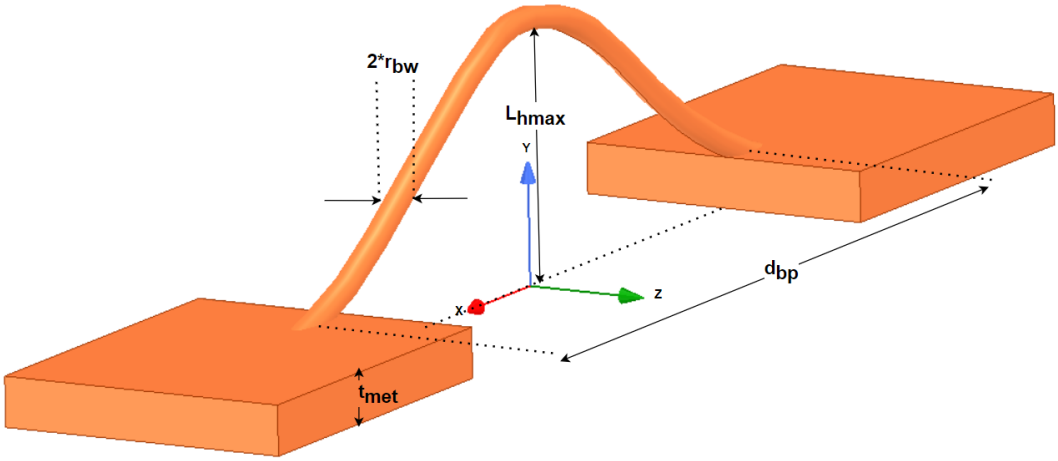



Figure 2.10: Gaussian Shaped bondwire Dimensions

### 2.3.1 Length

Length of Gaussian shaped bond wire depends on $d_{bp}$ (distance between bond wire pads) and $L_{hmax}$ (Height of the middle of the bond wire) for Gaussian Shaped bondwire:

#### 2.3.1.1 Effect of $d_{bp}$

Distance between pads of a Gaussian shaped bondwire directly increases the length of the wire. The inductance of a conductor is related to the magnetic field it creates when current flows through it. A longer wire allows for a greater portion of the magnetic field to be enclosed within the the wire, thus increasing the inductance. This result can be observed in Table 2.2 as increase in DC inductance. Also, In the Figure 2.11, Frequency dependent inductance changes can be seen for different $d_{bp}$ values. Note that decrease in inductance with the frequency is related to skin effect and it will be mentioned in the next chapter.

Table 2.2: Effect of Distance Between Pads of Bondwire ($d_{bp}$) on DC R, L, C Values of Bondwire - Q3D

| $d_{bp}$ (um) | DC Resistance - $R_{DC}$ (mOhm) | DC Inductance - $L_{DC}$ (pH) | Capacitance (fF) |
|---|---|---|---|
| 750 | 8.139 | 582.456 | 20.218 |
| 1000 | 10.080 | 795.539 | 24.202 |
| 1250 | 11.966 | 1022.072 | 28.507 |
| 1500 | 13.705 | 1256.405 | 32.666 |
| 1750 | 15.879 | 1501.804 | 37.134 |

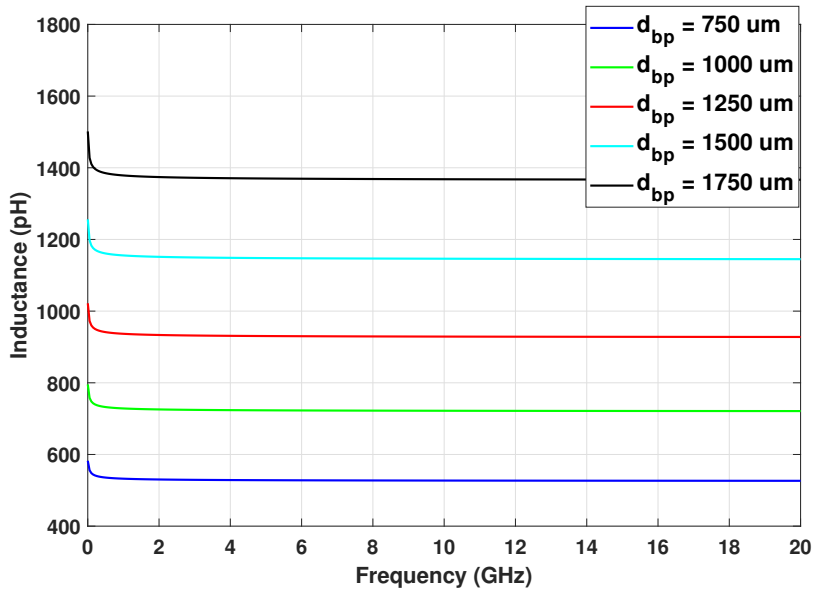



Figure 2.11: Frequency Dependent Inductance for Different $d_{bp}$ Values

The increase in the length leads to more resistance. In a longer conductor, electrons experience more scattering events as they travel through the material, which contributes to increased resistance. This effect can be observed in Table 2.2 as DC resistance and in Figure 2.12 as AC resistance.

Additionally, since the area of the conductor also increases with increasing length, charge capability of the conductor becomes higher. This means that the capacitance to ground plane increses. The effect can be observed from Table 2.2.

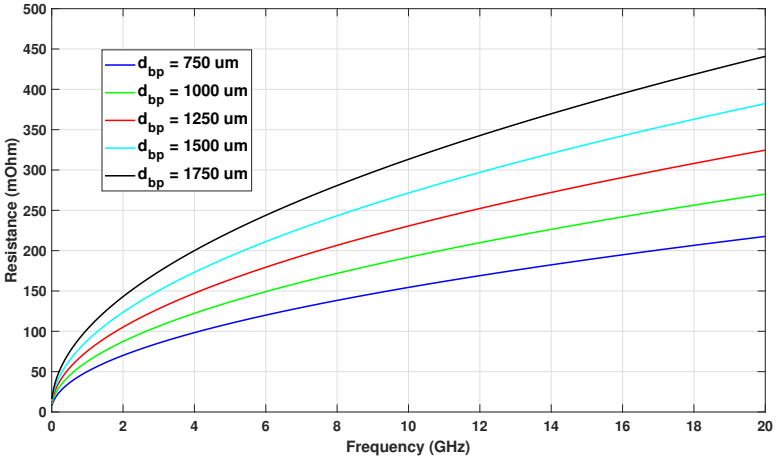



Figure 2.12: Frequency Dependent Resistance for Different ($d_{bp}$) Values

Also, in Figure 2.13, an increase in inductance introduces more loss to the wire. This is because the already high impedance of the cable increases, which also leads to a rise in return loss. The impedance increases with the rise in inductance, and the resulting insertion loss ($S_{21}$) in the wire loss as shown below.

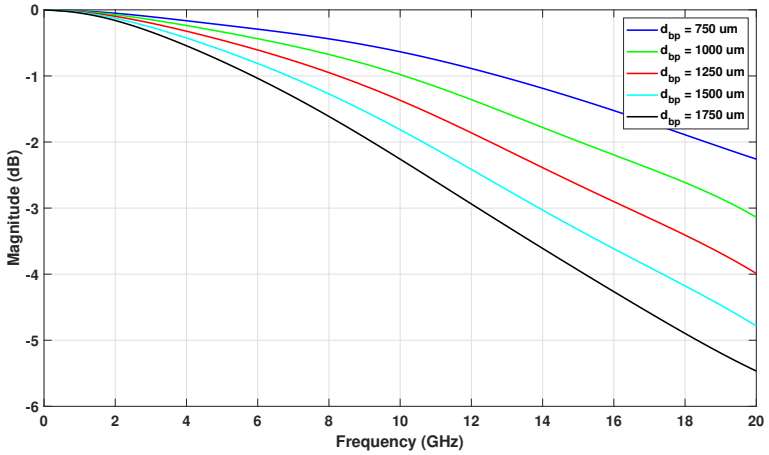



Figure 2.13: $S_{21}$ (dB) for Different $d_{bp}$ Values

#### 2.3.1.2 Effect of $L_{hmax}$

The increase in $L_{hmax}$ slightly increses the Resistance and inductance of the wire. This effect can be observed from Table2.3. Also, Figures 2.14 and 2.15 directly show the effect.

Table 2.3: Effect of Height of Bondwire ($L_{hmax}$) on DC R, L, C Values of Bondwire - Q3D

| $L_{hmax}$ (um) | DC Resistance - $R_{DC}$ (mOhm) | DC Inductance - $L_{DC}$ (pH) | Capacitance (fF) |
|---|---|---|---|
| 200 | 13.644 | 1228.599 | 33.385 |
| 300 | 13.705 | 1256.405 | 32.666 |
| 400 | 15.076 | 1316.713 | 33.074 |
| 500 | 15.842 | 1376.302 | 33.840 |
| 600 | 16.880 | 1445.683 | 34.927 |

For capacitance, in Table 2.3, almost there is not a change for different $L_{hmax}$ values. This is because the increase in length is compensated by the height of the cable from a capacitance standpoint. While the length increases, the corresponding rise in height increases the distance to the ground plane, thereby balancing the capacitance.

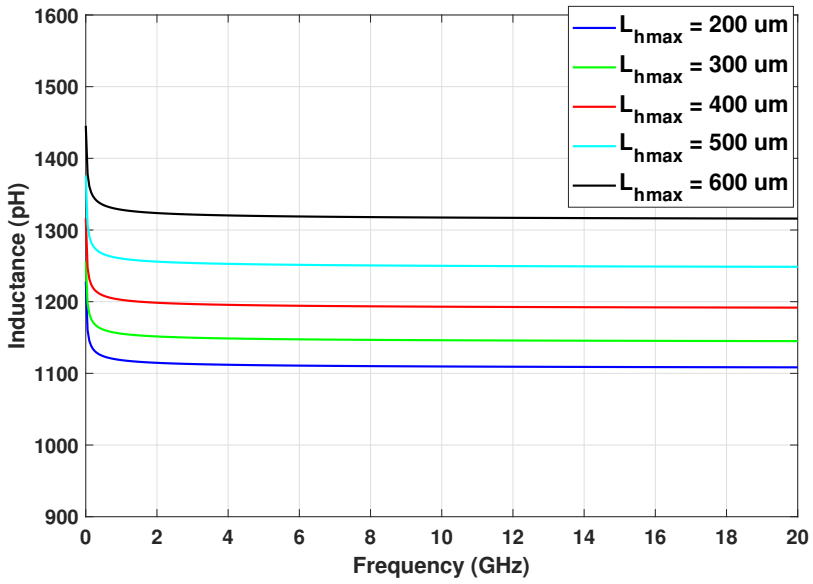



Figure 2.14: Frequency Dependent Inductance for Different $L_{hmax}$ values

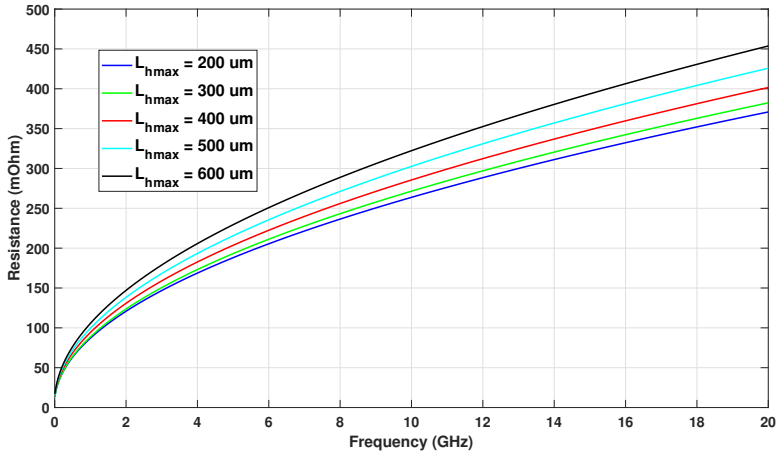



Figure 2.15: Frequency Dependent Resistance for Different $L_{hmax}$ values

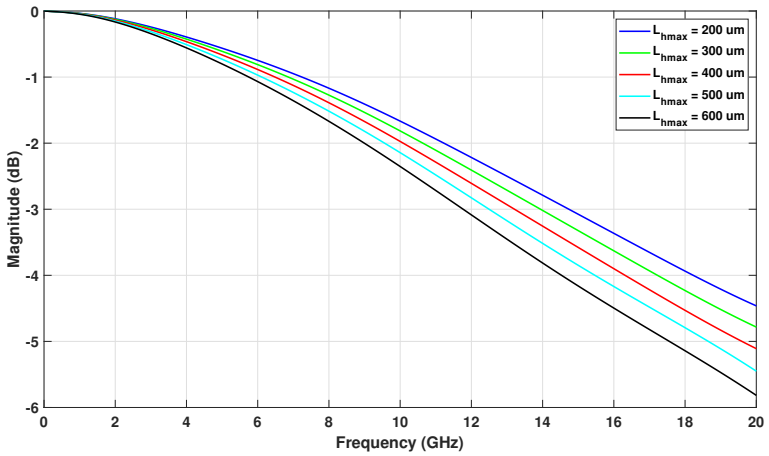



Figure 2.16: $S_{21}$ (dB) for Different $L_{hmax}$ Values

In Figure 2.16, an increase in inductance leads to high impedance and the resulting insertion loss in the wire increases.

### 2.3.2 Effect of Radius of Bond wire

The cable radius is also a significant factor. The radius directly affects the wire's resistance, inductance, and capacitance. As the wire radius increases, the wire's cross-

sectional area increases, which reduces resistance according to Ohm's Law. A similar effect occurs with inductance. The decrease in resistance is illustrated in Table 2.4, while the reduction in inductance is shown in Table 2.4 and Figure 2.17.

Table 2.4: Effect of Radius of Bondwire ($r_{bw}$) on DC R, L, C Values of Bondwire - Q3D

| $r_{bw}$ (um) | DC Resistance - $R_{DC}$ (mOhm) | DC Inductance - $L_{DC}$ (pH) | Capacitance (fF) |
|---|---|---|---|
| 12.5 | 62.651 | 1461.080 | 26.311 |
| 25 | 13.705 | 1256.405 | 32.800 |
| 37.5 | 6.220 | 1134.327 | 37.926 |
| 50 | 3.460 | 1043.129 | 42.503 |
| 62.5 | 2.232 | 974.847 | 46.853 |

Capacitance, on the other hand, might be expected to increase due to the larger charging area. These effects are demonstrated in Table 2.4.

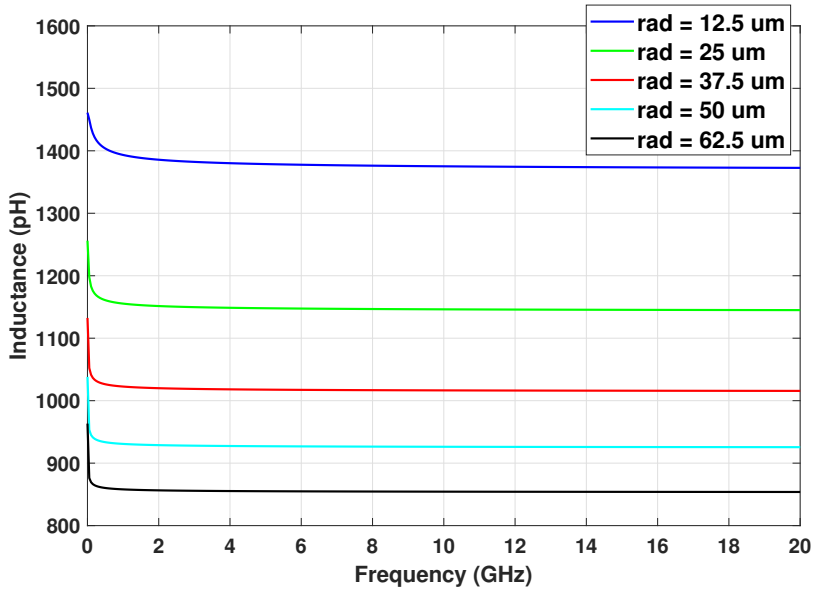



Figure 2.17: Frequency Dependent Inductance for Different Radius values

Finally, wire impedance increases with rising inductance but decreases with increasing capacitance. Consequently, the loss in the cable decreases as the radius increases, as shown in the graph below, due to the impedance becoming closer to 50 ohms.

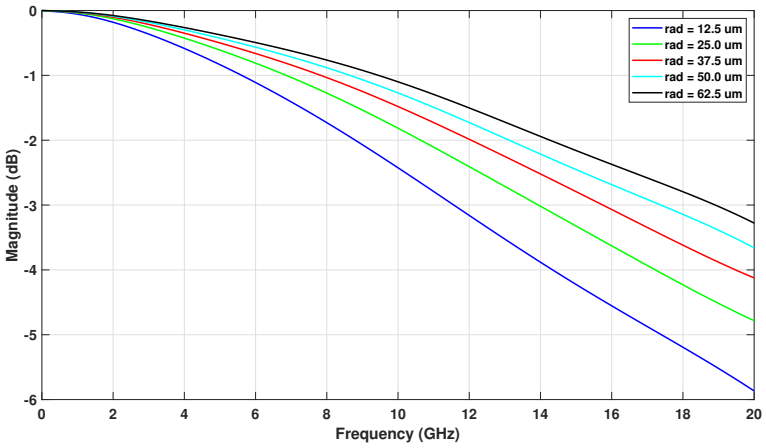



Figure 2.18: $S_{21}$ (dB) for Different Radius of Wire Values

## 2.4 Effect of Number of Bondwires

Increasing the number of bondwires in a bondwier network effectively reduces wire losses by addressing. As more bondwires are used, the current carried by each wire decreases, which lowers resistive losses because of the reduced current density in each wire. This improved distribution of current also helps to reduce high resistive losses and heat generation. Additionally, having more bondwires decreases the overall inductance of the bondwire network, as the total inductance is reduced when the current is shared among more wires. Together, these effects reduce loss in the wire network as shown in Figure 2.19. Here, it should also be noted that when two identical bondwires are used in parallel, the inductance does not decrease by half due to mutual inductance. However, the total inductance of the network decreases, which leads to a reduction in the overall loss within the network.

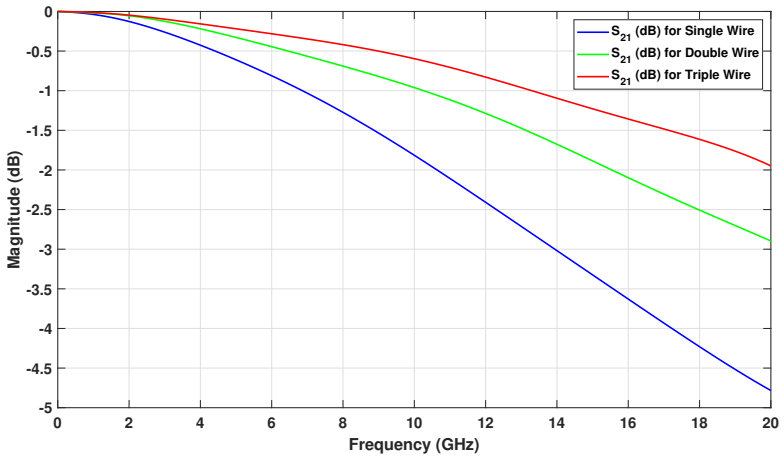



Figure 2.19: Magnitude of $S_{21}$ Comparison of Single, Double and Triple bondwire in Parallel

## 2.5 Effect of Material

In general, as a bondwire material, copper and gold are used. The choice between copper and gold for bondwires has a significant impact on electronic device performance due to their differing conductivities. Copper, known for its superior electrical conductivity, results in lower resistive losses and is often more cost-effective for various applications. On the other hand, gold, though less conductive, is valued for its excellent corrosion resistance and long-term reliability, making it ideal for high-performance and high-reliability scenarios. Gold bondwires are more resistant to oxidation and degradation, which is essential in challenging environments. Therefore, while copper bondwires offer better electrical performance with reduced resistance, gold bondwires provide enhanced durability and reliability, thereby affecting the overall performance and lifespan of the device.

# CHAPTER 3

# LUMPED ELEMENT MODEL OF WIRE-BOND

In this thesis, two different modeling approaches are discussed and compared. The first approach is based on 3-D EM simulation model, which is discussed at Chapter 2. The second approach is the equivalent lumped element model based on analytical calculations of bond wire parasitic and it will be mentioned in this chapter.

## 3.1 Single wire Model

Bond-wires can be precisely characterized using lumped elements, given the very small diameters of bond wires and their electrically short lengths relative to the operating wavelength. This characterization is effectively achieved through straightforward formulas that account for their inductance, series resistance, and capacitance to the ground plane [28]. In Figure 3.1, for a given IC component, 3D model of bondwire and its lumped element representation is shown. In Figure 3.1, R stands for DC resistance ($R_{DC}$) and resistance with frequency dependence due to the skin effect ($R_{AC}$) and L stands for DC inductance ($L_{DC}$) and frequency dependent inductance ($L_{AC}$) coming from the causality relation with $R_{AC}$, while C symbolizes the capacitance to the ground plane of the geometry of the bond wire. [29].

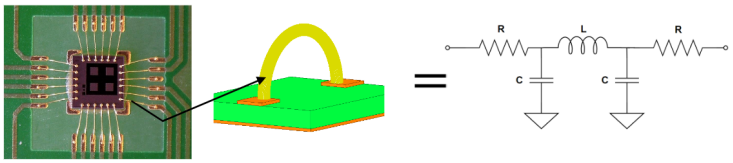



Figure 3.1: Lumped Element Model of A Single Bondwire [30]

### 3.1.1 Inductance Derivation

Inductance is a critical term that describes the link between the stored energy in a magnetic field and the current that generates the field. It includes two key concepts: loops and partial inductance. Loop inductance demands the computation of the magnetic flux ($\psi$) going through the enclosed surface of a closed current loop, requiring a return channel for the signal. Partial inductance, on the other hand, is defined as the inductance of a part of a closed current loop and is independent of determining the return path. In particular, partial inductance describes a section of wire or PCB land with inductance, as loop inductance cannot define a conductor segment without a current return path [31, 32].

#### 3.1.1.1 Partial Self-Inductance of Bond-wire

The theory of partial inductance, as defined by Ruehli [33], is essential for understanding the inductive behavior of incomplete loops and their segments. Unlike traditional loop inductance, which considers the entire loop, partial inductance focuses on defining the inductance of a specific segment of the loop. Ruehli showed that a unique inductance can be assigned to a segment of an incomplete loop, which includes both partial self-inductance and mutual inductance. In the model generated by Ruehli [33], the partial self-inductance of a conductor segment is determined by the magnetic flux that penetrates a surface area bounded by the conductor and extending to infinity. In a bondwire structure consisting of a single conductor, mutual inductance can be neglected by assuming that the other parts creating loop inductance are

located at an infinite distance. This assumption leaves only the partial self-inductance of the bondwire structure, eliminating the contribution from mutual inductance. For a given conductor segment, the total partial self-inductance consists of two parts: external inductance ($L_{ext_{ps}}$), which is due to the magnetic flux generated by the current, and internal self inductance ($L_{int_{ps}}$ ), which is affected by the skin effect [34]. This approach is fundamental in calculating bond wire inductance, taking into account the bonding geometry, material properties, and segment-specific parameters.

$$L_{partial} = L_{ext_{ps}} + L_{int_{ps}} \tag{3.1}$$

**External Self Inductance** The external partial self-inductance of a conductor is defined as the ratio of the magnetic flux and the current that generates the magnetic flux surrounding the conductor. Analytically, the external self inductance of a bondwire geometry is derived using the definition of the loop inductance. In this context, Equation (3.2) refers to $L_{loop}$, which represents the loop inductance of the closed loop current, I, shown in Figure 3.2 , whereas $\psi$ represents the magnetic flux.

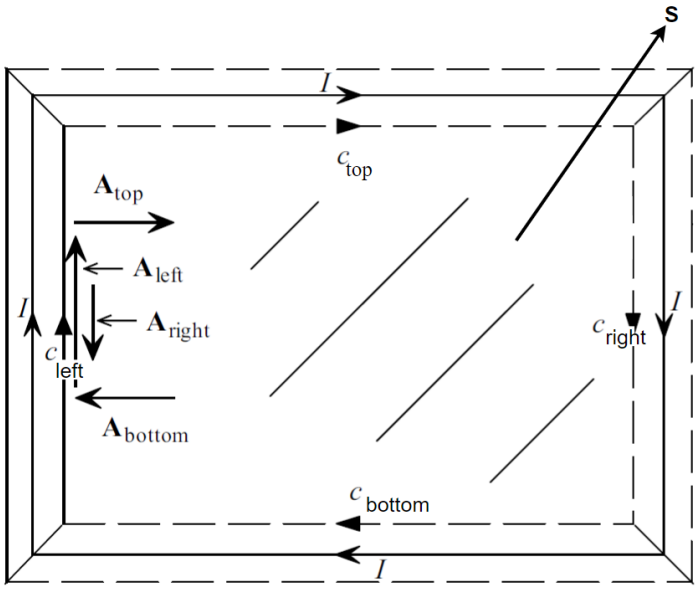



Figure 3.2: Closed Current Loop and Magnetic Potential Vectors on One of the Segments [35]

$$L_{loop} = \frac{\psi}{I} \tag{3.2}$$

$$\psi = \int_S \vec{B} \cdot d\vec{S} \tag{3.3}$$

Total magnetic flux of the loop is derived integrating magnetic flux density, B, over the surface, S, enclosed by the contour c as in Equation (3.3). $\vec{B}$ is also written in terms of magnetic potential vector, $\vec{A}$, as in Equation (3.4). Combining Equation (3.3) and Equation (3.4) and applying the Stokes Theorem, the magnetic flux can be using Equation (3.5), where $\vec{dl}$ is the small segments of the contour c.

$$\vec{B} = \nabla \times \vec{A} \tag{3.4}$$

$$\psi = \oint_c \vec{A} \cdot \vec{dl} \tag{3.5}$$

$$L_{loop} = \frac{\oint_c \vec{A} \cdot \vec{dl}}{I} \tag{3.6}$$

Equation (3.6) gives $L_{loop}$ in terms of $\vec{A}$. Here, $L_{loop}$ is the summation of the inductances of each segments, $L_{left}$, $L_{right}$, $L_{top}$, $L_{bottom}$. When it is considered about only the left side, $L_{left}$ can be defined as in Equation (3.7). Here, the contribution of the other segments to the inductance of the left side is because of mutual inductance. Here, referring to in Figure 3.2, the last two terms are zero because $\vec{A}_{top}$ and $\vec{A}_{bottom}$ are perpendicular to the small wire segments, $\vec{dl}$. If it is considered that right sided line is infinitely away from the left sided wire segment, the second term is also zero. At the end, $L_{left}$ is derived from only the magnetic potential vector which is created by the current passing through it, Equation (3.8).

$$L_{left} = \frac{\int_{c_{left}} \vec{A}_{left} \cdot \vec{dl}}{I} + \frac{\int_{c_{right}} \vec{A}_{right} \cdot \vec{dl}}{I} + \frac{\int_{c_{top}} \vec{A}_{top} \cdot \vec{dl}}{I} + \frac{\int_{c_{bottom}} \vec{A}_{bottom} \cdot \vec{dl}}{I} \tag{3.7}$$

$$L_{left} = \frac{\int_{c_{left}} \vec{A}_{left} \cdot \vec{dl}}{I} \tag{3.8}$$

This is the definition of the external partial self inductance of a wire [35]. For a wire segment carrying a DC current I and having magnetic potential vector $\vec{A}$ around, the external self inductance, $L_{ext_{ps}}$ can be calculated analytically as in Equation (3.9).

$$L_{ext_{ps}} = \frac{\int_c \vec{A} \cdot \vec{dl}}{I} \tag{3.9}$$

.

To illustrate a bond-wire geometry, current passing through it and magnetic potential vector, Figure 3.3 can be referred. The current, I, is regarded as uniformly distributed across the cross section of the conducting wire, allowing it to be depicted as a filament current along the wire's axis as in Figure 3.3.

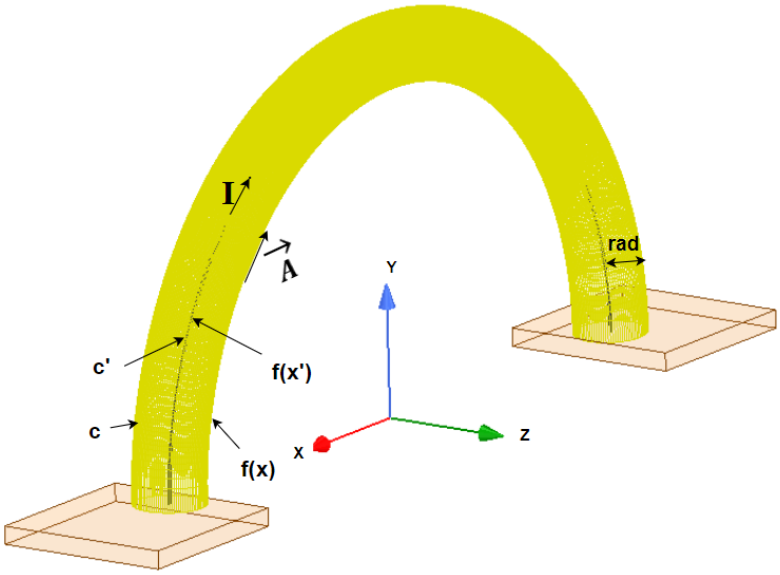



Figure 3.3: Filament Current and Created Magnetic Flux around the wire

For a random shaped bond-wire, **f(x)**, in Figure 3.3, magnetic potential vector, $\vec{A}$, created by the current passing through the center of the wire, c, is represented in Equation (3.10).

$$\vec{A} = \frac{\mu_0}{4\pi} \int_{c'} \frac{I\vec{dl'}}{R} \tag{3.10}$$

where a vector differential length of the line in the direction of the current is denoted as $\vec{dl'}$ and contains $I\vec{dl}$ ampere-meters. $R$ is the distance between the point where we are determining $\vec{A}$ and the differential current segment in Figure 3.4. Here, source parameters are represented with " $'$ " such as $\vec{dl'}$, $f(x')$, $\vec{r'}$, $\vec{r'}_1$ and $\vec{r'}_1$, while $\vec{dl}$, $f(x)$,

$\vec{r}$, $\vec{r_1}$, and $\vec{r_1}$ are denoted as measurement point parameters.

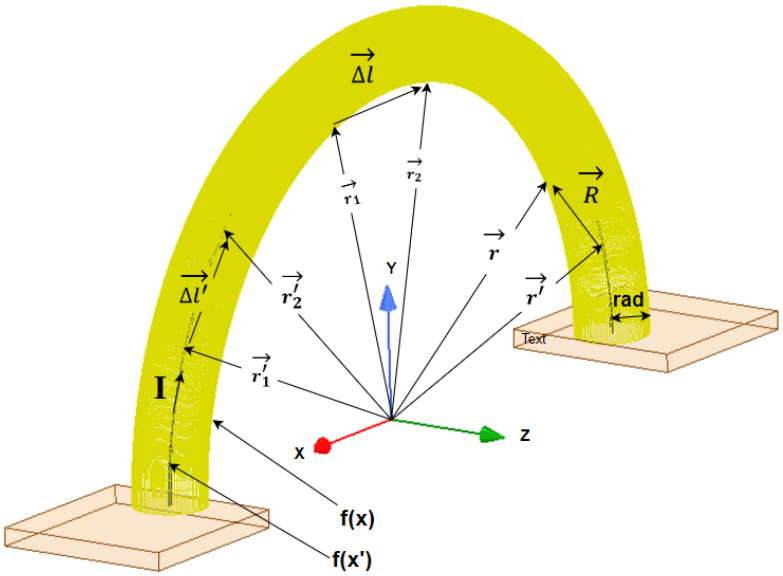



Figure 3.4: Defining Dimensions

In order to find $L_{ext_{ps}}$ through Equation (3.11), Equation (3.8) and Equation (3.10) are combined [17].

$$L_{ext_{ps}} = \frac{\mu_0}{4\pi} \int_c \int_{c'} \frac{d\vec{l'} \cdot \vec{dl}}{R} \tag{3.11}$$

The source and measurement point parameters in Equation (3.11) are derived as follows:

$$\vec{R} = \vec{r} - \vec{r'} \tag{3.12}$$

$$\vec{r} = x\vec{a_x} + f(x)\vec{a_y} + rad\vec{a_z} \tag{3.13}$$

$$\vec{r'} = x'\vec{a_x} + f(x')\vec{a_y} \tag{3.14}$$

$$R = \left|\vec{R}\right| = \sqrt{(x-x')^2 + (f(x) - f(x'))^2 + rad^2} \tag{3.15}$$

Also, from Figure 3.4, $\Delta\vec{l}$ = $\vec{r_2}$-$\vec{r_1}$ = $\Delta\vec{r}$. $\vec{r_1}$ and $\vec{r_2}$ can be defined as $\vec{r}(x)$ and $\vec{r}(x + \Delta x)$ respectively. Taking the limit as $\Delta x$ goes to 0, $\vec{dl}$ and $\vec{dl'}$ becomes:

$$\vec{dl} = \frac{d(x\vec{a_x} + f(x)\vec{a_y} + rad\vec{a_z})}{dx} dx = (\vec{a_x} + f'(x)\vec{a_y})dx \tag{3.16}$$

$$\vec{dl'} = \frac{d(x'\vec{a_x} + f(x')\vec{a_y})}{dx'}dx' = (\vec{a_x} + f'(x')\vec{a_y})dx' \tag{3.17}$$

Substituting Equations (3.12) - (3.17) into Equation (3.11), the external partial self inductance of a wire with a geometric shape of $f(x)$ is found using the Equation (3.18).

$$L_{ext_{ps}} = \frac{\mu_0}{4\pi}\int_c\int_{c'} \frac{1 + f'(x)f'(x')}{\sqrt{(x-x')^2 + (f(x) - f(x'))^2 + r_{bw}^2}}dx'dx \tag{3.18}$$

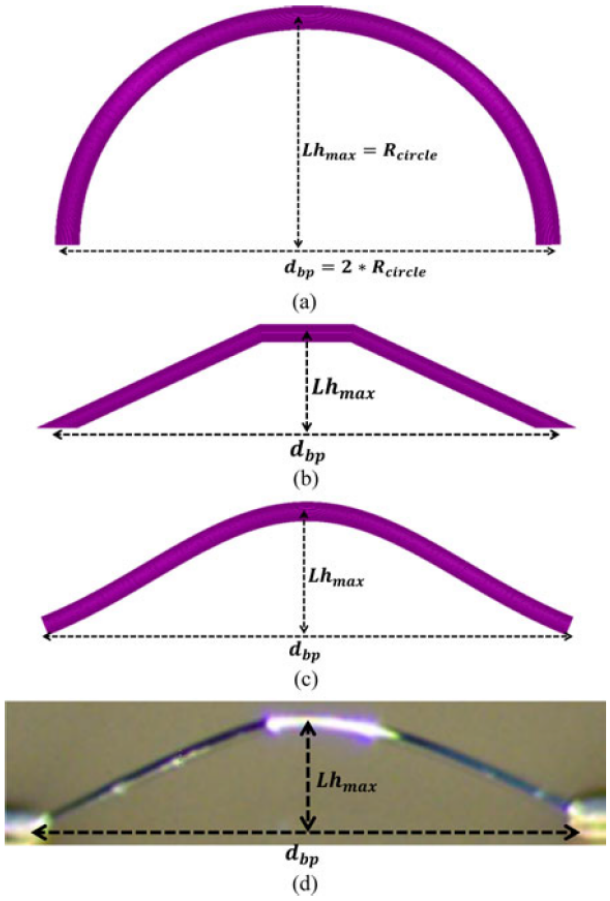



Figure 3.5: Models used to represent the shape of bond wire interconnects; (a) semi-circle; (b) JEDEC; (c) proposed model in [17]; (d) manufactured bond wire using the wedge–wedge bonding process as example.

In the literature, to define the geometry of bond wires, $f(x)$, simple shapes are available such as semicircles [14] and segment-wise lines [13]. However, these shapes do not fully reflect the actual shape of the bond wires because they rely on only a

single parameter (the radius of the circle) to capture the geometry. Combining bonding models in the literature, JEDEC standards and wedge-wedge bondwires [36], the geometry of the bond-wire is chosen as Gaussian function as depicted in Figure 3.6 [17]. Parameters of the bondwire with Gaussian function geometry $f(x)$ is given in the figure below. Here, $L_{\text{hmax}}$ is the maximum height of the bondwire, $d_{\text{bp}}$ is the distance between the pads at both ends of the bond-wire, $r_{\text{bw}}$ is the radius of wire and $t_{\text{met}}$ is the pad thickness where bond-wire is soldered on. $f(x)$ is derived in terms of the diameters of the bondwire as in the Equation (3.22) using the Equations (3.19)-(3.21).

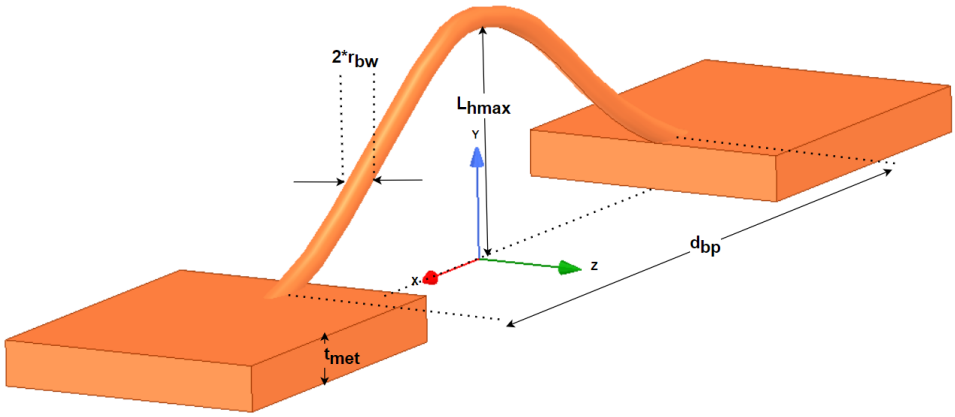



Figure 3.6: Gaussian Shaped Bond-wire Dimensions

$$f(x) = ae^{-bx^2} \tag{3.19}$$

$$\begin{aligned} x = 0; f(x) = a = L_{hmax} \\ x = \frac{d_{bp}}{2}; f(x) = L_{hmax}e^{-b(\frac{d_{bp}}{2})^2} = t_{met} \end{aligned} \tag{3.20}$$

$$b = \frac{4}{d_{bp}^2} ln(\frac{L_{hmax}}{t_{met}}) \tag{3.21}$$

$$f(x) = L_{hmax}e^{-\frac{4}{d_{bp}^2} ln(\frac{L_{hmax}}{t_{met}})x^2} \tag{3.22}$$

Therefore, to calculate $L_{\text{ext}_{\text{ps}}}$ analytically, $f(x)$ function derived for a Gaussian shaped bondwire in the Equation (3.22) is substituted into the Equation (3.18) [17]. $L_{\text{ext}_{\text{ps}}}$ is

given in Equation (3.23)

$$L_{ext_{ps}} = \frac{\mu_0}{4\pi} \int_c \int_{c'} \frac{1 + (2bL_{hmax})^2 x' x e^{-b(x'+x)^2}}{\sqrt{(x-x')^2 + (ae^{-bx^2} - ae^{bx'^2})^2 + r_{bw}^2}} dx' dx \tag{3.23}$$

**Internal Self Inductance** Internal self inductance arises from the magnetic flux inside of the conductor that a current passing through. For high frequency currents, the current distribution becomes progressively concentrated within a thin region near the conductor's surface, referred to as the skin depth, $\delta$ as seen in the Equation (3.24). As the frequency increases, the skin effect confines the magnetic field to a narrower region within the conductor, thereby decreasing the internal inductance. At very high frequencies, the total inductance of the conductor becomes nearly equivalent to the external inductance [37].

$$\delta = \frac{1}{\sqrt{\pi f \mu_0 \sigma}} \tag{3.24}$$

where, $\sigma$ is the conductivity of the wire material. In Figure 3.7, a current $I$ is passing through a wire of radius $r_{\text{bw}}$.

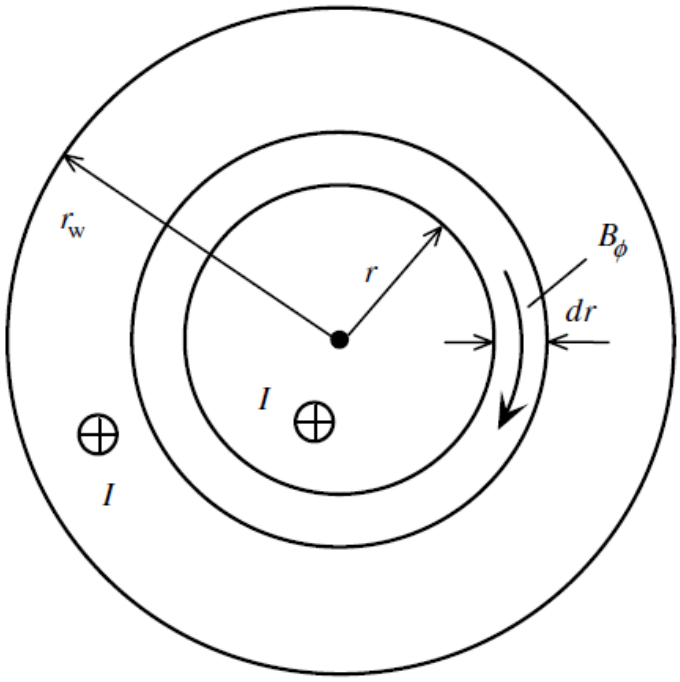



Figure 3.7: Internal Inductance Region [38]

At very low frequencies (DC), where the skin effect can be disregarded, the current density is assumed to be uniform across the entire cross-section of the conductor given in Figure 3.7. Total magnetic flux per unit length of the wire, $\psi_{\text{total}}$, is calculated through the Equations (3.25)-(3.28) [38]. Here $B_\phi$ is the magnetic flux density at a distance $r$.

$$@r < r_w; B_\phi = \frac{\mu_0 I}{2\pi r}(\frac{\pi r^2}{\pi r_{bw}^2}) = \frac{\mu_0 I r}{2\pi r_{bw}^2} \tag{3.25}$$

Total flux of a unit length segment with radius r and thickness dr :

$$d\psi = \frac{\mu_0 I r}{2\pi r_{bw}^2} dr \tag{3.26}$$

This flux occurs due to only a part of current:

$$I_{flux} = \frac{I\pi r^2}{\pi r_{bw}^2} \tag{3.27}$$

Combining the Equation (3.26) and the Equation (3.27) and doing integration over [0,$r_{bw}$], at DC/low frequencies, total flux inside of the wire of radius is found as

$$d\psi = \frac{\mu_0 I}{8\pi} \tag{3.28}$$

Therefore, at DC/low frequencies, $L_{\text{int}_{\text{DC}}}$, the internal inductance of a bond-wire of length $l_{bw}$ and radius $r_{bw}$is given in Equation (3.29) [17].

$$L_{int_{DC}} = \frac{\mu_0 l_{bw}}{8\pi} \tag{3.29}$$

At high frequencies, there is a causal relationship between internal inductance and surface resistance coming from surface impedance equation the Equation (C.1) [39]. For a function to be considered causal, it must be zero for negative times, meaning it can be expressed in terms of its even part and its Hilbert transform as in the Equation (C.3). By examining the similarity between the surface impedance equation (C.1), and the expressions for causal functions, it is concluded that the even part of the function corresponds to the surface resistance, while the Hilbert transform is related to the internal inductance as in the Equation ((C.4)). Therefore, the internal inductance

for a causal relationship is determined as the negative ratio of the Hilbert transform of the skin resistance to the frequency. This concept is examined in Appendix C in more detail. $L_{int_{AC}}$, Equation (3.33), is derived from surface resistance, $R_s$, the Equation (3.30), as follows [40], [34]:

$$R_s = \frac{1}{\sigma\delta} = \sqrt{\frac{\pi\mu_0 f}{\sigma}} \tag{3.30}$$

$$R_{AC} = \frac{R_s l_{bw}}{2\pi r_{bw}} \tag{3.31}$$

$$L_{int_{AC}} = \frac{R_{AC}}{2\pi f} \tag{3.32}$$

$$L_{int_{AC}} = \frac{R_s l_{bw}}{4\pi^2 r_{bw} f} \tag{3.33}$$

Here, $R_{AC}$ is the high frequency resistance of the bond-wire. At the end, the total partial self inductance, $L_{partial}$, of the bond-wire is calculated in two ways, depending on the frequency.If the frequency is high, total partial self inductance is the summation of $L_{ext_{ps}}$, the Equation (3.23), and $L_{int_{AC}}$, the Equation (3.33), while it is equal to summation of $L_{ext_{ps}}$ and $L_{int_{DC}}$, the Equation (3.29), @ DC / low frequencies.

$$\begin{aligned} L_{partial_{DC}} &= L_{ext_{ps}} + L_{int_{DC}} \; for \; DC/Low \; Frequencies \\ L_{partial_{AC}} &= L_{ext_{ps}} + L_{int_{AC}} \; for \; High \; Frequencies \end{aligned} \tag{3.34}$$

In Table 3.1, it is tabulated the comparison of the $L_{partial_{DC}}$ for $d_{bp}$ sweep. As it can be seen, analytically calculated $L_{partial_{DC}}$, the Equation (3.34), has a good correlation with the results of Q3D analysis. The same comparison is done for both $L_{hmax}$ anda $r_{bw}$ sweeeps. From Table 3.2 and Table 3.3,It is observed that the analytically derived Dc inductance formula accurately predicts the DC inductance value.

Table 3.1: Comparison of DC Inductance for Analytical Solution and Q3D Simulation with Different $d_{\text{bp}}$ Values for $L_{\text{hmax}} = 200\mu m$ and $r_{\text{bw}} = 12.5\mu m$

| $d_{\text{bp}}$ (um) | DC Inductance - L (pH) | |
|---|---|---|
| | Analytical Solution | Q3D |
| 750 | 660.7 | 645.8 |
| 1000 | 913.8 | 892.6 |
| 1250 | 1180.1 | 1160.0 |
| 1500 | 1460.5 | 1423.3 |
| 1750 | 1748.6 | 1702.2 |

Table 3.2: Comparison of DC Inductance for Analytical Solution and Q3D Simulation with Different $L_{\text{hmax}}$ Values for $d_{\text{bp}} = 1000\mu m$ and $r_{\text{bw}} = 12.5\mu m$

| $L_{\text{hmax}}$ (um) | DC Inductance - L (pH) | |
|---|---|---|
| | Analytical Solution | Q3D |
| 200 | 913.8 | 892.6 |
| 300 | 967.8 | 957.5 |
| 400 | 1040.9 | 1029.7 |
| 500 | 1128.6 | 1120.7 |
| 600 | 1227.2 | 1221.0 |

Table 3.3: Comparison of DC Inductance for Analytical Solution and Q3D Simulation with Different $r_{\text{bw}}$ Values for $d_{\text{bp}} = 1000\mu m$ and $L_{\text{hmax}} = 200\mu m$

| $r_{\text{bw}}$ (um) | DC Inductance - L (pH) | |
|---|---|---|
| | Analytical Solution | Q3D |
| 12.5 | 913.8 | 892.5 |
| 18.75 | 832.2 | 816.5 |
| 25 | 775.3 | 754.2 |
| 31.25 | 732.2 | 707.3 |
| 37.5 | 697.1 | 670.0 |

To compare the AC inductance, Q3D solutions are obtained up to 20 GHz for various values of $d_{bp}$, $L_{hmax}$, and $r_{bw}$, and the results from the AC inductance equation, 3.34 are compared in the graphs 3.8, 3.9 and 3.10, respectively. It was found that the analytical formula accurately predicts the AC inductance with a small margin of error. The error remains below $5\%$ for each sweep value.

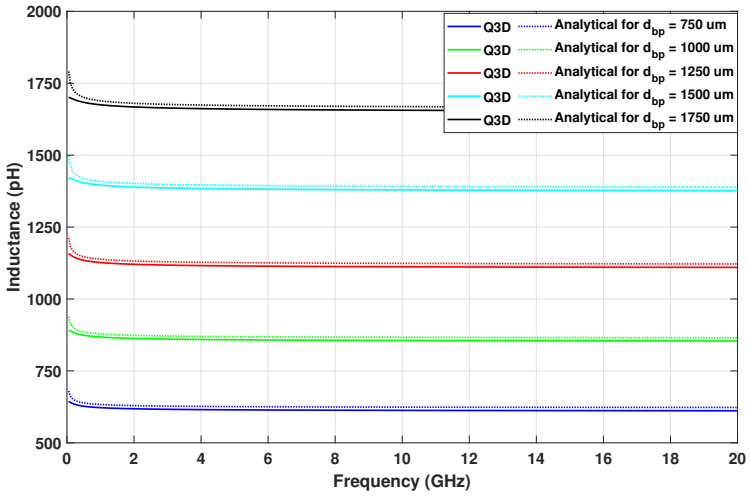



Figure 3.8: Frequency Dependent Inductance Values of Q3D and Analytical Solution for Different $d_{bp}$ Values

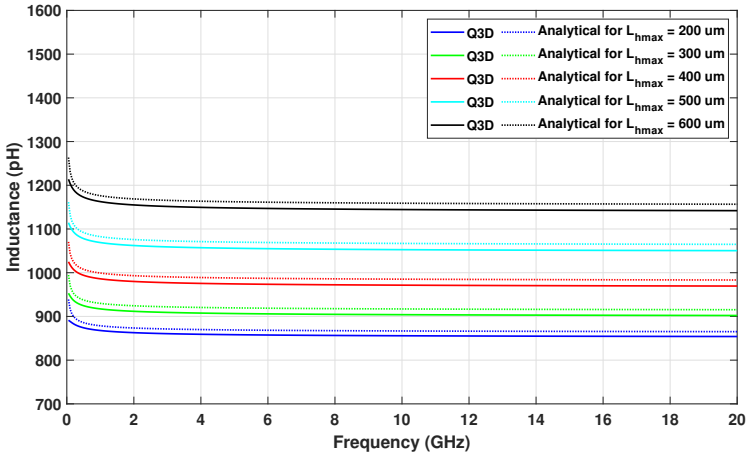



Figure 3.9: Frequency Dependent Inductance Values of Q3D and Analytical Solution for Different $L_{hmax}$ Values

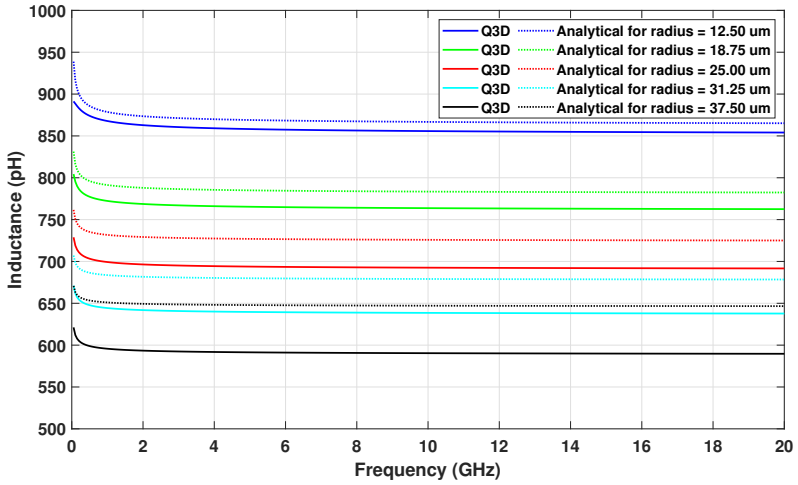



Figure 3.10: Frequency Dependent Inductance Values of Q3D and Analytical Solution for Different Radius Values

### 3.1.2 Resistance

In high-frequency applications, even though bondwires are relatively short, the increase in resistance due to the skin effect becomes significant and must be carefully considered. At DC/Low frequencies, the series resistance of a bond-wire is determined using Equation (3.35), which takes into account essential parameters such as the total length, $l_{\text{bw}}$, the radius, $r_{\text{bw}}$, the material's conductivity, $\sigma$, and the thickness of the ground plane, $t_{\text{gnd}}$ [41]. At high frequencies, the skin effect, which restricts current flow to the outer surface of the conductor, effectively reduces the conductivity of the bondwire, making it essential to calculate AC resistance of the wire. The AC resistance of a cylindrical conductor, in relation to skin depth $\delta$, is outlined in the Equation (3.36) [40]. As seen in Figure 3.11, while frequency is increased, skin depth decays, which means that the resistance that the current passing through the wire is faced is increased.

$$R_{DC} = \frac{l_{bw}(\pi r_{bw}^2 + t_{gnd})}{\pi r_{bw}^2 \sigma t_{gnd}} \tag{3.35}$$

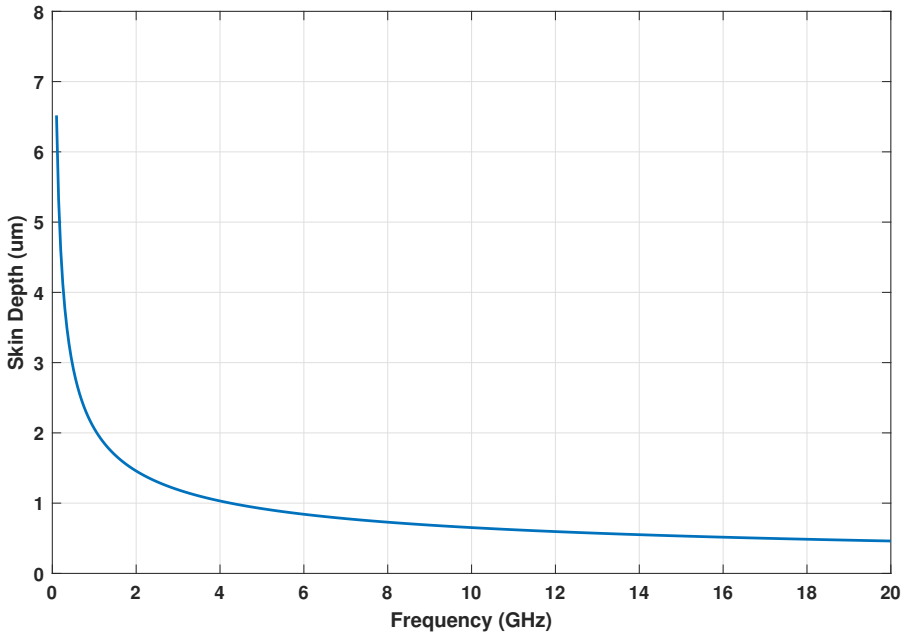



Figure 3.11: Skin Depth vs Frequency

$$R_s = \frac{1}{\sigma\delta} = \sqrt{\frac{\pi\mu_0 f}{\sigma}}$$
$$R_{AC} = \frac{R_s l_{bw}}{2\pi r_{bw}} = \frac{l_{bw}}{2r_{bw}}\sqrt{\frac{\mu_0 f}{\pi\sigma}} \tag{3.36}$$

The DC resistance calculated by the analytical formulation is compared to Q3D results for different $d_{\text{bp}}$, $L_{\text{hmax}}$ and $r_{\text{bw}}$ in Tables 3.4-3.6. As seen from the tables, there is a good correlation between the simulation and analytical results.

Table 3.4: Comparison of DC Resistance for Analytical Solution and Q3D Simulation with Different $d_{\text{bp}}$ Values for $L_{\text{hmax}} = 200\mu m$ and $r_{\text{bw}} = 12.5\mu m$

| $d_{\text{bp}}$ (um) | DC Resistance- R (mOhm) | |
|---|---|---|
| | Analytical Solution | Q3D |
| 750 | 27.9 | 29.7 |
| 1000 | 35.9 | 37.9 |
| 1250 | 44.1 | 48.8 |
| 1500 | 52.4 | 55.7 |
| 1750 | 60.8 | 64.16 |

Table 3.5: Comparison of DC Resistance for Analytical Solution and Q3D Simulation with Different $L_{\text{hmax}}$ Values for $d_{\text{bp}} = 1000\mu m$ and $r_{\text{bw}} = 12.5\mu m$

| $L_{\text{hmax}}$ (um) | DC Resistance- R (mOhm) | |
|---|---|---|
| | Analytical Solution | Q3D |
| 200 | 35.9 | 37.9 |
| 300 | 38.7 | 41.4 |
| 400 | 42.5 | 45.4 |
| 500 | 47.1 | 51.2 |
| 600 | 52.1 | 57.4 |

Table 3.6: Comparison of DC Resistance for Analytical Solution and Q3D Simulation with Different $r_{\text{bw}}$ Values for $d_{\text{bp}} = 1000\mu m$ and $L_{\text{hmax}} = 200\mu m$

| $r_{bw}$ (um) | DC Resistance- R (mOhm) | |
|---|---|---|
| | Analytical Solution | Q3D |
| 12.50 | 35.9 | 37.9 |
| 18.75 | 15.9 | 17.9 |
| 25.00 | 8.9 | 9.3 |
| 31.25 | 5.7 | 5.9 |
| 37.50 | 3.9 | 4.1 |

AC resistance is also swept for different for different $d_{\text{bp}}$, $L_{\text{hmax}}$ and $r_{\text{bw}}$ values by keeping constant other two parameters. As it can be seen in Figures 3.12-3.14, there are good correlations between the analytically derived AC resistance, Equation (3.36), and Q3D results. After such a comparison, it can be concluded that the AC and DC resistance equations are suitable to be used in the Lumped Element Modelling.

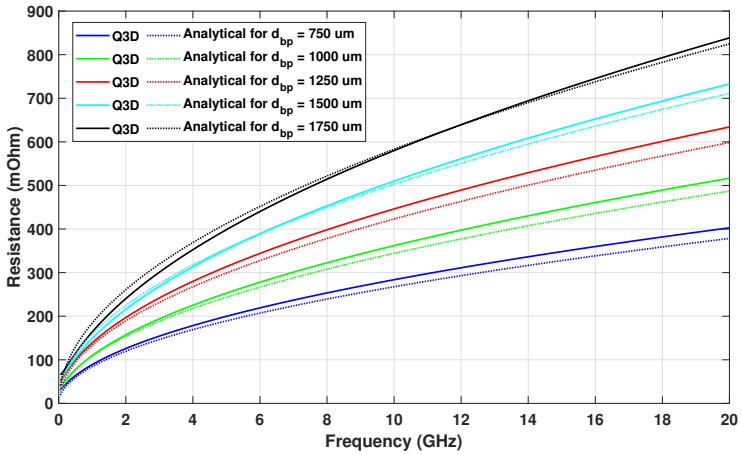



Figure 3.12: Frequency Dependent Resistance Value Comparison of Q3D and Analytical Solution For Different $d_{\text{bp}}$ Values

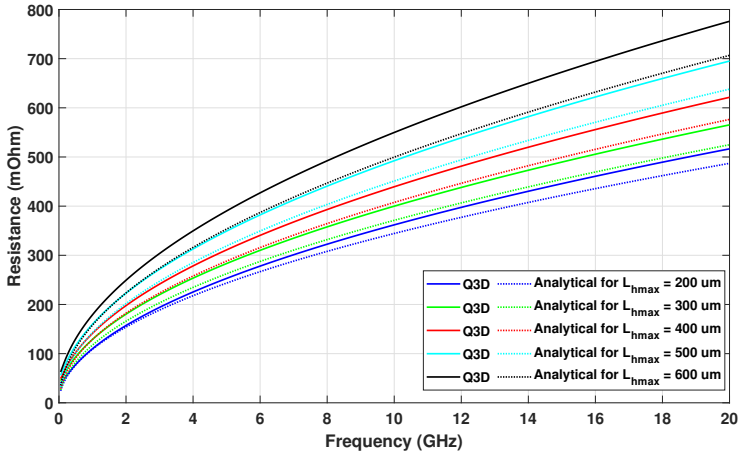



Figure 3.13: Frequency Dependent Resistance Value Comparison of Q3D and Analytical Solution For Different $L_{\text{hmax}}$ Values

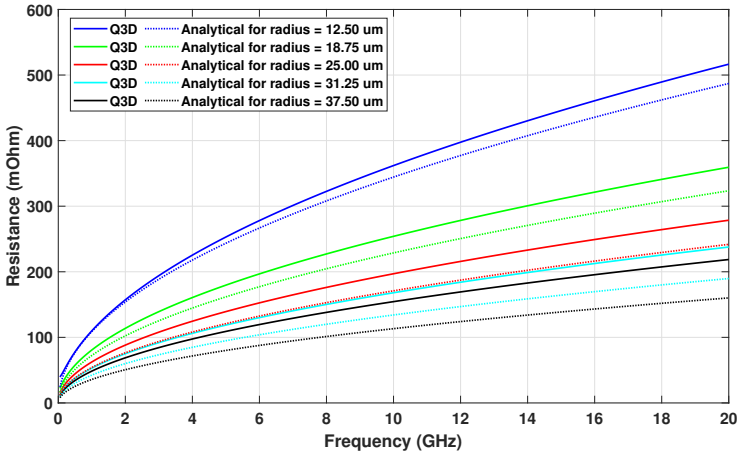



Figure 3.14: Frequency Dependent Resistance Value Comparison of Q3D and Analytical Solution For Different $r_{bw}$ Values

In order to verify frequency dependent resistance formula given in 3.36, a Bessel based formula is used [42]. Comparison of the frequency dependent resistance of a gaussian shaped bondwire is plotted in Figure 3.15. Here, using Bessel-Kernel Fundtions, a derivation is done and formula is simplified for some spesific cases. As it can be seen, simple formula, 3.36 has a good alignment with Bessel formula which is given in [42]. Also, internal inductance which is given in 3.33 is compared to the internal inductance formula given in [42]. Equation 3.33 has a perfect match with the formula derived from Bessel [42], as it can be seen in Figure 3.16.

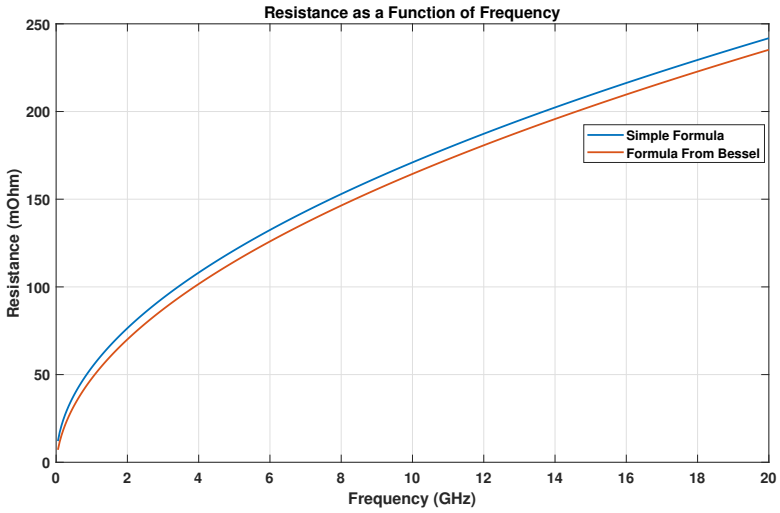



Figure 3.15: Frequency Dependent Resistance Comparison of Simple formula used in the thesis and Bessel Based Formula

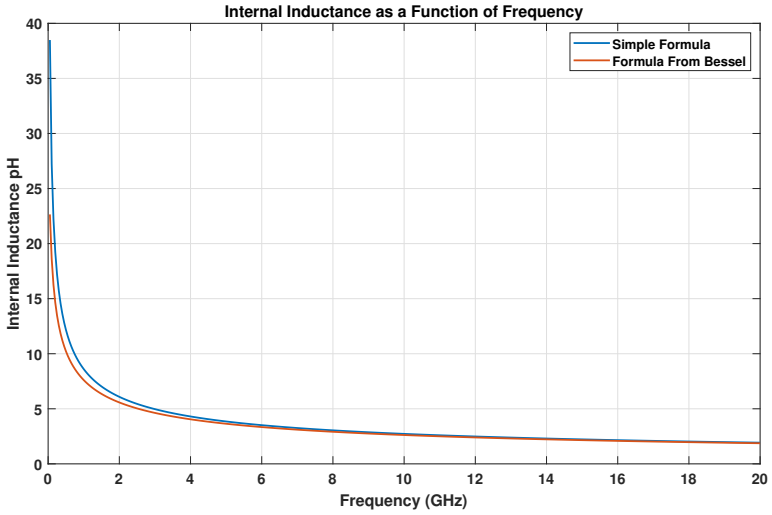



Figure 3.16: Frequency Dependent Inductance (Internal Inductance) Comparison of Simple formula used in the thesis and Bessel Based Formula

### 3.1.3 Capacitance

Capacitance to ground plane of a bond-wire has an important effect on signal transmission. Therefore, it is also should be included the lumped element model as a shunt capacitance to ground. There are different methods to calculate the capacitance of a wire. In [14], effective dielectric constant of the the medium, $\epsilon_{r_{eff}}$ is calculated using the ratio of height of air and the dielectric substrate. Then, a wire above a ground plane solution is done using $\epsilon_{r_{eff}}$. However, the solution is made of assumptions lots of assumptions, capacitance is calculated with inconsistent results.

To go further in the proposed lumped element model, the existing model found by Alimenti [43] is used after being adjusted to fit the Gaussian bond-wire shape, Figure 3.17. Derivation of the capacitance of a bond-wire is done using the Conformal Mapping equations in this section. Here, analysis are done for a circular wire with unit length over ground plane [43]. For a unit length circular wire of radius $R$, using conformal mapping, the wire geometry over ground plane is reduced to Figure 3.17. Here, because of the symmetry, the structure reduces to the geometry in Figure 3.17(a), where a magnetic wall is put on the symmetry plane y axis. In Figure 3.17(b), it is now a parallel plate capacitance with 2 medium, $\epsilon_r$ and air. It is found that changing pattern of $\epsilon_r$ is $f(v)$.

The capacitance is formulated as in Equation (3.37).

$$C_{unit_{straigth}} = \frac{2\epsilon_0}{U_0}\int_{-\pi}^{0}(1-\frac{1}{U_0}(1-\frac{1}{\epsilon_r})f(v))^{-1}dv \tag{3.37}$$

The parameters $f(v)$ and $U_0$ are [43]:

$$f(v) = \tanh^{-1}(\frac{2P}{1+P^2+\frac{1}{tan^2v}\sqrt{1+(1-P^2)tan^2v+\delta}}) \tag{3.38}$$

$$P = \frac{\frac{H}{R}}{\sqrt{(\frac{S}{R})^2-1}} \tag{3.39}$$

$$\delta = 1\ if\ v \in [0, \frac{-\pi}{2}[$$
$$\delta = -1\ if\ v \in [\frac{-\pi}{2}, -\pi[ \tag{3.40}$$

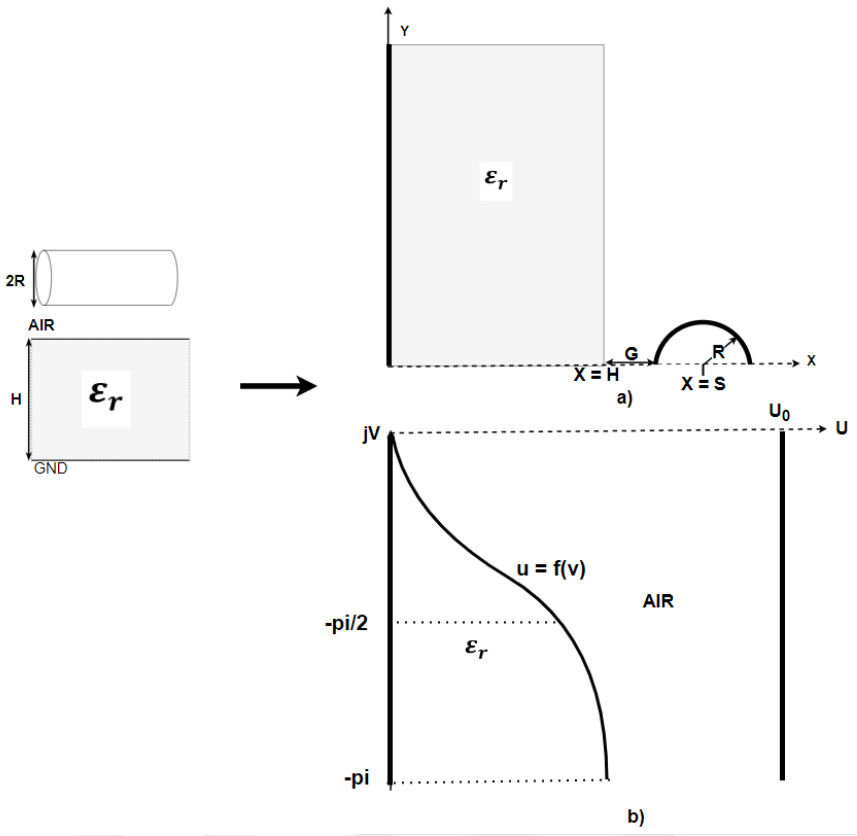



Figure 3.17: a) - b) A complex function maps of half of the circular wire with radius R

$$U_0 = \cosh^{-1}\frac{S}{R} \tag{3.41}$$

For the Gaussian shaped Bond wire with a geometry function $f(x)$, eqn. 3.22, and radius of $r_{\text{bw}}$ and dielectric thickness of $H_{\text{dielectric}}$, the formulations above, the Equations (3.38)-(3.41), turn into the followings:

$$f(v) = \tanh^{-1}\left(\frac{2P}{1+P^2+\frac{1}{tan^2 v}\sqrt{1+(1-P^2)tan^2 v+\delta}}\right) \tag{3.42}$$

$$P = \frac{\frac{H_{dielectric}}{r_{bw}}}{\sqrt{\left(\frac{H_{dielectric}+ae^{-bx^2}}{r_{bw}}\right)^2-1}} \tag{3.43}$$

$$\delta = 1 \; if \; v \in [0, \frac{-\pi}{2}[$$

$$\delta = -1 \; if \; v \in [\frac{-\pi}{2}, -\pi[ \tag{3.44}$$

$$U_0 = \cosh^{-1}(\frac{H_{dielectric} + ae^{-bx^2}}{r_{bw}}) \tag{3.45}$$

$$C_{Gaussian_{bw}} = \frac{2\epsilon_0}{U_0} \int_{\frac{-db}{2}}^{\frac{db}{2}} \int_{-\pi}^{0} (1 - \frac{1}{U_0}(1 - \frac{1}{\epsilon_r}) f(v))^{-1} dv dx \tag{3.46}$$

When the parameters are inserted into Equation (3.46), the capacitance of the Gaussian shaped bond wire is found. To verify the formulation, geometric parameters of the bond-wire are swept and the results are compared to ANSYS-Q3D simulation results in Tables 3.7-3.9. Although there are errors reaching 15 $\%$ during analysis compared to Q3D results, adding capacitance improved the lumped element model when it is added to the other effects.

Table 3.7: Comparison of Capacitance to Ground Plane of Analytical Solution and Q3D Simulation For Different $d_{bp}$ Values

| $d_{bp}$ (um) | Capacitance Between Wire and Ground Plane (fF) | |
|---|---|---|
| | Analytical Solution | Q3D |
| 750 | 13.10 | 16.32 |
| 1000 | 17.47 | 20.23 |
| 1250 | 21.84 | 24.56 |
| 1500 | 24.58 | 28.96 |
| 1750 | 30.58 | 33.22 |

Table 3.8: Comparison of Capacitance to Ground Plane of Analytical Solution and Q3D Simulation For Different $L_{hmax}$ Values

| $L_{hmax}$ (um) | Capacitance Between Wire and Ground Plane (fF) | |
|---|---|---|
| | Analytical Solution | Q3D |
| 200 | 17.47 | 20.23 |
| 300 | 17.92 | 20.63 |
| 400 | 18.14 | 21.52 |
| 500 | 18.55 | 22.73 |
| 600 | 19.57 | 24.14 |

Table 3.9: Comparison of Capacitance to Ground Plane of Analytical Solution and Q3D Simulation For Different Radius of Wire ($r_{bw}$) Values

| r_bw (um) | Capacitance Between Wire and Ground Plane (fF) | |
|---|---|---|
| | Analytical Solution | Q3D |
| 12.5 | 17.47 | 20.24 |
| 18.75 | 20.33 | 23.58 |
| 25 | 22.89 | 26.52 |
| 31.25 | 24.76 | 29.12 |
| 37.5 | 27.52 | 31.58 |

### 3.1.4 Ground Plane Effect

Effect of the PCB ground plane on bond-wire model occurs due to mutual inductance between bond-wire and ground plane. In order to calculate the mutual inductance between ground plane and wire, $M_{GND}$, image theory is used [28]. In Figure 3.18, the theory is visualized. Here, $A_1$ is the magnetic flux on the image wire which is created by the current $I_1$ passing through the wire.

$$M_{GND} = \frac{\int_c \vec{A_1} \cdot d\vec{l_2}}{I_2} \tag{3.47}$$

$$\vec{A_1} = \frac{\mu_0}{4\pi} \int_{c'} \frac{I_1 \vec{dl'_1}}{R} \tag{3.48}$$

$$I_1 = -I_2 \tag{3.49}$$

$$M_{GND} = \frac{\mu_0}{4\pi} \int_c \int_{c'} \frac{\vec{dl'_1} \cdot \vec{dl_2}}{R} \tag{3.50}$$

Similar to the derivation set of Equations (3.12)-(3.18), the mutual inductance is found using the following equation set below.

$$\vec{R} = \vec{r} - \vec{r'} \tag{3.51}$$

$$\vec{r} = x\vec{a_x} + (-f(x) - 2H_{dielectric})\vec{a_y} \tag{3.52}$$

$$\vec{r'} = x'\vec{a_x} + f(x')\vec{a_y} \tag{3.53}$$

$$R = \left|\vec{R}\right| = \sqrt{(x - x')^2 + (f(x) + f(x') + 2H_{dielectric})^2} \tag{3.54}$$

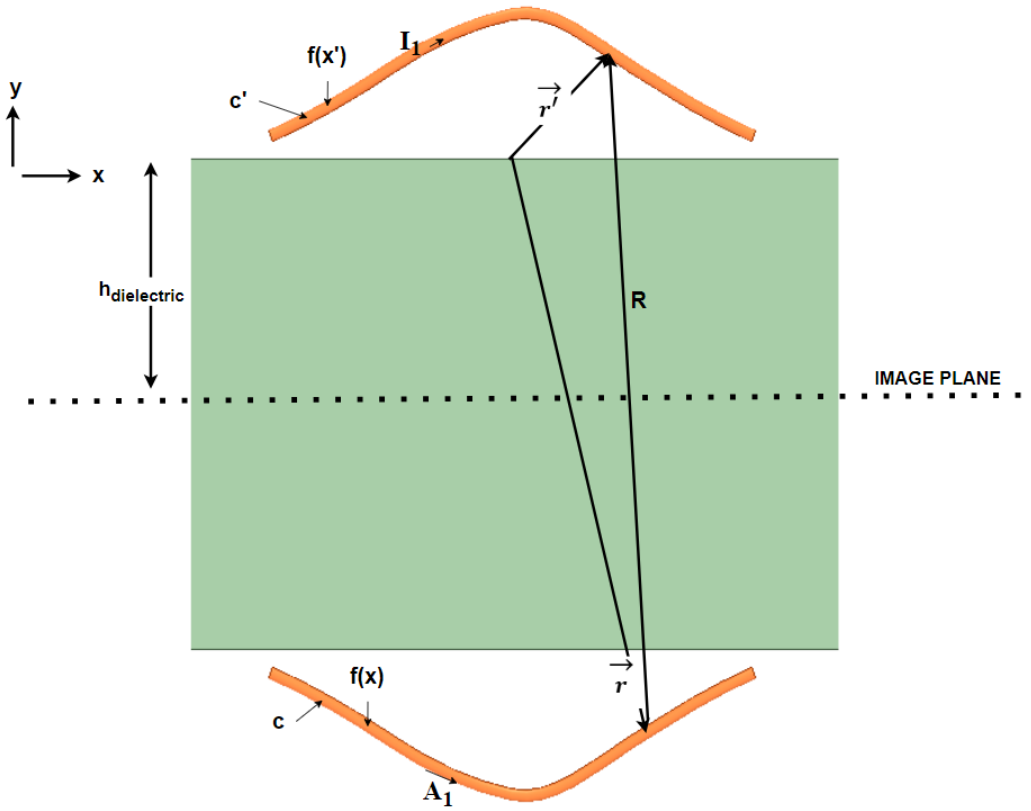



Figure 3.18: Mutual Inductance to Ground Plane Using Image Theory

$$d\vec{l}_1' = \frac{d\vec{r}'}{dx'}dx' = \vec{a_x} + f'(x')\vec{a_y} \tag{3.55}$$

$$d\vec{l}_2 = \frac{d\vec{r}}{dx}dx = \vec{a_x} - f'(x)\vec{a_y} \tag{3.56}$$

$f(x')$ is a Gaussian shaped function as mentioned in the Equation (3.22); however, for $f(x)$ function an update is needed due to dielectric thickness and 180 degree rotation. After adding these dimensions, mutual inductance between the wire and ground plane is defined in Equation (3.57).

$$M_{GND} = \frac{\mu_0}{4\pi}\int_c\int_{c'} \frac{1 - f'(x)f'(x')}{\sqrt{(x-x')^2 + (f(x) + f(x') + 2H_{Dielectric})^2}}dx'dx \tag{3.57}$$

The effect of the mutual inductance will be subtractive since the wire creates a reverse directed current in the ground plane $I_1$=$-I_2$. When the matrix in the Equation (3.58)

is solved, the effect will be realised as in Figure 3.19. Also, the effect of $L_{22}$ is ignored since the self inductance of the ground plane is too small compared to other inductance in the system.

$$\begin{bmatrix} V_1 \\ V_2 \end{bmatrix} = \begin{bmatrix} L_{11} & M \\ M & L_{22} \end{bmatrix} \begin{bmatrix} jwI_1 \\ -jwI_1 \end{bmatrix} \tag{3.58}$$

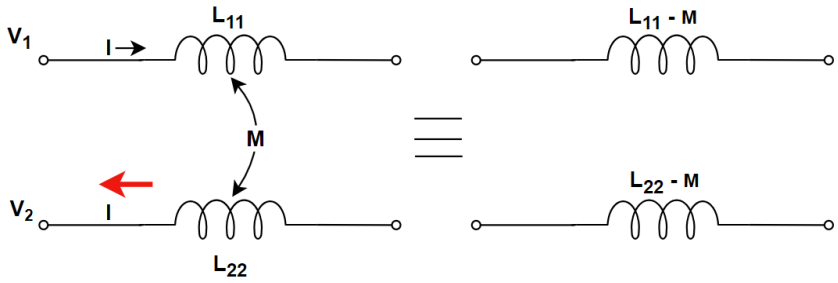



Figure 3.19: Ground Plane Mutual Inductance Effect

In order to validate the model, for different $d_{\text{bp}}$, $L_{\text{hmax}}$ and $r_{\text{bw}}$ values the the mutual inductance calculated by the analytical solution, Equation (3.58), are compared to the results coming from Q3D in Tables 3.10- 3.12, respectively. The tabulated results show that there is an excellent match between analytical solution and Q3D. Therefore, the analytical Equation 3.58 is added to the overall model.

Table 3.10: Mutual Inductances to Ground Plane of a Single Wire for Different $d_{\text{bp}}$ Values

| $d_{\text{bp}}$ (um) | Mutual Inductance to Ground Plane (pH) | |
|---|---|---|
| | Analytical Model | Q3D |
| **750** | 37.13 | 38.86 |
| **1000** | 66.03 | 68.89 |
| **1250** | 101.30 | 104.03 |
| **1500** | 143.00 | 146.81 |
| **1750** | 190.60 | 196.42 |

Table 3.11: Mutual Inductances to Gorund Plane of a Single Wire for Different $L_{hmax}$ Values

| $L_{hmax}$ (um) | Mutual Inductance to Ground Plane (pH) | |
|---|---|---|
| | Analytical Model | Q3D |
| **200** | 153.31 | 158.82 |
| **300** | 143.30 | 146.81 |
| **400** | 134.28 | 137.45 |
| **500** | 126.72 | 129.77 |
| **600** | 120.05 | 196.42 |

Table 3.12: Mutual Inductances to Ground Plane of a Single Wire for Different $r_{bw}$ Values

| $r_{bw}$ (um) | Mutual Inductance to Ground Plane (pH) | |
|---|---|---|
| | Analytical Model | Q3D |
| **12.5** | 143.47 | 148.65 |
| **25.0** | 143.30 | 146.81 |
| **37.5** | 142.71 | 145.57 |
| **50.0** | 142.56 | 144.54 |
| **62.5** | 142.50 | 143.58 |

### 3.1.5 Comparison Of The Models with HFSS Simulation Results

There are 8 lumped element models in order to analyze behavior of the single bond wire structure given in Figure 3.20. All of the models are derived analytically and compared to HFFS simulation results. In the first model, Figure 3.20(a), only DC inductance and resistance are taken into consideration. Then, to obtain the second model, Figure 3.20(b), capacitance to ground plane is added. In the third one, Figure 3.20(c) mutual inductance effect of the ground plane is also analytically included. These 3 models are made of DC effects. To improve the models, firstly, using fre-

quency dependent inductance and resistance model-4, Figure 3.20(e), is created. By adding capacitance and the mutual inductance effect of the ground plane, model-5, Figure 3.20(f), and model-6, Figure 3.20(g), are included to the comparisons respectively. Model-7 represents a DC value model in which the ground plane effect is included only as return path inductance without considering the capacitance, Figure 3.20(d). In contrast, Model-8 extends this approach to a frequency-dependent version in which frequency effects are included in the model as $L(w)$ and $R(w)$, Figure 3.20(h).

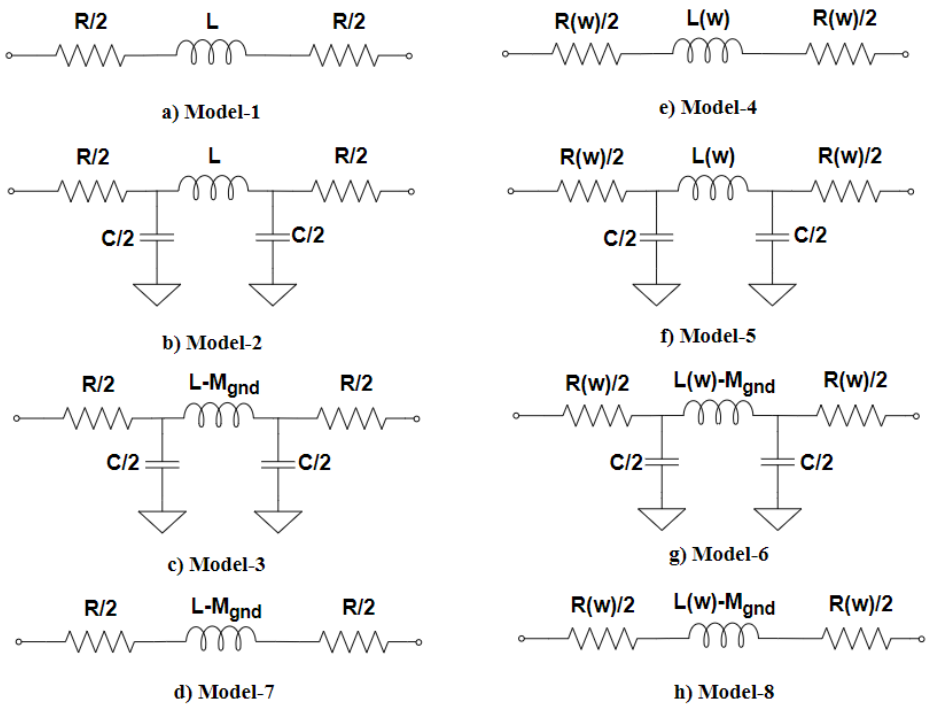



Figure 3.20: Cumulatively Created Lumped Element Models for a Single Wire

The reason for choosing the symmetric lumped element model is the observed improvement when comparing its results with HFSS outcomes, as opposed to the asymmetric model. Symmetrical and asymmetrical models are illustrated in Figure 3.21 and comparison with the HFSS results is shown in Figure 3.22. The superior performance of the symmetric model can be attributed to the geometric symmetry of the selected bond wire structure.

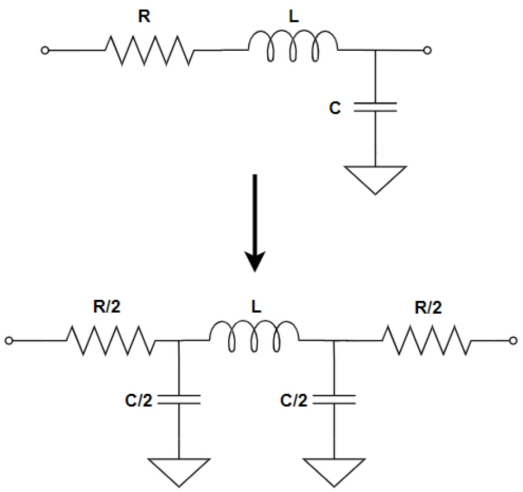



Figure 3.21: Asymmetrical and Symmetrical Models

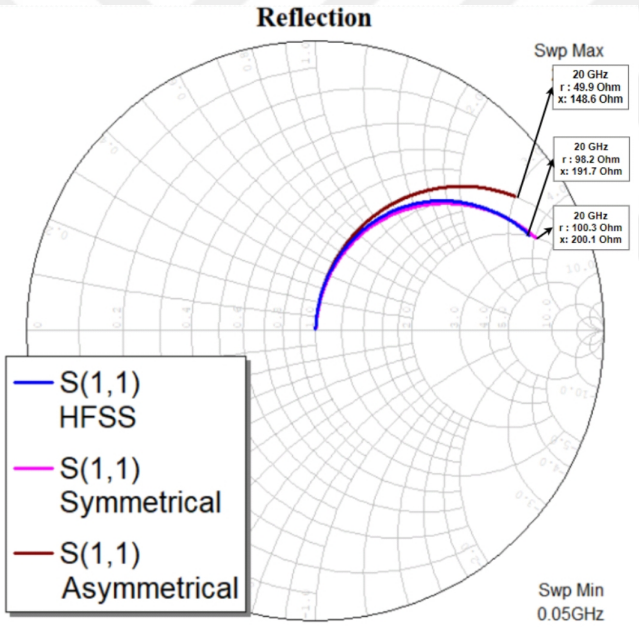



Figure 3.22: Comparison of Asymmetrical and Symmetrical Models with HFSS

For different values of geometric parameters of single bondwire different simulations are examined. In Figure 3.23, $d_{bp} = 1500\,\mu m$, $L_{hmax} = 200\,\mu m$ and $r_{bw} = 12.5\,\mu m$ case is studied. At the beginning of the plot, frequency is 0.05 GHz while it is 20 GHz at the zoomed area. For this longer wire case, the capacitance-free models, Model-1,

Model-4, Model-7, and Model-8 (Figure 3.20), deviate from the other models and the results of Q3D and HFSS. Moreover, the models that ground plane mutual inductance effect is not included, Model-2 and Model-5, estimates the inductance higher than Q3D and HFSS. Conversely, the models that capacitance and ground plane inductance are taken into account, Model-3 and Model-6, predict more accurate results than other lumped element models, Figure 3.20.

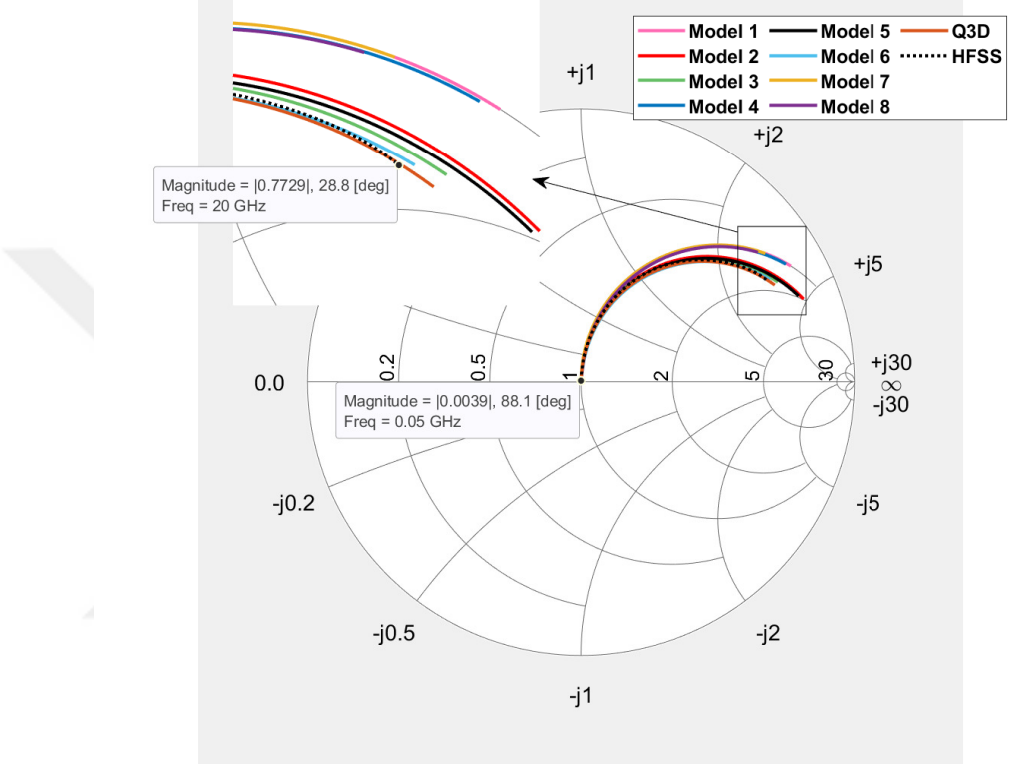



Figure 3.23: Single Wire-Comparison of $S_{11}$ on Smith Chart for $d_{bp} = 1500\,\mu m$, $L_{hmax} = 200\,\mu m$, $r_{bw} = 12.5\,\mu m$

For a shorter wire, $d_{bp} = 750\,\mu m$, $L_{hmax} = 200\,\mu m$ and $r_{bw} = 12.5\,\mu m$, same effect can be observed in Figure 3.24. Model-3 and Model-6 have much closer results to Q3D and HFSS. Despite examining the capacitance effect, Model-2 and Model-5 deviate more from the norm compared to others because they only consider the self-inductance values. These models do not take into account the ground-plane mutual inductance. Research demonstrates that the ground plane inductance reduces the total inductance, and its incorporation into Model-2 and Model-5 yields more accurate

results, leading to the creation of Model-3 and Model-6.

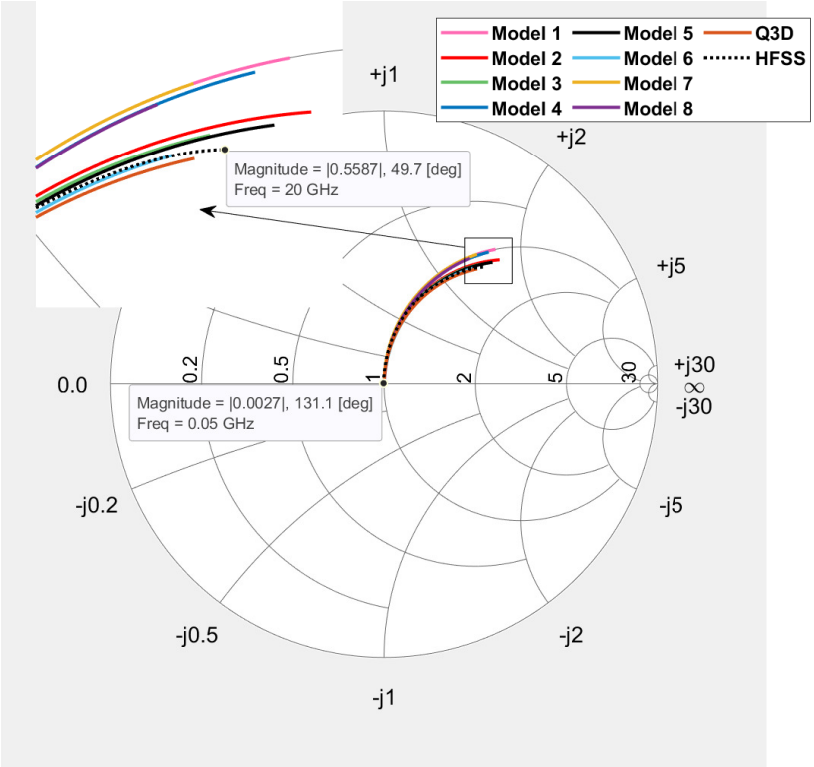



Figure 3.24: Single Wire-Comparison of $S_{11}$ on Smith Chart for $d_{bp} = 750\,\mu m$, $L_{hmax} = 200\,\mu m$, $r_{bw} = 12.5\,\mu m$

The data from Figure 3.25 to Figure 3.36 are analyzed to comprehend the behavior of the models at varying frequencies and parameters in comparison to HFSS and Q3D. The complex S11 and S21 parameters of the models and Q3D are extensively examined using the HFSS data. Normalize Mean Square Error (NMSE) with respect to HFSS results is taken as reference error formula. Formula of NMSE for $d_{bp}$, $L_{hmax}$ and $r_{bw}$ sweeps are given in equations 3.59, 3.60, 3.61 respectively [44]. Here, n symbolizes the frequency index with 0.05 Ghz steps, from 0.05 Ghz to 20 Ghz. In addition, in the equations, $\bar{y}$ represents the mean value of the HFSS results, while analytical results are symbolized by variable $x$.

$$NMSE_{d_{\text{bp}}} = \frac{\sum_{n=1}^{400}(x_n - y_n)^2}{\sum_{n=1}^{400}(y_n - \bar{y})^2} \tag{3.59}$$

$$NMSE_{L_{\text{hmax}}} = \frac{\sum_{n=1}^{400}(x_n - y_n)^2}{\sum_{n=1}^{400}(y_n - \bar{y})^2} \tag{3.60}$$

$$NMSE_{r_{bw}} = \frac{\sum_{n=1}^{400}(x_n - y_n)^2}{\sum_{n=1}^{400}(y_n - \bar{y})^2} \tag{3.61}$$

In addition, to examine the effects of change in parametric variables along the frequency band, NMSE is calculated using the formulas given in 3.62, 3.63, 3.64 for each parameter [44]. Each variable are examined in 5 steps.

$$NMSE_{frequency-d_{\text{bp}}} = \frac{\sum_{n=1}^{5}(x_n - y_n)^2}{\sum_{n=1}^{5}(y_n - \bar{y})^2} \tag{3.62}$$

$$NMSE_{frequency-L_{\text{hmax}}} = \frac{\sum_{n=1}^{5}(x_n - y_n)^2}{\sum_{n=1}^{5}(y_n - \bar{y})^2} \tag{3.63}$$

$$NMSE_{frequency-r_{\text{bw}}} = \frac{\sum_{n=1}^{5}(x_n - y_n)^2}{\sum_{n=1}^{5}(y_n - \bar{y})^2} \tag{3.64}$$

Firstly, in Figure 3.25 and Figure 3.26, the parameter $d_{\text{bp}}$ is swept from 750 $\mu$ m to 1750 $\mu$ m, while the parameters $L_{\text{hmax}}$ and $r_{\text{bw}}$ are kept constant at the values 200 $\mu$m and 12.5 $\mu$m, respectively. After that, at each $d_{\text{bp}}$ value, the NMSE of complex scattering parameters of the models against HFSS along the frequency band is plotted. In Figure 3.25 and Figure 3.26, it is observed that Model-3, and Model-6 are more accurate than other models with respect to HFSS data along $d_{\text{bp}}$ sweep, except lower values. At lower $d_{\text{bp}}$ values, Model-3, Model-6, Model-7 and Model-8 estimate lower inductance than HFSS although Model-1, Model-2, Model-4 and Model-5 estimates better values in terms of inductance.

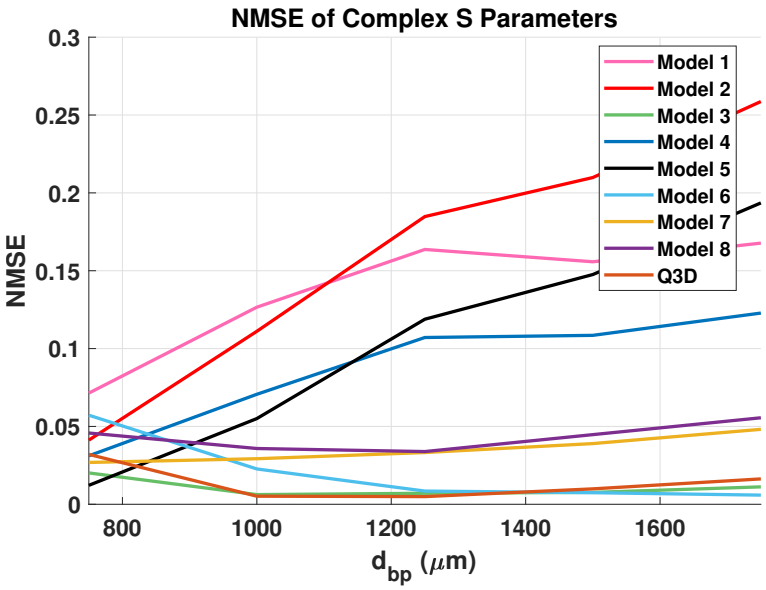



Figure 3.25: Single Wire - NMSE of Complex $S_{11}$ along Frequency Band for Different $d_{\text{bp}}$ Values - $d_{bp}$ Sweep, $L_{hmax} = 200\,\mu m$, $r_{bw} = 12.5\,\mu m$, (NMSE is calculated over 0.05-20 GHz)

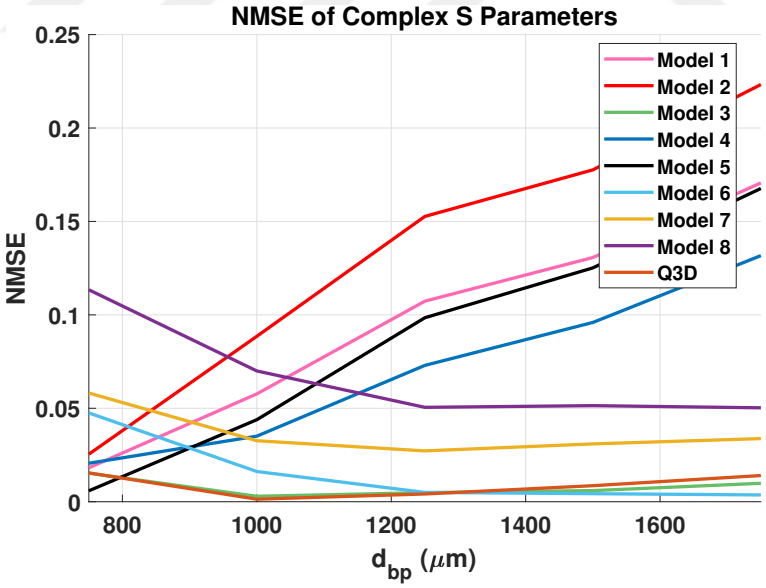



Figure 3.26: Single Wire - NMSE of Complex $S_{21}$ along Frequency Band for Different $d_{\text{bp}}$ Values - $d_{bp}$ Sweep, $L_{hmax} = 200\,\mu m$, $r_{bw} = 12.5\,\mu m$, (NMSE is calculated over 0.05-20 GHz)

In Figure 3.27 and Figure 3.28, frequency sweep is done and at each frequency, nmse is calculated for different values of $d_{\text{bp}}$ for each model. For example, at 10 GHz, $d_{\text{bp}}$ value is swept from 750 $\mu$m to 1750 $\mu$m for each model. Then, with respect to HFSS, NMSE is calculated at one frequency along the $d_{\text{bp}}$ values . This data gives that how much models deviates from HFSS when dbp is swept at one frequency. In Figure 3.27 and Figure 3.28, along the frequency band, Model-3 and Model-6 gives the best match to Q3D and HFSS results. Also, it is seen that Q3D result is reliable model to make decision since error level is at lowest values constantly. Here, at high frequencies effect of capacitance can be seen explicitly. When comparing Model-6 with Model-8, it can be observed that the effect of capacitance is beneficial at higher frequencies. The same effect has also been observed in the comparison between Model-7 and Model-3.

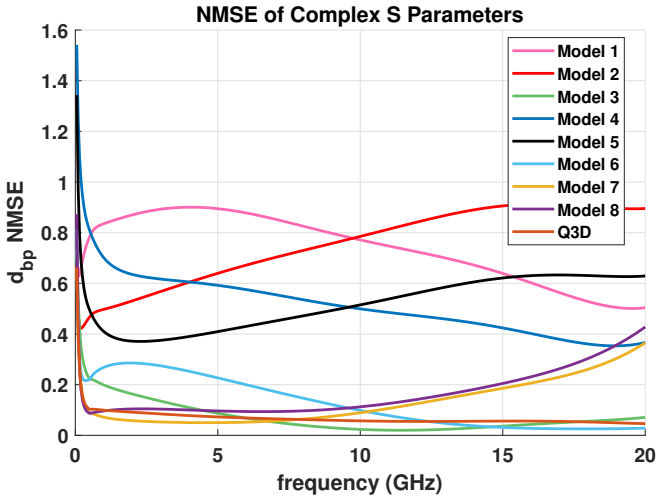



Figure 3.27: Single Wire - NMSE of Complex $S_{11}$ calculated from $d_{\text{bp}}$ sweep at A Frequency. - Frequency Sweep, $L_{hmax} = 200\,\mu m$, $r_{bw} = 12.5\,\mu m$, (NMSE is calculated over $d_{bp} = 750 - 1500\,\mu m$)

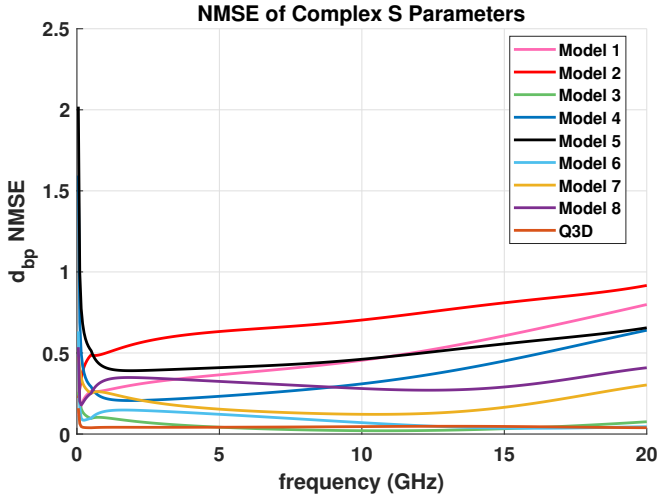



Figure 3.28: Single Wire - NMSE of Complex $S_{21}$ calculated from $d_{\text{bp}}$ sweep at A Frequency. - Frequency Sweep, $L_{hmax} = 200\,\mu m$, $r_{bw} = 12.5\,\mu m$, (NMSE is calculated over $d_{bp} = 750 - 1500\,\mu m$)

In Figure 3.29 and Figure 3.30, at one $L_{\text{hmax}}$ value, NMSE between the models and HFSS along the frequncy band is plotted. As it can be seen along the $L_{\text{hmax}}$ sweep, Mode-3 and Model-6 gives the best match to HFSS and Q3D for both real and imaginary part of $S_{11}$ and $S_{21}$. At $L_{\text{hmax}}$ sweep, Model-3 gives slightly better results than Model-6.

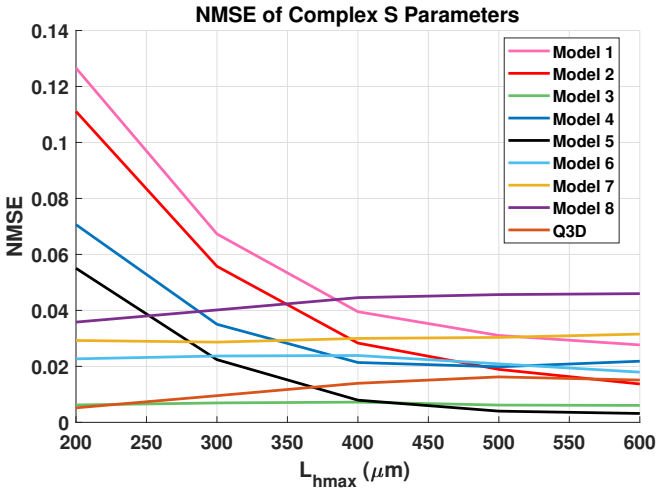



Figure 3.29: Single Wire - NMSE of Complex $S_{11}$ along Frequency Band for Different $L_{\text{hmax}}$ Values - $L_{hmax}$ Sweep, $d_{bp} = 1000\,\mu m$, $r_{bw} = 12.5\,\mu m$, (NMSE is calculated over 0.05-20 GHz)

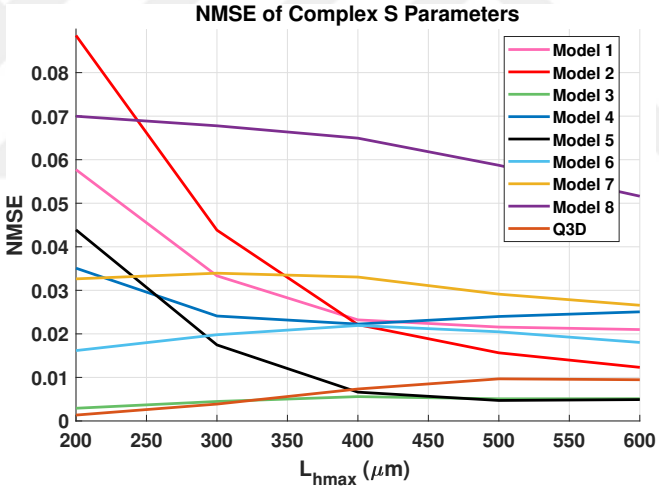



Figure 3.30: Single Wire - NMSE of Complex $S_{21}$ along Frequency Band for Different $L_{\text{hmax}}$ Values - $L_{hmax}$ Sweep, $d_{bp} = 1000\,\mu m$, $r_{bw} = 12.5\,\mu m$, (NMSE is calculated over 0.05-20 GHz)

In Figure 3.31 and Figure 3.32, at one frequency, $L_{\text{hmax}}$ is swept for each model and along $L_{\text{hmax}}$, how much models deviates form HFSS is calculated. For both $S_{11}$ and $S_{21}$, Model-3 and Model-6 have the best estimation at higher frequencies. In

HFSS analyses, deviation of the HFSS from its mean is lower around 2 GHz. Since denominator of the NMSE formula is directly related to this, NMSE is estimated larger around 2 GHz.

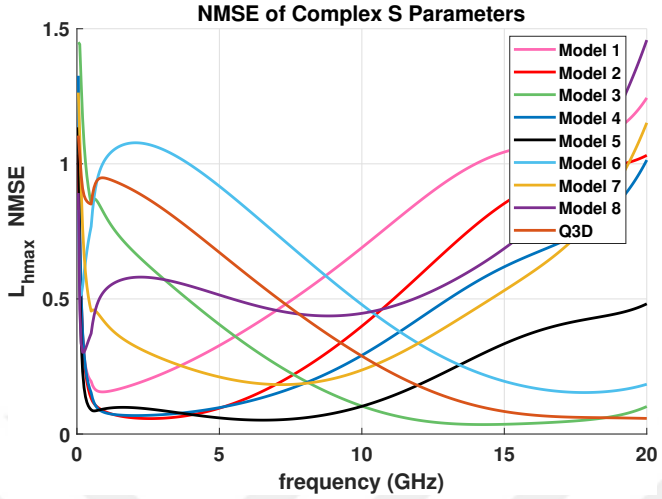



Figure 3.31: Single Wire - NMSE of Complex $S_{11}$ calculated from $L_{\text{hmax}}$ sweep at A Frequency. - Frequency Sweep, $d_{bp} = 1000\,\mu m$, $r_{bw} = 12.5\,\mu m$, (NMSE is calculated over $L_{hmax} = 200 - 600\,\mu m$)

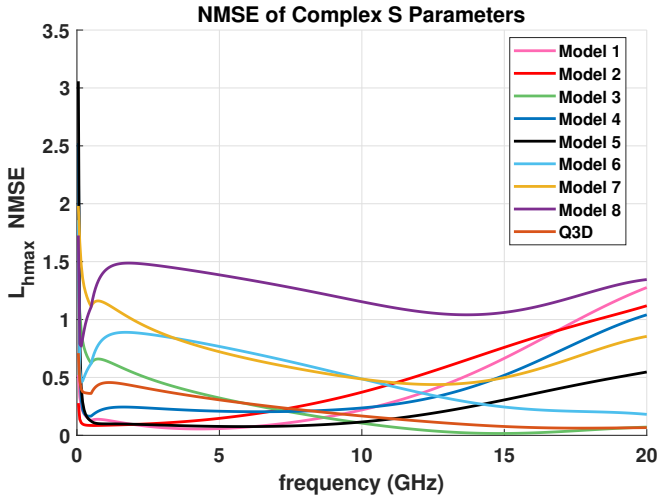



Figure 3.32: Single Wire - NMSE of Complex $S_{21}$ calculated from $L_{\text{hmax}}$ sweep at A Frequency. - Frequency Sweep, $d_{bp} = 1000\,\mu m$, $r_{bw} = 12.5\,\mu m$, (NMSE is calculated over $L_{hmax} = 200 - 600\,\mu m$)

When at a single $r_{\text{bw}}$ value, NMSE along the frequency band is calculated as in Figure 3.33 and Figure 3.34. For both real and imaginary parts of $S_{11}$ and $S_{21}$, the complicated models, Model-3 and Model-6 have better accuracy.

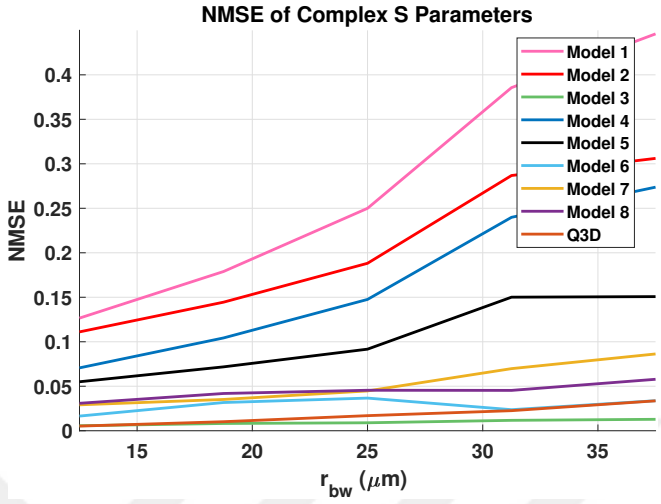



Figure 3.33: Single Wire - NMSE of Complex $S_{11}$ along Frequency Band for Different $r_{\text{bw}}$ Values - $r_{bw}$ Sweep, $d_{bp} = 1000\,\mu m$, $L_{hmax} = 200\,\mu m$, (NMSE is calculated over 0.05-20 GHz)

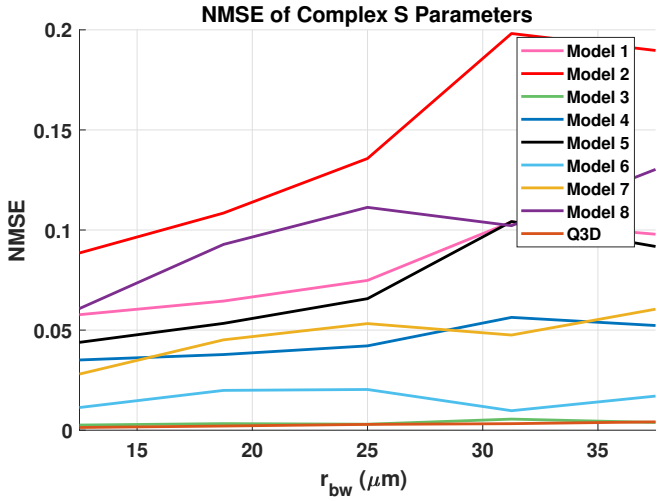



Figure 3.34: Single Wire - NMSE of Complex $S_{21}$ along Frequency Band for Different $r_{\text{bw}}$ Values - $r_{bw}$ Sweep, $d_{bp} = 1000\,\mu m$, $L_{hmax} = 200\,\mu m$, (NMSE is calculated over 0.05-20 GHz)

In Figure 3.35 and 3.36, NMSE of the complex $S_{11}$ calculated for $r_{\text{bw}}$ sweep at A Frequency. Frequency effect is also seen in this parameter. At high frequencies, since capacitance is taken into account results of Model-3 and Model-6 are closer to HFSS and Q3D. However, there is deviation at lower frequencies because of denominator of NMSE formula. Here, HFSS deviates from its mean larger than other frequencies. Therefore, this creates a peak around 2 GHz for Model-3 and 6. In HFSS analyses, deviation of the HFSS from its mean is lower around 2 GHz. Since denominator of the NMSE formula is directly related to this, NMSE is estimated larger around 2 GHz.

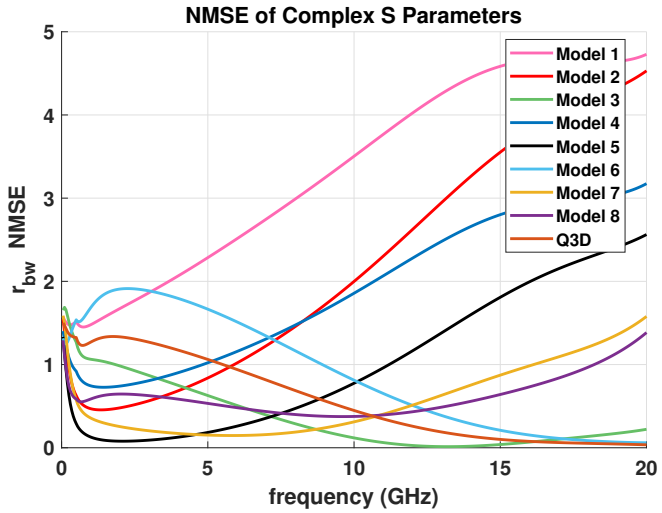



Figure 3.35: Single Wire - NMSE of Complex $S_{11}$ calculated from $r_{\text{bw}}$ sweep at A Frequency. - Frequency Sweep, $d_{bp} = 1000\,\mu m$, $L_{hmax} = 200\,\mu m$, (NMSE is calculated over $r_{bw} = 12.5 - 37.5\,\mu m$)

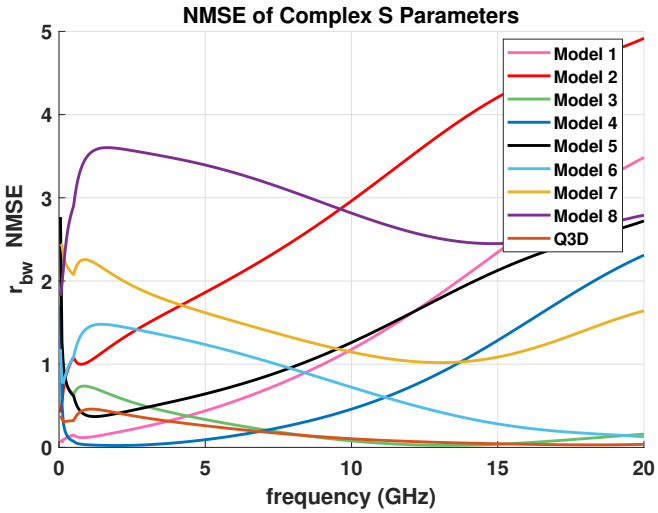



Figure 3.36: Single Wire - NMSE of Complex $S_{21}$ calculated from $r_{\text{bw}}$ sweep at A Frequency. - Frequency Sweep, $d_{bp} = 1000\,\mu m$, $L_{hmax} = 200\,\mu m$, (NMSE is calculated over $r_{bw} = 12.5 - 37.5\,\mu m$)

This section can be concluded as follows: Single-wire analyses are examined both along the frequency, keeping the parameters constant, and along the sweep values of the parameters, keeping the frequency constant. Observations show that Model-3 and Model-6 produce results that are closer to Q3D and HFSS. This is because these models take into account capacitance and ground-plane mutual inductance. In cases where capacitance is not taken into account but ground plane inductance is taken into account, Model-7 and Model-8 gave good results when the wire length is short. However, as the frequency increased and the wire length became longer, the lack of capacitance increased the error margin of the models. In cases where capacitance is taken into account and ground plane inductance is not taken into account, Model-2 and Model-5 gave better results when the wire length is short. This is because other models underestimate the inductance value. Better results are given by Model-5 when the wire length is short. Inductance values are underestimated by other models. The total inductance of Model-2 and Model-5 does not subtract the ground plane inductance, leading to results that are closer to the values calculated by HFSS. Serious distortions are observed in these models when the wire length increases and the frequency rises, making them unreasonable models.

As it is mentioned in Chapter 2, HFSS makes full wave analysis while Q3D simulator is a quasistatic solver. The lumped element models in Figure 3.20 are also analyzed in static case. Therefore, to be more meaningful, NMSE of the lumped element models are also plotted with respect to Q3D results in Figure3.37, Figure 3.38 and Figure 3.39. For these figures, at a constant geometric parameter, NMSE value is calculated along the frequency band. It can be said that Model-3 and Model-6 are the most closer results to Q3D results. In Figure 3.37 and Figure 3.38, when the length of the bondwire increases with increasing $d_{\text{bp}}$ and $d_{\text{bp}}$ respectively , Model-6 gives closer results to Q3D. Also, in Figure 3.39, when the radius of the bondwire is increased, error between Model-6 and Q3D is getting smaller than that of Model-3. In fact, these are expected results since Model-6 concerns about frequency dependent parameters such as resistance and inductance.

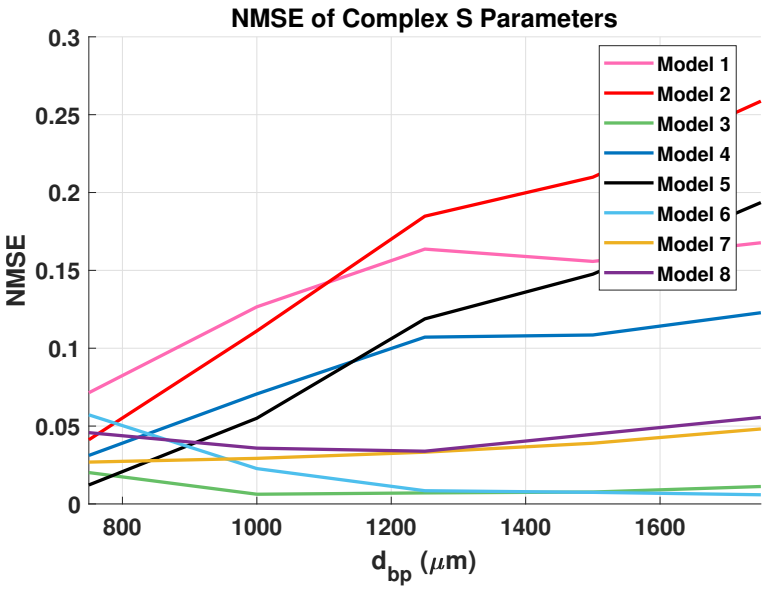



Figure 3.37: Single Wire - NMSE of Complex $S_{11}$ with respect to Q3D for $d_{\text{bp}}$. - $d_{bp}$ Sweep, $L_{hmax} = 200\,\mu m$, $r_{bw} = 12.5\,\mu m$, (NMSE is calculated over 0.05-20 GHz)

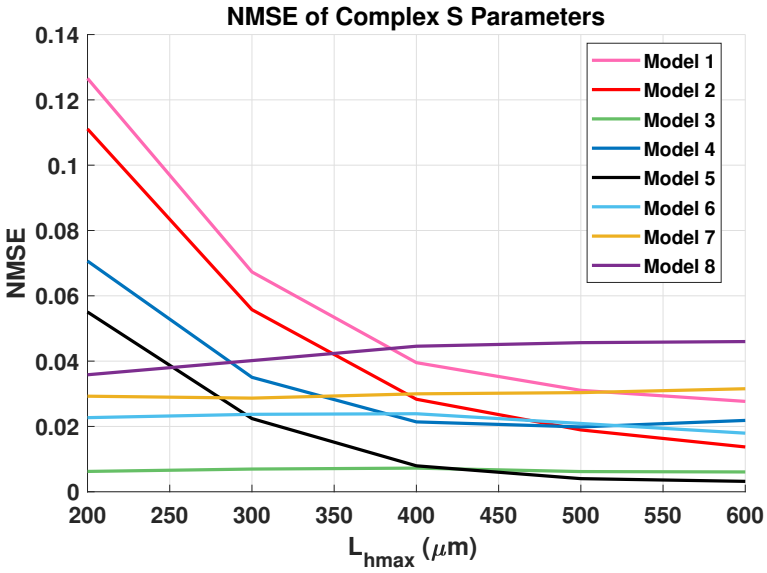



Figure 3.38: Single Wire - NMSE of Complex $S_{11}$ with respect to Q3D for $L_{\text{hmax}}$. - $L_{hmax}$ Sweep, $d_{bp} = 1000\,\mu m$, $r_{bw} = 12.5\,\mu m$, (NMSE is calculated over 0.05-20 GHz)

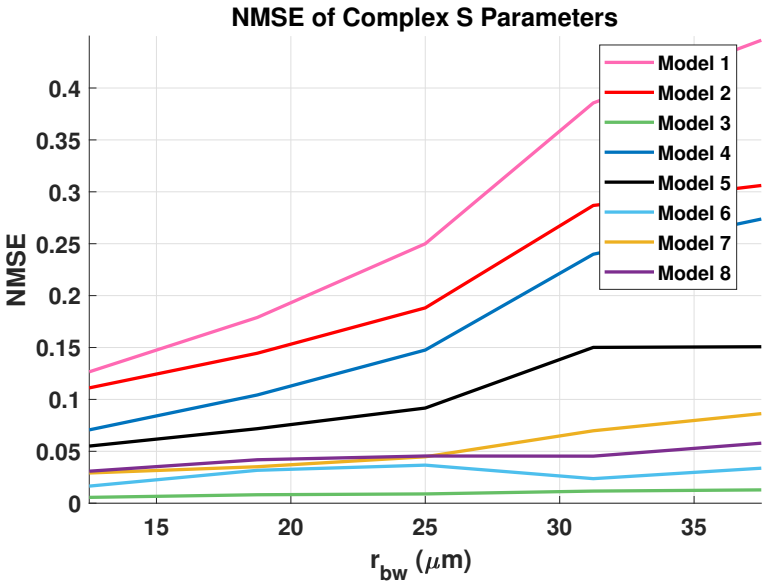



Figure 3.39: Single Wire - NMSE of Complex $S_{11}$ with respect to Q3D for $r_{\text{bw}}$. - $r_{bw}$ Sweep, $d_{bp} = 1000\,\mu m$, $L_{hmax} = 200\,\mu m$, (NMSE is calculated over 0.05-20 GHz)

## 3.2 Double Wire Model

### 3.2.1 Mutual inductance of Parallel Bond-wires Carrying a Signal

Mutual inductance is a measure of how the magnetic field generated by the current in one of the wire induces a voltage in the other wire. In Figure 3.40, a double wire system is shown. These are identical wires, that is, current, dimensions and magnetic flux induced at each other are the same. For such a system, mutual inductance between wires, $L_{mutual_{double}}$, is derived as follows:

$$L_{mutual_{double}} = \frac{\int_c \vec{A_1} \cdot \vec{dl_2}}{I_2} \tag{3.65}$$

$$\vec{A_1} = \frac{\mu_0}{4\pi} \int_{c'} \frac{I_1 \vec{dl'_1}}{R} \tag{3.66}$$

$$I_1 = I_2 \tag{3.67}$$

$$L_{mutual_{double}} = \frac{\mu_0}{4\pi} \int_c \int_{c'} \frac{\vec{dl'_1} \cdot \vec{dl_2}}{R} \tag{3.68}$$

Here, $\vec{A_1}$ is the magnetic flux around second wire created by the current, $I_1$, passing through the first wire. Using the same path while deriving Equation (3.18), mutual inductance is found as in Equation (3.75).

$$\vec{R} = \vec{r} - \vec{r'} \tag{3.69}$$

$$\vec{r} = x\vec{a_x} + f(x)\vec{a_y} + (r_{bw} + p)\vec{a_z} \tag{3.70}$$

$$\vec{r'} = x'\vec{a_x} + f(x')\vec{a_y} \tag{3.71}$$

$$R = \left|\vec{R}\right| = \sqrt{(x - x')^2 + (f(x) - f(x'))^2 + rad^2} \tag{3.72}$$

$$\vec{dl'_1} = \frac{\vec{dr'}}{dx'} dx' = \vec{a_x} + f'(x')\vec{a_y} \tag{3.73}$$

$$\vec{dl_2} = \frac{\vec{dr}}{dx} dx = \vec{a_x} + f'(x)\vec{a_y} \tag{3.74}$$

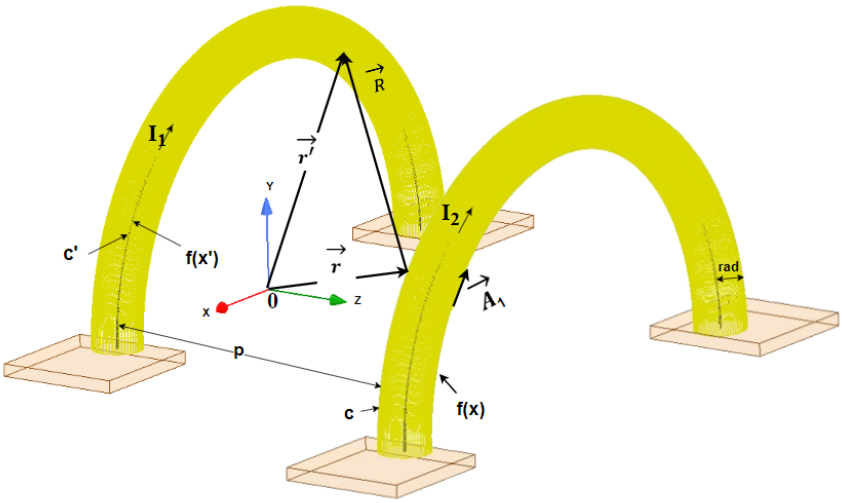



Figure 3.40: Mutual Inductance Derivation

Since $f(x)$ is a Gaussian shaped function as mentioned in Equation (3.22), mutual inductance between 2 Gaussian shaped bond-wire is calculated using the equation below.

$$L_{mutual_{double}} = \frac{\mu_0}{4\pi} \int_c \int_{c'} \frac{1 + (2bL_{hmax})^2 x' x e^{-b(x'+x)^2}}{\sqrt{(x-x')^2 + (ae^{-bx^2} - ae^{bx'^2})^2 + (r_{bw}+p)^2}} dx' dx \tag{3.75}$$

The effect of the mutual inductance will be additive since both o the wires are identical and they transfers to signal to the same side. When matrix in Equation (3.76) is solved, the effect will be realised as in Figure 3.41. $V_1$=$V_2$ and $I_1$=$I_2$ and $L_{11}$=$L_{22}$=$L$ because of equivalence.

$$\begin{bmatrix} V_1 \\ V_2 \end{bmatrix} = \begin{bmatrix} L_{11} & M \\ M & L_{22} \end{bmatrix} \begin{bmatrix} jwI_1 \\ jwI_2 \end{bmatrix} \tag{3.76}$$

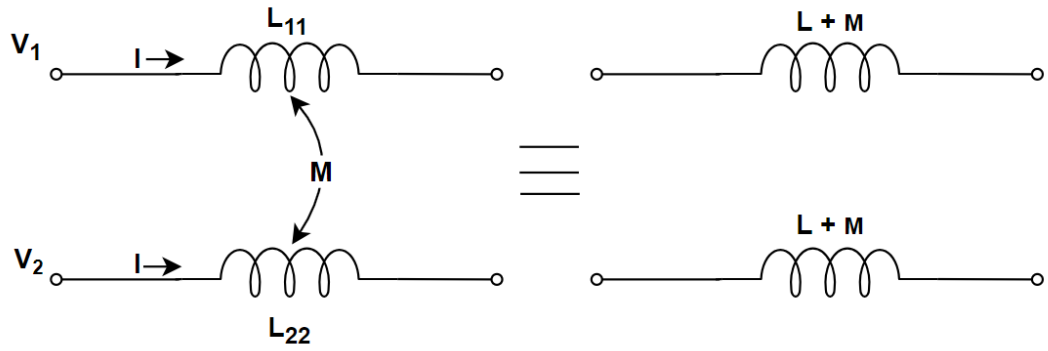



Figure 3.41: Mutual Inductance Effect

The mutual inductance between wires found using analytical formulation in Equation (3.75) are compared to ANSYS-Q3D results in the Table 3.13. Sweeping the distance between the wires, $p$, the pad distance of the identical Gaussian-shaped bondwires, $d_{\text{bp}}$, the maximum height of the wires, $L_{\text{hmax}}$ and the radius, $r_{\text{bw}}$, it is seen that the mutual inductance values that are calculated using the analytical formulation match the simulation results very well. In this context, when calculating the magnetic flux around the other wire, it is assumed that the magnetic flux occurs on the surface of the second wire, consistent with the approach taken by Q3D.

Table 3.13: Mutual Inductance of Double Wires with Different Parameters

| p (um) | $d_{bp}$ (um) | $L_{hmax}$ (um) | $r_{bw}$ (um) | Mutual Inductance (pH) | |
|---|---|---|---|---|---|
| | | | | Analytical Model | Q3D |
| **300** | 1000 | 300 | 25 | 243.74 | 243.61 |
| **300** | 1500 | 300 | 25 | 457.66 | 457.41 |
| **300** | 1500 | 600 | 25 | 489.10 | 489.65 |
| **300** | 1500 | 300 | 50 | 456.35 | 456.81 |
| **500** | 1000 | 300 | 25 | 168.95 | 168.6 |
| **500** | 1500 | 300 | 25 | 334.38 | 333.59 |
| **500** | 1500 | 600 | 25 | 350.01 | 349.45 |
| **500** | 1500 | 300 | 50 | 333.78 | 333.58 |
| **700** | 1000 | 300 | 25 | 128.71 | 128.54 |
| **700** | 1500 | 300 | 25 | 263.58 | 263.42 |
| **700** | 1500 | 600 | 25 | 272.34 | 272.48 |
| **700** | 1500 | 300 | 50 | 263.26 | 263.38 |
| **900** | 1000 | 300 | 25 | 130.59 | 103.67 |
| **900** | 1500 | 300 | 25 | 217.08 | 217.26 |
| **900** | 1500 | 600 | 25 | 222.40 | 222.45 |
| **900** | 1500 | 300 | 50 | 216.90 | 217.11 |

### 3.2.2 Interaction with Image of Wires

In the double-wire configuration, an important consideration when accounting for ground plane inductance is the inclusion of the images of the wires. Specifically, the return path in the double-wire structure involves not only the image of each wire itself but also the image of the other wire. In this case, the ground plane inductance for one of the wire is calculated as the mutual inductance between its own image, as well as the mutual inductance between the image of the other wire. This concept is illustrated in Figure 3.42.

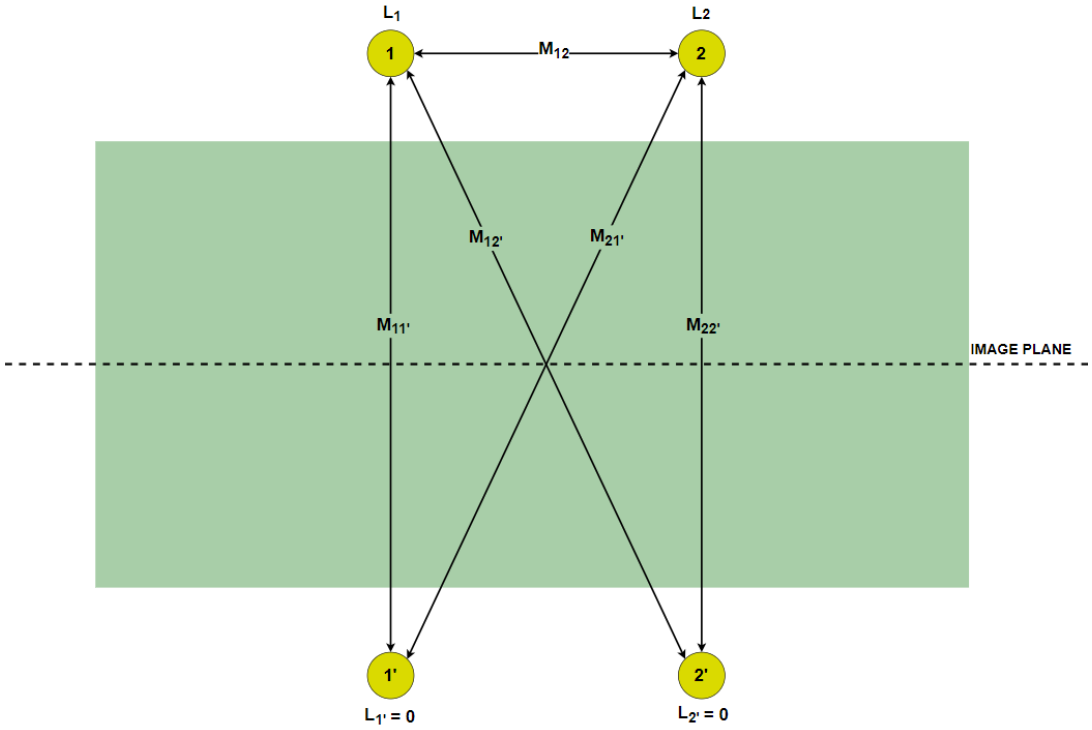



Figure 3.42: Double Wire Inductance Network

The inductance derivation between wire-1 and the image of wire-2 is very similar to the ground-plane inductance derivation given in 3.57. The formula to calculate the mutual inductance between wire-1 and image of wire-2 is given in 3.77.

$$M_{12'} = M_{21'} = \frac{\mu_0}{4\pi} \int_c \int_{c'} \frac{1 - f'(x)f'(x')}{\sqrt{(x-x')^2 + (f(x) + f(x') + 2H_{Dielectric})^2 + p^2}} dx'dx \tag{3.77}$$

$$\begin{bmatrix} L_1 & M_{12} & M_{11'} & M_{12'} \\ M_{21} & L_2 & M_{21'} & M_{22'} \\ M_{1'1} & M_{1'2} & L_{1'} & M_{1'2'} \\ M_{2'1} & M_{2'2} & M_{2'1'} & L_{2'} \end{bmatrix} = \begin{bmatrix} L_1 & M_{12} & M_{11'} & M_{12'} \\ M_{21} & L_2 & M_{21'} & M_{22'} \\ M_{11'} & M_{21'} & 0 & 0 \\ M_{12'} & M_{22'} & 0 & 0 \end{bmatrix} \tag{3.78}$$

$$M_{total} = M_{11'} + M_{12'} \tag{3.79}$$

Due to the symmetry of the matrix, the $M_{ij}$ terms are symmetric and equal to each other. Furthermore, the self-inductances of the return path, denoted as $L_1'$ and $L_2'$, are assumed to be zero. This assumption is based on the consideration that the PCB ground plane is treated as an infinitely large surface. Both of these conditions are reflected in the matrix equation above. The mutual inductance between wire-1 and the ground is expressed by equation 3.79.

### 3.2.3 Comparison Of The Models with HFSS Simulation Results for Double Wire Configuration

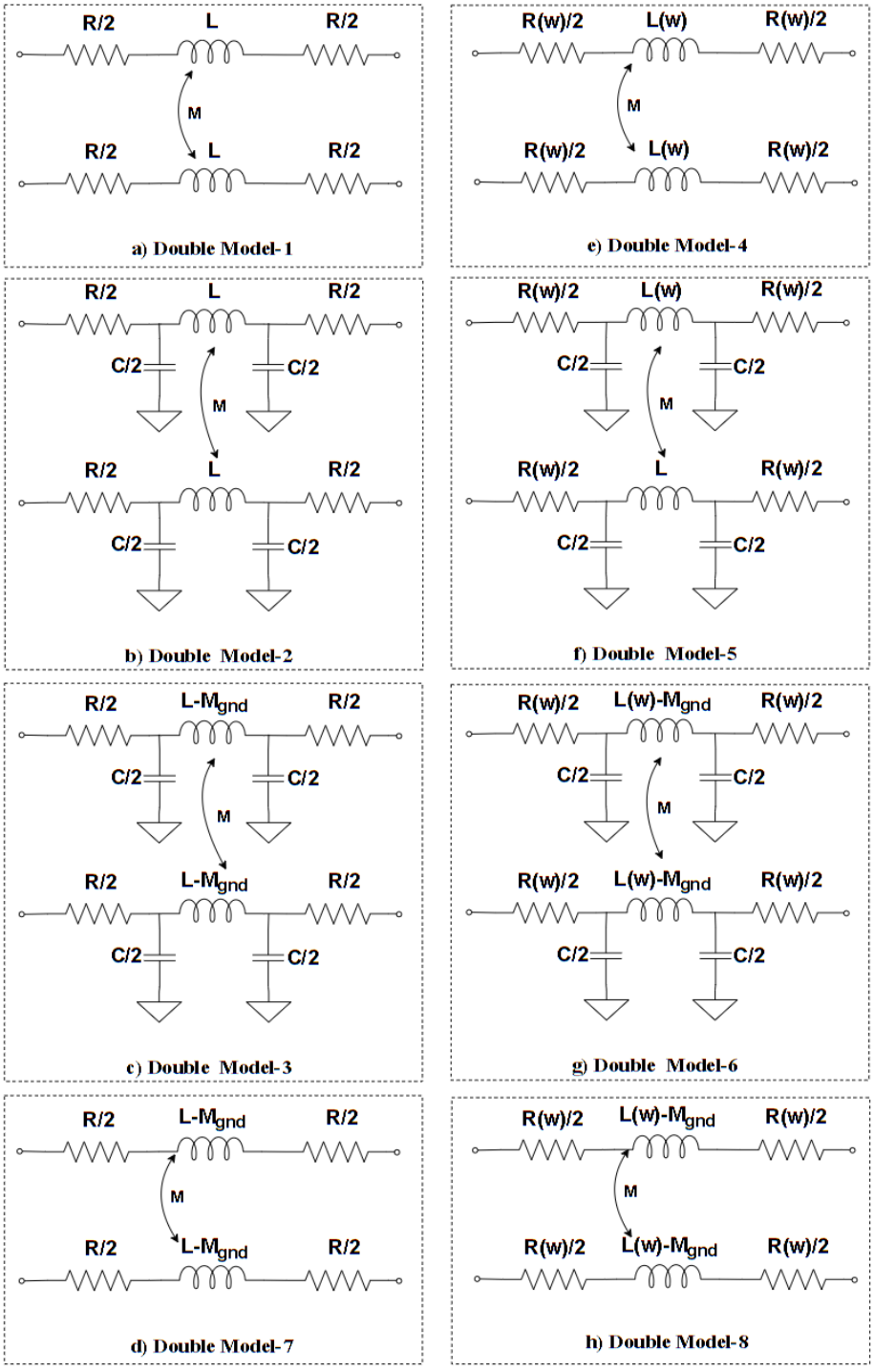



Figure 3.43: Double Wires Lumped Element Models

8 lumped element models are used to analyze the behavior of a double bond wires, as illustrated in Figure 3.43. These models are developed analytically and compared with HFSS simulation results. The first model, shown in Figure 3.43(a), considers only DC inductance, $L$, DC resistance, $R$, and mutual inductance between double wires, $M$. The second model, Figure 3.43(b), incorporates capacitance to the ground plane, $C$. The third model, Figure 3.43(c), additionally includes the mutual inductance effect of the ground plane,$M_{\text{gnd}}$, focusing on DC effects. To enhance accuracy, a frequency-dependent inductance,$L(w)$ and resistance, $R(w)$ model is introduced as model-4, Figure 3.43(e). Subsequently, model-5, Figure 3.43(f), and model-6, Figure 3.43(g), integrate both capacitance and mutual inductance effects of the ground plane. Model-7 represents a DC value model in which the ground plane effect is included only as return path inductance without considering the capacitance, Figure 3.43(d). In contrast, Model-8 extends this approach to a frequency-dependent version in which frequency effects are included in the model as $L(w)$ and $R(w)$, Figure 3.43(h).

For a double bondwire case with $d_{bp} = 1500, \mu m$, $L_{hmax} = 200, \mu m$, $r_{bw} = 6.25, \mu m$ and $p = 100, \mu m$ simulations are conducted across a frequency range of 0.05 GHz to 20 GHz. In Figure 3.44, Capacitance-free models (Model-1, Model-4, Model-7, and Model-8) show significant deviations from Q3D and HFSS results for this longer wire case. Models excluding the ground plane mutual inductance effect (Model-2 and Model-5) overestimate inductance values. In contrast, models incorporating both capacitance and ground plane inductance (Model-3 and Model-6) provide the most accurate predictions. the key point in the double wire model is that the wire interacts not only with its own image but also with the image of the other wire, and when this interaction is taken into account, the models become more accurate.

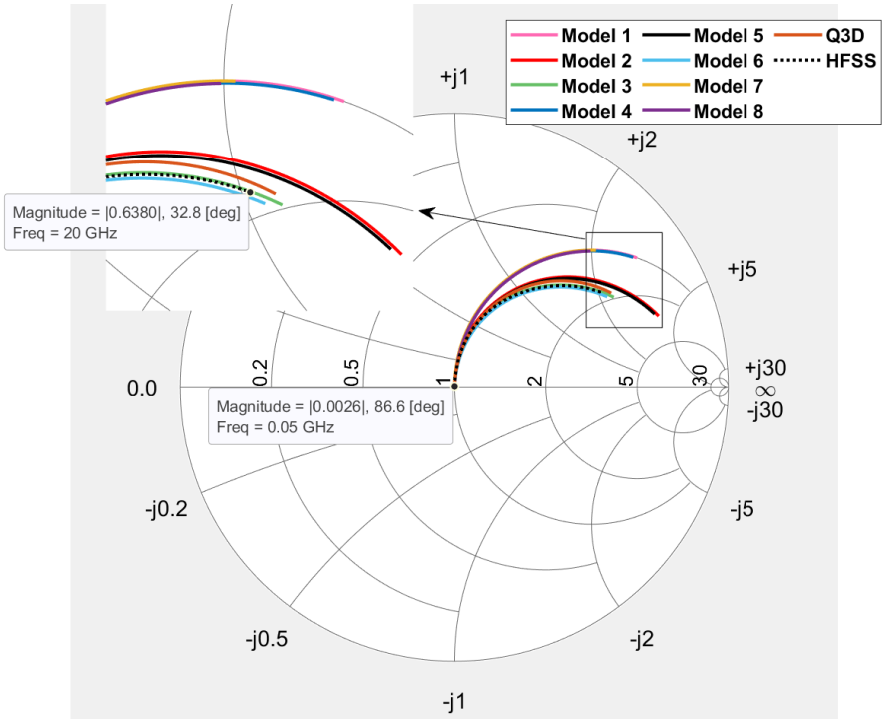



Figure 3.44: Double Wire-Comparison of $S_{11}$ on Smith Chart for $d_{bp} = 1500\,\mu m$

In the case of a double wire with shorter length with $d_{bp} = 750, \mu m$, $L_{hmax} = 200, \mu m$, $r_{bw} = 6.25, \mu m$ and $p = 100, \mu m$ , similar trends are observed in Figure 3.45. Model-3 and Model-6 show results much closer to Q3D and HFSS. While Models-2 and Model-5 consider only self-inductance and deviate more from the expected results, they neglect ground-plane mutual inductance. Research shows that including ground-plane inductance reduces the total inductance, and when added to Models-2 and Model-5, more accurate results are obtained, leading to the creation of Model-3 and Model-6.

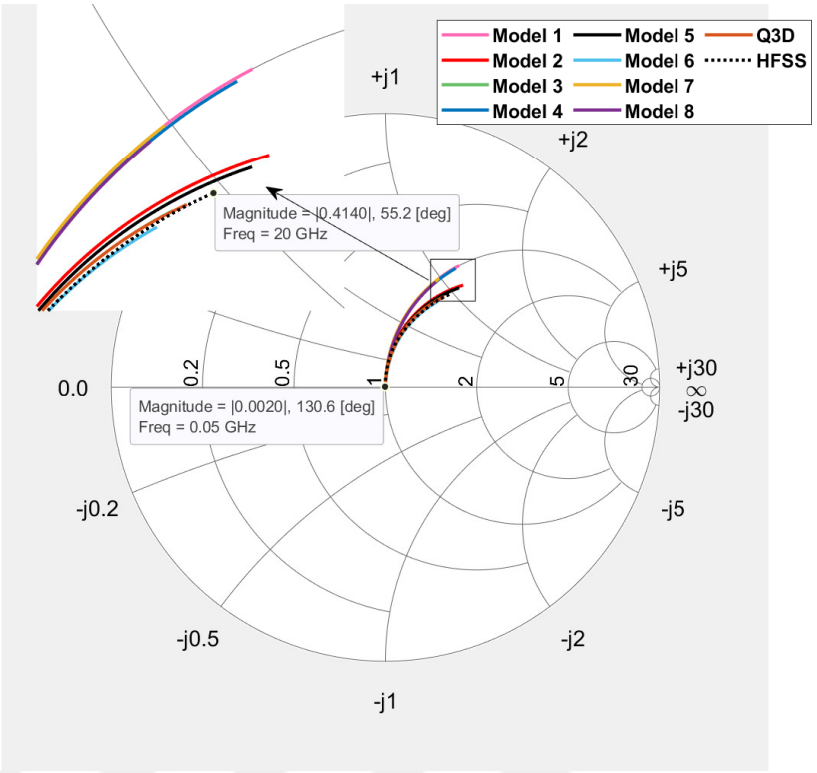



Figure 3.45: Double Wire-Comparison of $S_{11}$ on Smith Chart for $d_{bp} = 750\,\mu m$

In order to understand the behavior of the lumped element models with respect to the geometric parameters and frequency, a detailed analysis is done below. In Figure 3.46 and Figure 3.47, NMSE of complex S parameters of the models with respect to HFSS results are plotted. NMSE error formulas are given in the single wire section, from equation 3.59 to equation 3.64. The same formulas are valid for the double wire case. For a constant $d_{\text{bp}}$ value, along frequency band, deviation from HFSS results is shown. As in the single wire case, Model-3 and Model-6 gives the better result with HFSS and Q3D, while other models give closer approximation at some specific cases. For example, at lower $d_{\text{bp}}$ values, Model-2 and Model-5 estimates closer inductance values to HFSS since ground plane inductance is not subtracted. For Model-3 and Model-6, there can be a numeric error while calculating return path inductance- ground plane mutual inductance.

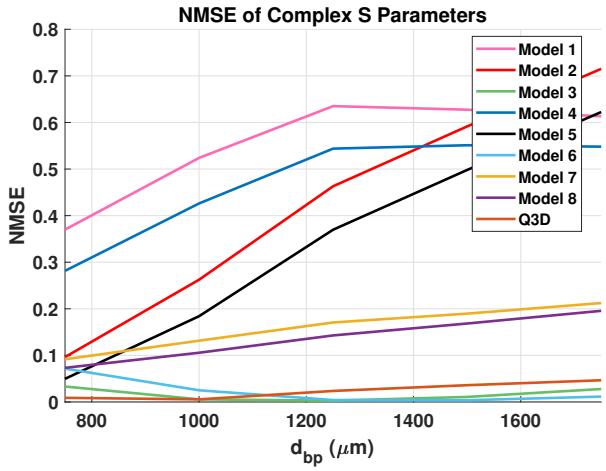



Figure 3.46: Double Wire - NMSE of Complex $S_{11}$ along Frequency Band for Different $d_{\text{bp}}$ Values - $d_{bp}$ Sweep, $L_{hmax} = 200\,\mu m$, $p = 100\,\mu m$, (NMSE is calculated over 0.05-20 GHz)

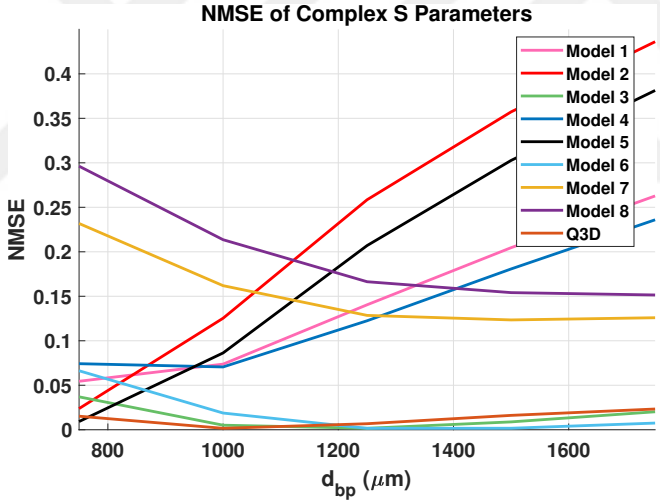



Figure 3.47: Double Wire - NMSE of Complex $S_{21}$ along Frequency Band for Different $d_{\text{bp}}$ Values - $d_{bp}$ Sweep, $L_{hmax} = 200\,\mu m$, $p = 100\,\mu m$, (NMSE is calculated over 0.05-20 GHz)

In Figure 3.48 and Figure 3.49, deviation of the models from HFSS is shown at a constant frequency with different $d_{\text{bp}}$ values. As in the single wire case, deviation of the Model-7 and Model-8 shows that at higher frequencies capacitance is needed to be

included to get more accurate results as Model-3 and Model-6. Because of numerical error around 6 GHz, a slight deviation is observed in comparison for frequency sweep.

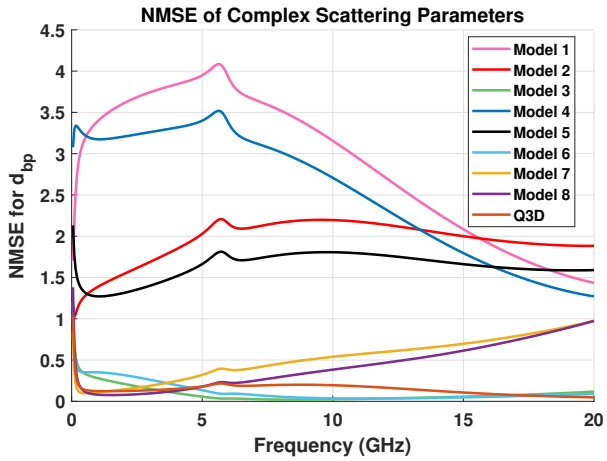



Figure 3.48: Double Wire - NMSE of Complex $S_{11}$ calculated from $d_{\text{bp}}$ sweep at A Frequency. - Frequency Sweep, $L_{hmax} = 200\,\mu m$, $p = 100\,\mu m$, (NMSE is calculated over $d_{bp} = 750 - 1500\,\mu m$)

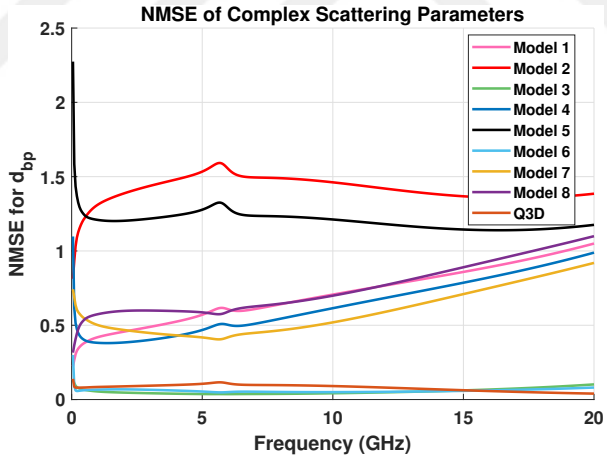



Figure 3.49: Double Wire - NMSE of Complex $S_{21}$ calculated from $d_{\text{bp}}$ sweep at A Frequency. - Frequency Sweep, $L_{hmax} = 200\,\mu m$, $p = 100\,\mu m$, (NMSE is calculated over $d_{bp} = 750 - 1500\,\mu m$)

In Figure 3.50 and Figure 3.51, NMSE of complex S parameters of the models with respect to HFSS results are plotted. For a constant $L_{\text{hmax}}$ value, along frequency

band, deviation from HFSS results is shown. As in the single wire case, Model-3 and Model-6 gives the better result with HFSS and Q3D.

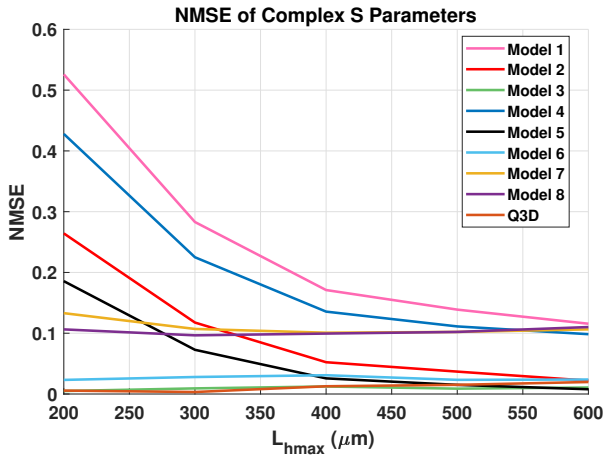



Figure 3.50: Double Wire - NMSE of Complex $S_{11}$ along Frequency Band for Different $L_{\text{hmax}}$ Values- $L_{hmax}$ Sweep, $d_{bp} = 1000\,\mu m$, $p = 100\,\mu m$, (NMSE is calculated over 0.05-20 GHz)

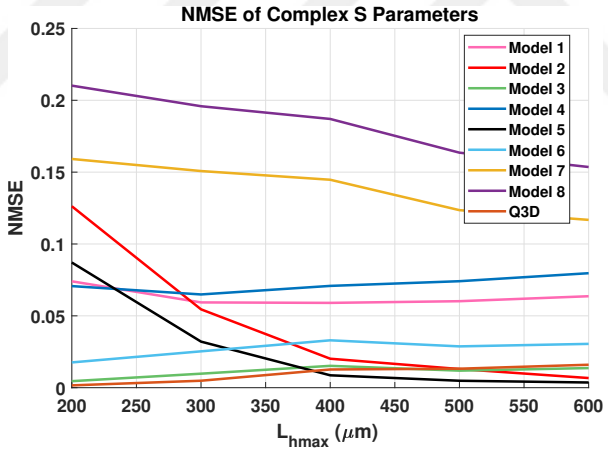



Figure 3.51: Double Wire - NMSE of Complex $S_{21}$ along Frequency Band for Different $L_{\text{hmax}}$ Values- $L_{hmax}$ Sweep, $d_{bp} = 1000\,\mu m$, $p = 100\,\mu m$, (NMSE is calculated over 0.05-20 GHz)

In Figure 3.52 and Figure 3.53, NMSE of the complex S parameters of the models with respect to HFSS results are plotted. For a constant frequency value, along $L_{\text{hmax}}$ sweep, deviation from HFSS results is shown. Model-3 and Model-6 give the best

match with HFSS results. Also, the results of their capacitance free version Model-7 and Model-8 show that capacitance is a key component for high frequencies to get accurate results. In addition there is an larger error with respect to other frequencies at the begining of the frequency band for Model-3 and Model-6. Such an error occurs because deviation of the HFSS results from its mean is more than other frequencies.

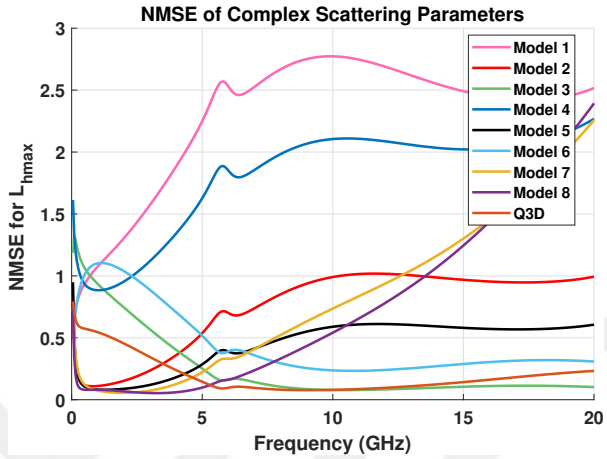



Figure 3.52: Double Wire - NMSE of Complex $S_{11}$ calculated from $L_{\text{hmax}}$ sweep at A Frequency. - Frequency Sweep, $d_{bp} = 1000\,\mu m$, $p = 100\,\mu m$, (NMSE is calculated over $L_{hmax} = 200 - 600\,\mu m$)

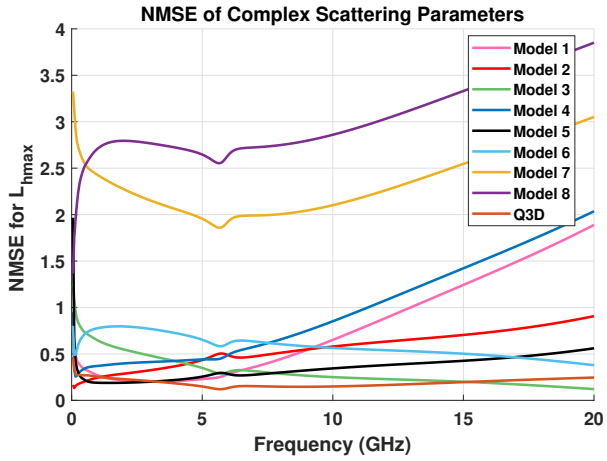



Figure 3.53: Double Wire - NMSE of Complex $S_{21}$ calculated from $L_{\text{hmax}}$ sweep at A Frequency. - Frequency Sweep, $d_{bp} = 1000\,\mu m$, $p = 100\,\mu m$, (NMSE is calculated over $L_{hmax} = 200 - 600\,\mu m$)

In Figure 3.54 and Figure 3.55, NMSE of complex S parameters of the models with respect to HFSS results are plotted. For a constant $p$ value, along frequency band, deviation from HFSS results is shown. Accuracy of Model-3 and Model-6 is better than other models.

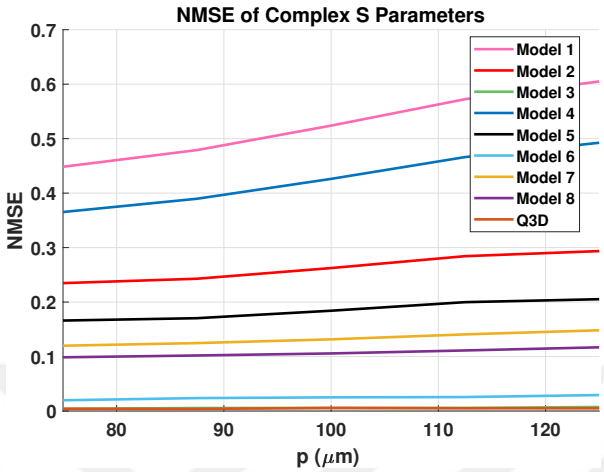



Figure 3.54: Double Wire - NMSE of Complex $S_{11}$ along Frequency Band for Different $p$ Values - $p$ Sweep, $d_{bp} = 1000\,\mu m$, $L_{hmax} = 200\,\mu m$, (NMSE is calculated over 0.05-20 GHz)

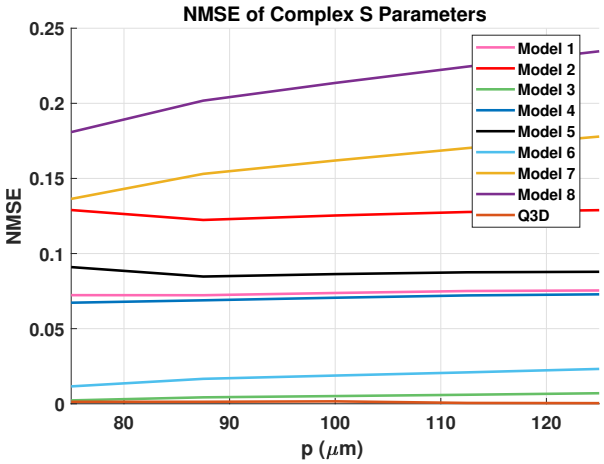



Figure 3.55: Double Wire - NMSE of Complex $S_{21}$ along Frequency Band for Different $p$ Values - $p$ Sweep, $d_{bp} = 1000\,\mu m$, $L_{hmax} = 200\,\mu m$, (NMSE is calculated over 0.05-20 GHz)

In Figure 3.56 and Figure 3.57, NMSE of complex S parameters of the models with respect to HFSS results are plotted. For a constant frequency value, along $p$, deviation from HFSS results is shown. In S parameters, real and imaginary parts are estimated in Model-3 and Model-6 more accurately. Again it is observed that when capacitance is removed from Model-3 and Model-6, the lumped element models Model-7 and Model-8 are created respectively. Their results deviate at higher frequencies due to lack of capacitance. In frequency sweep, around 2 GHz, NMSE value is measured larger than other frequencies for Model-3 and Model-6. The reason for this is that the HFSS data is not far from its own mean. In other words, the denominator in the NMSE formula is very small at this frequency. The Smith chart plot shown in Figure 3.58. It is comparing the means of the HFSS data at five different $p$ values. This figure shows that around 2 GHz, the deviation from the mean is minimal. In Figure 3.59,a comparison is made between the HFSS data and the results from Model 6 for a single value. Upon examining this comparison, it becomes evident that even though the difference is small, the NMSE value at around 2 GHz is slightly higher. This is due to the very small denominator in the NMSE formula, which magnifies the effect of even a small difference.

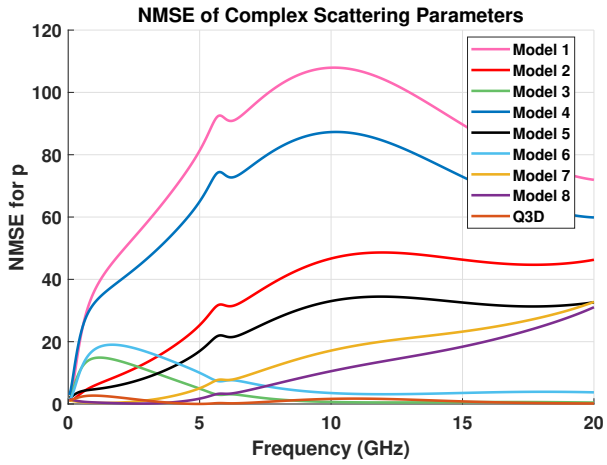



Figure 3.56: Double Wire - NMSE of Complex $S_{11}$ calculated from $p$ sweep at A Frequency. - Frequency Sweep, $d_{bp} = 1000\,\mu m$, $L_{hmax} = 200\,\mu m$, (NMSE is calculated over $p = 200 - 600\,\mu m$)

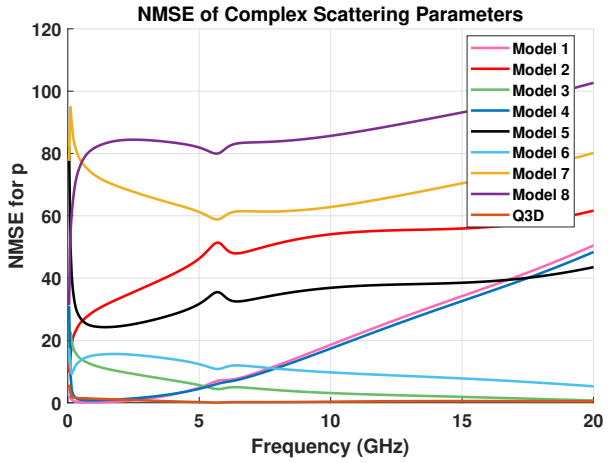



Figure 3.57: Double Wire - NMSE of Complex $S_{21}$ calculated from $p$ sweep at A Frequency. - Frequency Sweep, $d_{bp} = 1000\,\mu m$, $L_{hmax} = 200\,\mu m$, (NMSE is calculated over $p = 200 - 600\,\mu m$)

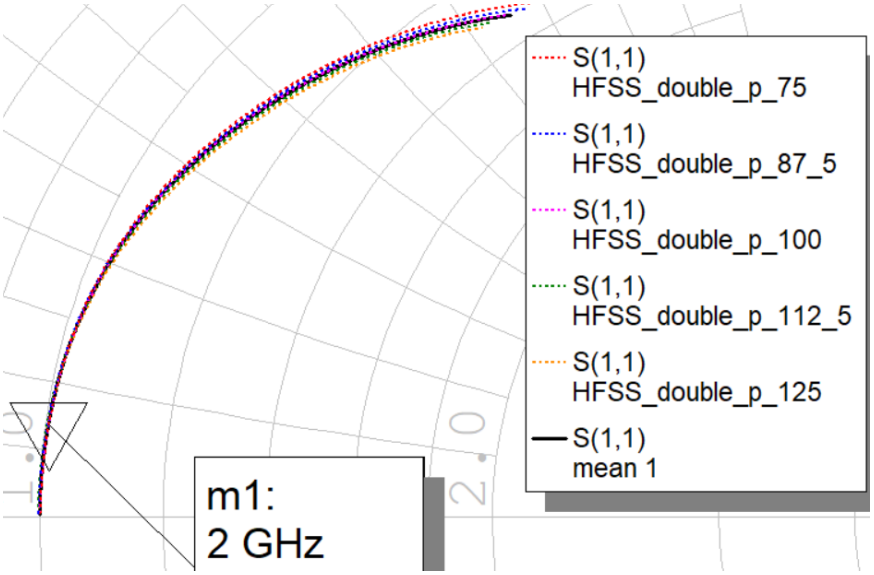



Figure 3.58: Comparison of 5 different s2p file for $p$ and Their Mean.

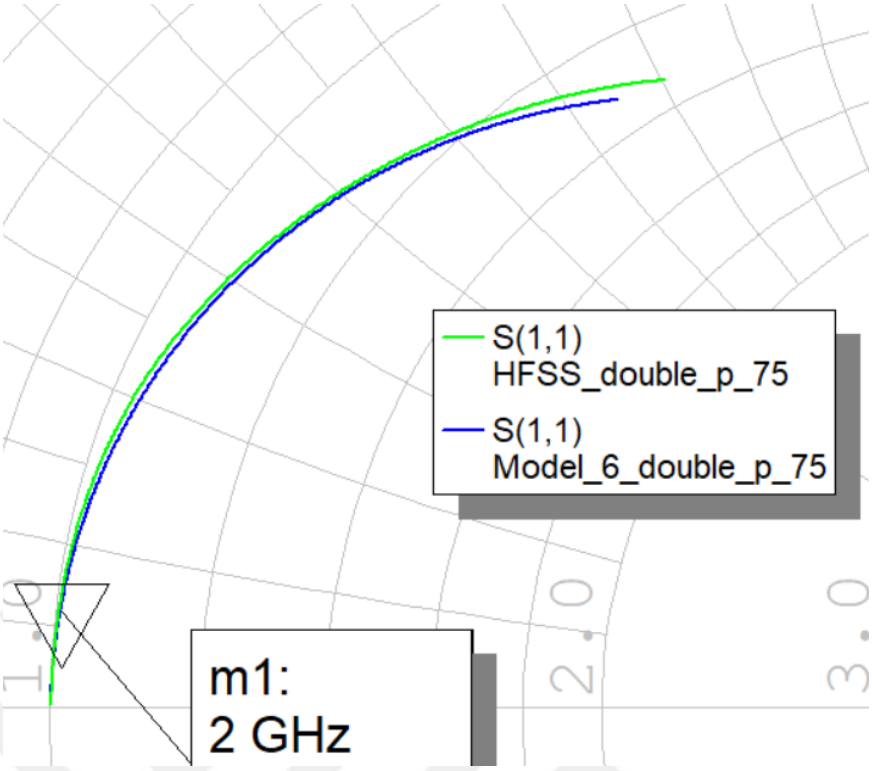



Figure 3.59: Comparison of HFSS data and Model-6 Data for $p = 75\mu m$

To conclude this section; in double-wire analyses, the frequency is varied with fixed parameters, and the parameters are swept with a constant frequency. All of the results are consistent with the single wire case. The most comparable outcomes to Q3D and HFSS are produced by Model-3 and Model-6 due to their consideration of ground-plane mutual inductance and capacitance. Satisfactory results are achieved by Model-7 and Model-8 for short wire lengths; however, an increased margin of error is observed at high frequencies and with long wires as a result of the absence of capacitance. In contrast, Model-2 and Model-5, which account for capacitance but not ground-plane inductance, demonstrate superior performance with shorter wire lengths. Nonetheless, significant deviations observed at high frequencies and with long wire lengths render these models unreliable.

As mentioned in the single wire case, lumped element models are analytical static solvers and Q3D is quaistatic solver. Therefore, it is also needed to compare the lumped element models with Q3D in terms of NMSE. In Figure 3.60, Figure 3.61

and Figure 3.62, Model-3 and Model-6 gives the best match with Q3D. When the length of the wire increases, accuracy of Model-6 increases.

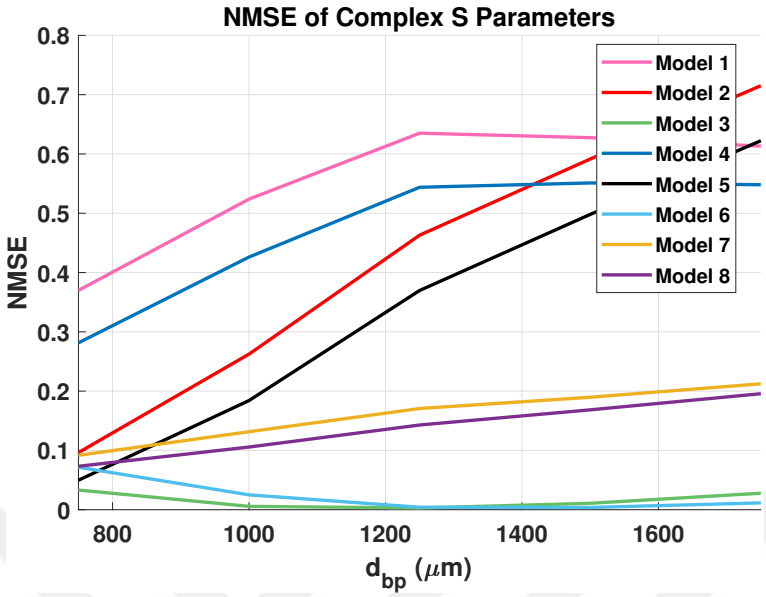



Figure 3.60: Double Wire - NMSE of Complex $S_{11}$ with respect to Q3D for $d_{\text{bp}}$. - $d_{bp}$ Sweep, $L_{hmax} = 200\,\mu m$, $p = 100\,\mu m$, (NMSE is calculated over 0.05-20 GHz)

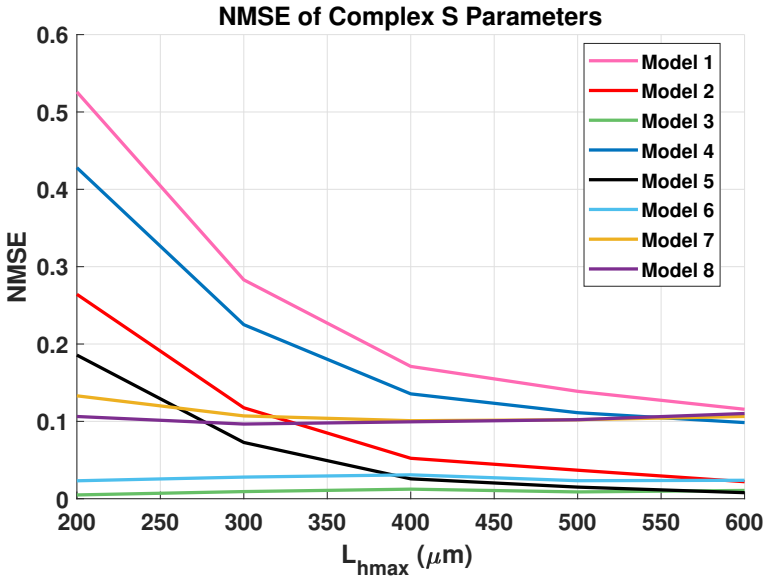



Figure 3.61: Double Wire - NMSE of Complex $S_{11}$ with respect to Q3D for $L_{\text{hmax}}$. - $L_{hmax}$ Sweep, $d_{bp} = 1000\,\mu m$, $p = 100\,\mu m$, (NMSE is calculated over 0.05-20 GHz)

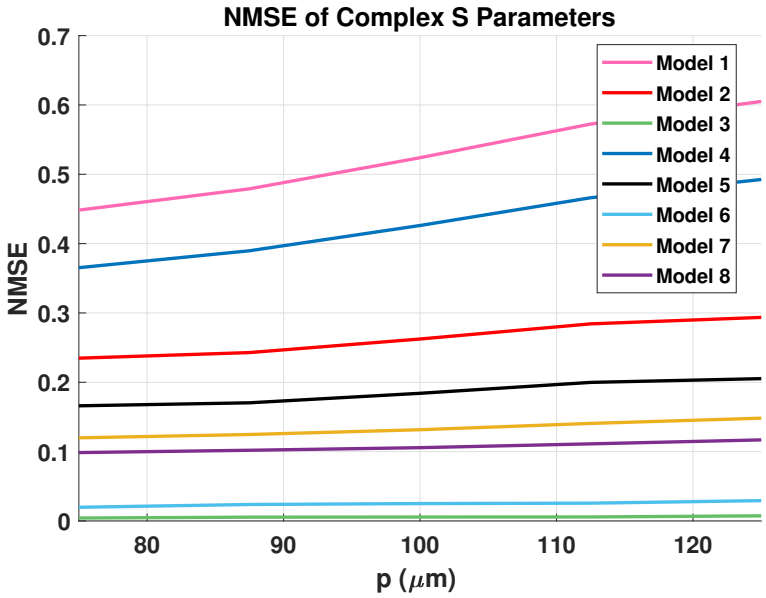



Figure 3.62: Double Wire - NMSE of Complex $S_{11}$ with respect to Q3D for $p$. - $p$ Sweep, $d_{bp} = 1000\,\mu m$, $L_{hmax} = 200\,\mu m$, (NMSE is calculated over 0.05-20 GHz)

# CHAPTER 4

# APPLICATION: POWER AMPLIFIERS

As stated in Chapter 1, 2, and Figure 2.5 2.6, the performance characteristics of power amplifiers are compromised by wire bond structures due to their high impedance impact. This deterioration may be shown using an MMIC power amplifier that consists of a die transistor and input-output matching networks on a GaN or GaAs substrate. In this chapter, degradation of performance of a MMIC power amplifier is shown using 4 different wire bond configuration. Different wirebond results are compared to 50 $\Omega$ output pad performance.

## 4.1 Wirebond Usage on MMIC

MMIC PAs are compact power amplifiers designed to provide high power inside a limited space [45]. To attain reduced dimensions and compactness, they are fabricated on substrates with high dielectric constants, such as GaN, SiC, and GaAs [46]. Nonetheless, these substrates are unsuitable for usage as PCBs due to the complexity and expense of the processes involved. Consequently, after fabricating an MMIC PA using GaN, GaAs, or SiC, it is essential to establish a connection with the PCB substrate containing additional RF materials or circuits, such as alumina, or RO4003, or FR-4. The connection is established by wirebonds, leading to parasitic effects. The procedure is shown in Figure 4.1. A 50-ohm-matched MMIC power amplifier is mounted to a metal layer and is attached to the printed circuit board, which resides on the same metal plate.

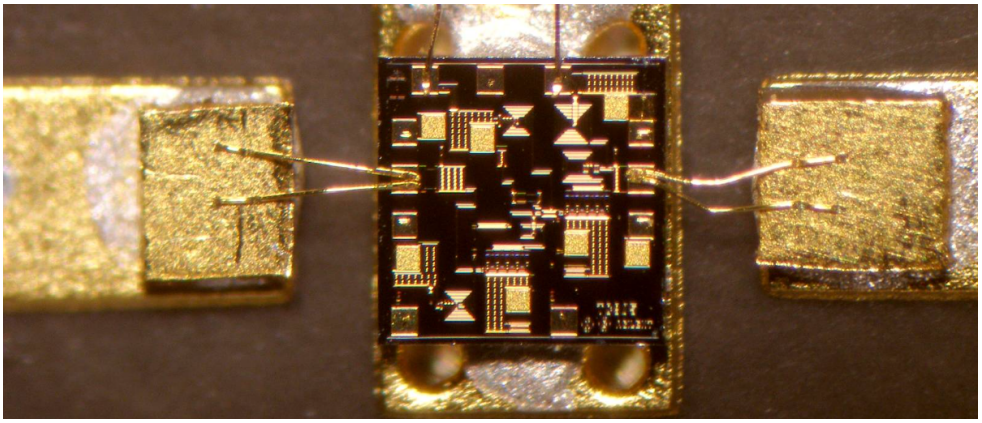


Figure 4.1: Bonding Process of MMIC PA [47]

## 4.2 Comparison of The Lumped Element Models with HFSS Results

To compare analytical and EM simulation results, a GaN substrate-based MMIC power amplifier operating in the 8-11 GHz range with a 20 W output power is used. First, the output power, gain, and efficiency values of the power amplifier are examined when it presents a 50-ohm output match. Then, the performance changes are observed as the output is connected to an alumina PCB through two different double-wire and two different single-wire configurations. During this process, the nonlinear MMIC PA model is cascaded with analytical and EM simulation wirebond results in the form of s2p files, and the results are compared using ADS, a widely used application in fields such as RF/microwave circuit design, antenna design, power amplifiers, filters, and signal integrity analysis. It is determined in 3 that either Model-3 or Model-6 from Figure 3.20 can be used as the analytical model, and comparisons are made using Model-6, Figure 3.20 (g) .

### 4.2.1 Single Wire Cases

In the single bondwire cases, 2 different length of bondwires, 0.5 mm and 0.8 mm are cascaded in MMIC nonlinear model in ADS as, which is described in Figure 4.2.

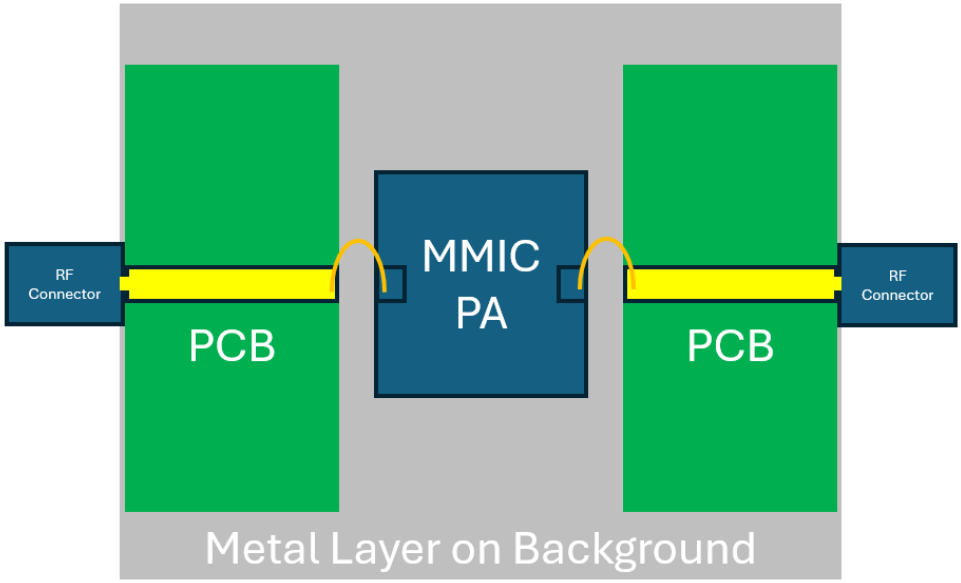



Figure 4.2: Cascaded Simulation with Single Wire in ADS

In the single-wire case, the inductance of the single wire is not reduced by being in parallel with any other wire, resulting in a much higher inductance value. Consequently, the impedance of the transmission line becomes much higher than 50 ohms. As a result, mismatch loss occurs, leading to a decrease in output power, gain, and power added efficiency values.As a result of this mismatch, as seen in the output power, Figure 4.3, gain, Figure 4.4, and Power Added Efficiency (PAE), Figure 4.5, the wirebond structure has caused degradation in these parameters. The PA, which can deliver 43 dBm of power with a 50-ohm load, has reduced its output power when using the single wire. It is notable that the analytical model and HFSS results have predicted very close outcomes. These results are consistent for two different single-wire lengths as well. The same trend is observed in the gain graph, Figure 4.4 where a decrease in gain occurs, and this reduction has been accurately predicted by the analytical model. In Figure 4.5, the trend in the PAE graph has also been predicted accurately at a good level for both cases.

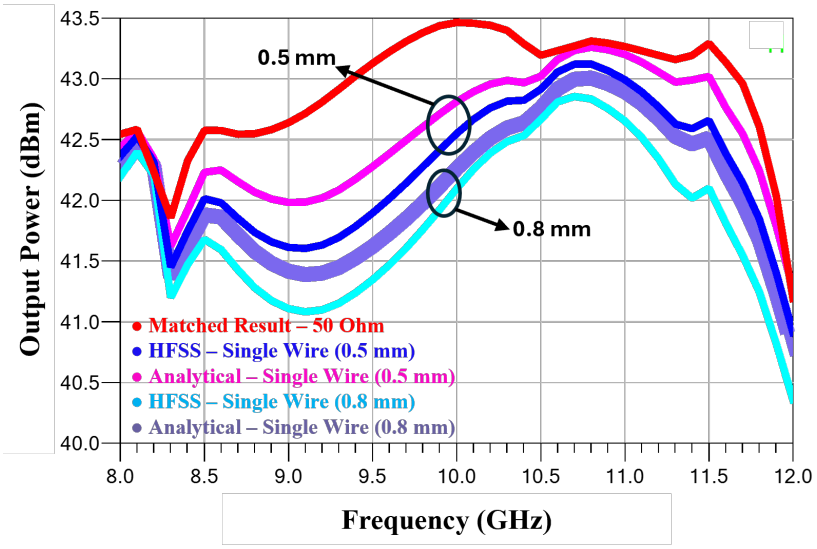



Figure 4.3: Comparison of Analytical Model and HFSS in terms of Output Power-Single Wire

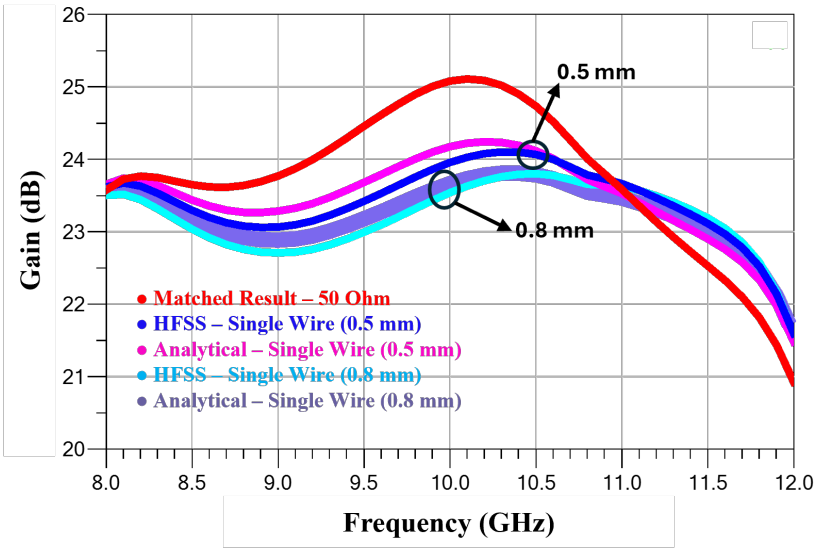



Figure 4.4: Comparison of Analytical Model and HFSS in terms of Gain-Single Wire

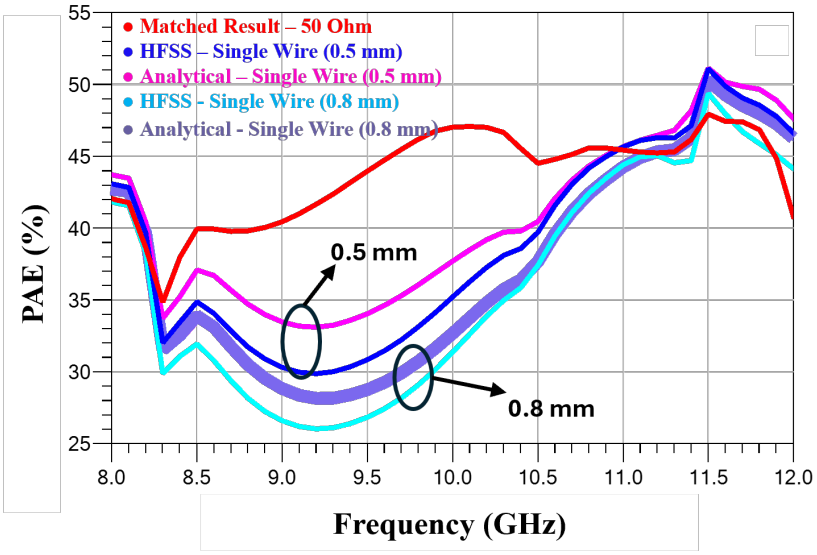



Figure 4.5: Comparison of Analytical Model and HFSS in terms of PAE-Single Wire

Additionally, note that using the longer wire will result in a more significant degradation due to the higher inductance value, which leads to much higher characteristic impedance than 50 ohm. This behavior is shown in the figures above for the single wire case.

### 4.2.2 Double Wire Cases

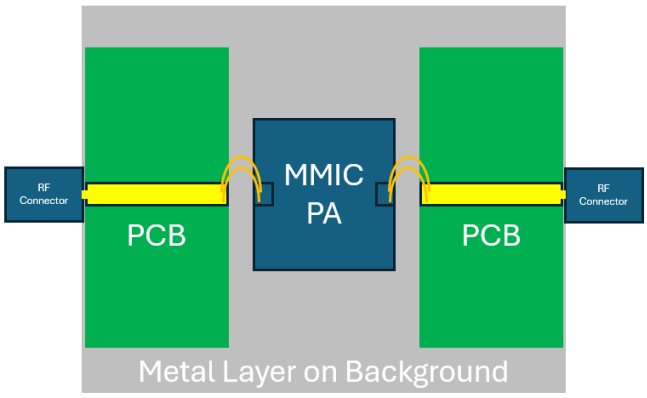



Figure 4.6: Cascaded Simulation with Double Wire in ADS

In the double-wire case, the paralleling of two wires reduces the inductance of the system, resulting in a slightly higher inductance value compared to a single wire. Consequently, the impedance of the transmission line is closer to 50 ohm than a single-wire case. This leads to a reduction in mismatch loss, although it remains insufficient. Therefore, a decrease in output power, gain, and power-added efficiency values also occurs in the double-wire case. The decrease in these parameters is not as high as that in a single-wire case. As seen in the output power, Figure 4.7, gain, Figure 4.8, and Power Added Efficiency (PAE), Figure 4.9, the wirebond structure has caused degradation in these parameters. The PA, which can deliver 43 dBm of power with a 50-ohm load, has reduced its output power when using the double wire. It is notable that the analytical model and HFSS results have predicted very close outcomes. The mathematical model and HFSS results have yielded very similar results. These findings are consistent across two distinct single-wire lengths. A similar tendency is seen in the gain graph, Figure 4.8 where a decrease in gain occurs, and this reduction has been accurately predicted by the analytical model for double wire. In Figure 4.9, the trend in the PAE graph has also been predicted enough accurate for both cases.

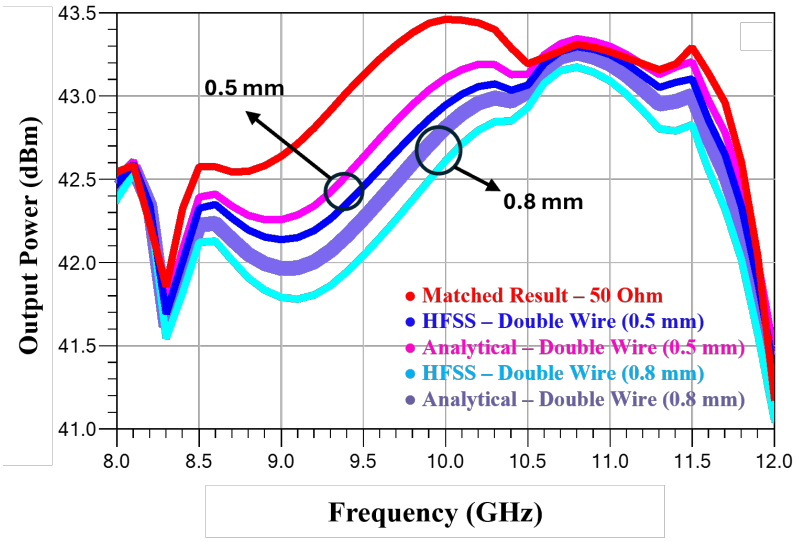



Figure 4.7: Comparison of Analytical Model and HFSS in terms of Output Power-Double Wire

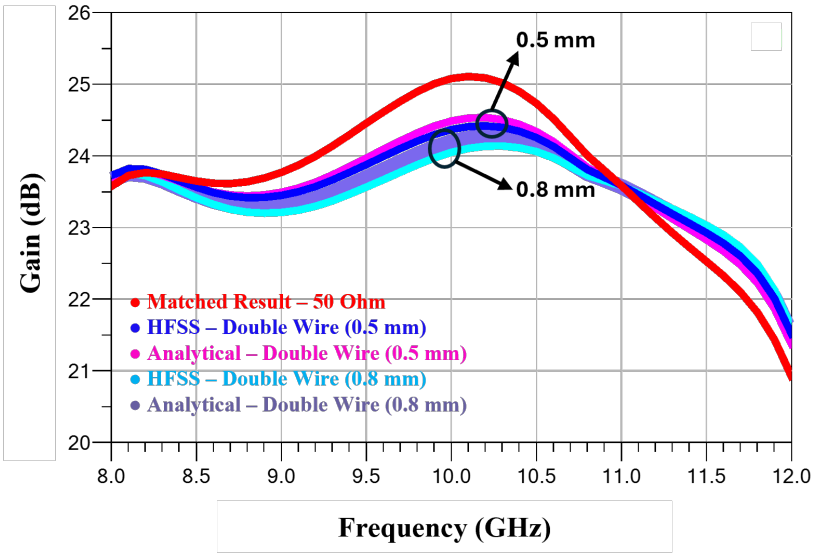



Figure 4.8: Comparison of Analytical Model and HFSS in terms of Gain-Double Wire

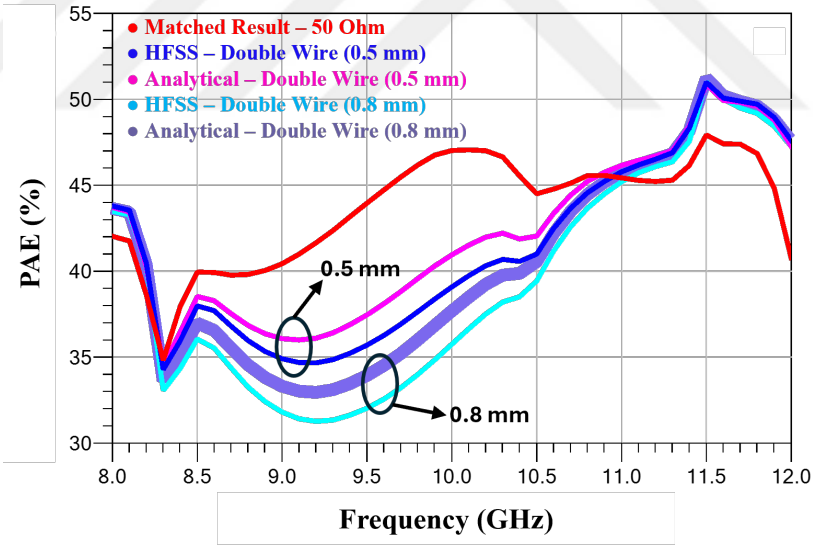



Figure 4.9: Comparison of Analytical Model and HFSS in terms of PAE-Double Wire

Additionally, note that using the longer wire is lead to a more significant degradation due to the higher inductance value, which leads to much higher characteristic

impedance than 50 ohm. This behavior is shown in the figures above for the double wire case.

Despite everything, an improvement is observed in the double-wire structure compared to the single-wire structure. For 0.5 mm single wire, output power is measured 42 dBm at 9 GHz, Figure 4.3, while it is 42.5 dBm for the same length-double wire, Figure 4.7. Also, in gain graphic of single wire indicates that Gain is 24.2 dB at 10 GHz,Figure 4.4, while it is 24.5 dB for double wire case, Figure 4.8. This improvement is attributed to the parallel inductance reducing the total inductance. Power added efficiency is also improved in double wire cases.

# CHAPTER 5

# CONCLUSION

In power amplifier (PA) circuits, bondwires are often used to connect the die substrate to an external PCB or as part of the die's packaging. However, because to their highly thin nature, bondwires contribute considerable parasitic effects like as inductance, resistance, and capacitance, which have an adverse effect on die performance. Furthermore, they cause mismatch concerns, which reduces overall efficiency. These parasitic effects may be investigated using full-wave electromagnetic simulations using tools such as HFSS or CST, as well as quasi-static simulations with Q3D. However, these methods are computationally demanding, requiring long solution durations and high-performance hardware such as sophisticated RAM and GPU setups, making such studies costly.

An alternate technique is to characterize bondwires as lumped components, with a series resistance, a series inductance, and a capacitance to ground. To overcome the high computational cost and lengthy simulation durations associated with EM tools, this work focuses on modeling bondwires using lumped element models rather than EM simulations. Eight unique models are created, and their S-parameters and lumped element values are compared to the HFSS and Q3D results. These parameters are analytically defined, numerically solved in MATLAB, and then integrated into circuit simulations in AWR.

The models account for DC resistance and inductance, frequency-dependent resistance and inductance, mutual inductance to the ground plane, mutual inductance between wires, and capacitance. Analyses are performed for both single-wire and double-wire setups, with factors such as the distance between bondwire pads, bondwire height, and radius swept throughout a frequency range of DC-20 GHz. Smith

charts are used to compare results for $S_{11}$ and $S_{21}$. Normalized mean square error (NMSE) values are used to quantify deviations from HFSS results.

Models 3 and 6, which account for ground mutual inductance and capacitance, show the best agreement with HFSS and Q3D findings in the single-wire situation. Model-6 adds frequency-dependent resistance and inductance, as well as ground mutual inductance and capacitance, to provide enhanced system behavior prediction. Model-7 and Model-8, which utilize mutual inductance instead of capacitance, work well in cases with minor capacitance effects, such as shorter bond lengths (e.g., $d_{\text{bp}}$ = 500 $\mu m$ and $d_{\text{bp}}$) =750 $\mu m$. However, when the bondwire length increases, the differences in these models and HFSS become increasingly noticeable. Furthermore, capacitor-free models deviated more beyond 10 GHz owing to impedance changes produced by capacitance effects. Capacitance-inclusive models, such as Model-3 and Model-6, stay stable over the frequency range, highlighting the need of include capacitance at higher frequencies, after 10 GHz.

In the double-wire design, both Model-3 and Model-6 take into consideration the effects of mutual inductance and capacitance, as well as interactions with the other wire and image of the other wire as ground plane effect. These models also correlate well with the findings of the HFSS and Q3D, indicating their suitability for assessing wirebond architectures. Similar to the single-wire situation, shorter bonds that eliminate capacitance but account for ground inductance, such as Model-7 and Model-8, provide satisfactory results.

Validated model, namely Model-6, is used in a real-world situation involving a GaN-based MMIC PA operating in the 8-11 GHz range with a 20 W output power. The PA connects to an alumina PCB using wirebonds modeled with Model-6 in simulation. Four cases — two single-wire configurations of varying lengths and two double-wire configurations that match the single-wire lengths — are investigated. These wirebond structures are cascaded with the nonlinear MMIC PA model in ADS, and their impacts on output power, gain, and power-added efficiency (PAE) are compared to the PA's performance at 50 ohms in simulation.

All four instances degrade the MMIC PA's performance. However, shorter single-wire systems degrade less than longer ones. There are benefits to double-wire ar-

rangements compared to single-wire constructions of the same length. This improvement is due to the parallel connection of the bondwire inductances, which decreases overall inductance and brings the double-wire line's characteristic impedance closer to 50 ohms. At approximately 11 GHz, the single-wire configuration exhibits superior performance. This may be attributed to the output impedance of the MMIC PA not being exactly 50 ohms, with the single-wire structure providing better impedance matching compared to the double-wire configuration. In all situations, Model-6 produces findings that are consistent with HFSS, properly characterizing the severity of the performance decline. In conclusion, Model-3 and Model-6 emerge as the most robust and accurate analytical models for bondwire analysis, demonstrating exceptional reliability across different configurations and frequencies. Its ability to account for frequency-dependent effects, mutual inductance, and capacitance makes it superior to other models, ensuring precise predictions with minimal computational cost. Thus, this approach provides a faster and more cost-effective method for bondwire modeling compared to traditional full-wave simulations.

## REFERENCES


[1] A. Grebennikov, *RF and Microwave Power Amplifier Design*. McGraw-Hill Education, 2004.

[2] A. Shirvani and B. Wooley, *Design and Control of RF Power Amplifiers*. Springer US, 2013.

[3] X. Li, H. Fu, K. MA, S. Zhu, and Q. Cheng, "Rf/microwave power amplifiers: The development route and state-of-the-art," *Journal of Circuits, Systems and Computers*, vol. 29, p. 2030004, 03 2020.

[4] W. Greig, *Integrated Circuit Packaging, Assembly and Interconnections*. Springer Series in Advanced Microelectronics S., v. 25, Springer US, 2007.

[5] G. Baumann, D. Ferling, and H. Richter, "Comparison of flip chip and wire bond interconnections and the technology evaluation on 51 ghz transceiver modules," in *1996 26th European Microwave Conference*, vol. 1, pp. 98–100, 1996.

[6] C. A. Palesko and E. J. Vardaman, "Cost comparison for flip chip, gold wire bond, and copper wire bond packaging," in *2010 Proceedings 60th Electronic Components and Technology Conference (ECTC)*, pp. 10–13, 2010.

[7] S. Seal, M. D. Glover, A. K. Wallace, and H. A. Mantooth, "Flip-chip bonded silicon carbide mosfets as a low parasitic alternative to wire-bonding," in *2016 IEEE 4th Workshop on Wide Bandgap Power Devices and Applications (WiPDA)*, pp. 194–199, 2016.

[8] C. Zhong, S. He, M. Song, J. Wu, F. You, T. Qi, and C. Li, "Study of harmonic control power amplifier technology based on improved modeling of bondwire," *International Journal of RF and Microwave Computer-Aided Engineering*, vol. 32, no. 10, p. e23317, 2022.

[9] W. Eisenstadt and Y. Eo, "S-parameter-based ic interconnect transmission line

characterization," *IEEE Transactions on Components, Hybrids, and Manufacturing Technology*, vol. 15, no. 4, pp. 483–490, 1992.

[10] F. Alimenti, P. Mezzanotte, L. Roselli, and R. Sorrentino, "Modeling and characterization of the bonding-wire interconnection," *IEEE Transactions on Microwave Theory and Techniques*, vol. 49, no. 1, pp. 142–150, 2001.

[11] I. Ndip, A. Öz, S. Guttowski, H. Reichl, K.-D. Lang, and H. Henke, "Modeling and minimizing the inductance of bond wire interconnects," in *2013 17th IEEE Workshop on Signal and Power Integrity*, pp. 1–4, 2013.

[12] A. L. Nazarian, L. F. Tiemeijer, D. L. John, J. A. van Steenwijk, M. de Langen, and R. M. T. Pijper, "A physics-based causal bond-wire model for rf applications," *IEEE Transactions on Microwave Theory and Techniques*, vol. 60, no. 12, pp. 3683–3692, 2012.

[13] T.-P. Wang and Y.-F. Lu, "Fast and accurate frequency-dependent behavioral model of bonding wires," *IEEE Transactions on Industrial Informatics*, vol. 13, no. 5, pp. 2389–2396, 2017.

[14] H. Xue, C. R. Benedik, X. Zhang, S. Li, and S. Ren, "Numerical solution for accurate bondwire modeling," *IEEE Transactions on Semiconductor Manufacturing*, vol. 31, no. 2, pp. 258–265, 2018.

[15] Özlem Baştüzel Çakmak, "Modeling of gan power transistor package for design of broadband high-power amplifier," February 2022. Available at `https://open.metu.edu.tr/bitstream/handle/11511/96366/%C3%96zlem%20BA%C5%9ET%C3%9CZEL%20%C3%87AKMAK_1875814_Master_Thesis.pdf`.

[16] M. Umar, M. Laabs, N. Neumann, and D. Plettemeier, "Bondwire model and compensation network for 60 ghz chip-to-pcb interconnects," *IEEE Antennas and Wireless Propagation Letters*, vol. 20, no. 11, pp. 2196–2200, 2021.

[17] I. Ndip, A. Öz, H. Reichl, K.-D. Lang, and H. Henke, "Analytical models for calculating the inductances of bond wires in dependence on their shapes, bonding parameters, and materials," *IEEE Transactions on Electromagnetic Compatibility*, vol. 57, no. 2, pp. 241–249, 2015.

[18] S. California State University, "An introduction to hfss: Fundamental principles, concepts, and use." https://athena.ecs.csus.edu/~milica/EEE212/HAND/HFSSintro.pdf.

[19] T. Schmaltz, *Molecular Order in P- and N-Type Self-Assembled Monolayer Field-Effect Transistors*. PhD thesis, 01 2015.

[20] MACOM, "Macom, "75 w, 6.0 ghz, gan hemt die," cghv60075d5 datasheet." https://cdn.macom.com/datasheets/CGHV60075D.pdf.

[21] MACOM, "Macom, "25 w, 6.0 ghz, gan hemt die," cg2h40025 datasheet." https://cdn.macom.com/datasheets/CG2H40025.pdf.

[22] A. Packaging, "Die attach - advanced packaging." https://advpackaging.co.uk/die-attach.

[23] F. Schnieder, F.-J. Schmückle, W. Heinrich, and M. Rudolph, "An analysis of source connections in gan power transistor packages," in *2012 The 7th German Microwave Conference*, pp. 1–4, 2012.

[24] MACOM, "Macom, "maap-011106 power amplifier, 71-86 ghz" maap-011106 datasheet." https://www.macom.com/products/product-detail/MAAP-011106.

[25] MACOM, "Macom, "maap-011205 power amplifier, 71-86 ghz" maap-011205 datasheet." https://www.macom.com/products/product-detail/MAAP-011205.

[26] ANSYS-Q3D, "Ansys q3d extractor multiphysics parasitic extraction analysis." https://www.ansys.com/products/electronics/ansys-q3d-extractor.

[27] S. Y. Çekiç, A. Ergen, and A. Tunç, "The performance effects of bondwire characteristics up to mmwave frequencies," in *2021 23rd European Microelectronics and Packaging Conference  Exhibition (EMPC)*, pp. 1–4, 2021.

[28] I. Bahl, *Lumped Elements for RF and Microwave Circuits*. ARTECH HOUSE, 2003.

[29] H. H. Stephen and L. H. Howard, *Appendix E: Causal Relationship between Skin Effect Resistance and Internal Inductance for Rough Conductors*, pp. 649–651. John Wiley  Sons, Ltd, 2009.

[30] CMi, "Tpt hb10 wire bonder guidelines." https://www.epfl.ch/research/facilities/cmi/wp-content/uploads/2020/04/HB10_guidelines.pdf.

[31] C. R. Paul, "Introduction," [48], ch. 1, pp. 1–12.

[32] C. R. Paul, ""loop" inductance vs. "partial" inductance," [48], ch. 7, pp. 307–309.

[33] A. E. Ruehli, "Inductance calculations in a complex integrated circuit environment," *IBM Journal of Research and Development*, vol. 16, no. 5, pp. 470–481, 1972.

[34] C. L. Holloway, E. F. Kuester, A. E. Ruehli, and G. Antonini, "Partial and internal inductance: Two of clayton r. paul's many passions," *IEEE Transactions on Electromagnetic Compatibility*, vol. 55, no. 4, pp. 600–613, 2013.

[35] C. R. Paul, "The concept of "partial" inductance," [48], ch. 5, pp. 196–202.

[36] JEDEC, "Bond wire modeling standard." https://www.jedec.org/sites/default/files/docs/JESD59.PDF.

[37] F. Capelli and J.-R. Riba, "Analysis of formulas to calculate the ac inductance of different configurations of nonmagnetic circular conductors," *Electrical Engineering*, vol. 99, pp. 827 – 837, 2016.

[38] C. R. Paul, "The concept of "loop" inductance," [48], ch. 4, pp. 155–158.

[39] *Appendix E: Causal Relationship between Skin Effect Resistance and Internal Inductance for Rough Conductors*, pp. 649–651. John Wiley  Sons, Ltd, 2009.

[40] M. Darmi, L. Cherif, J. Benallal, R. Elgouri, and N. Hmina, "Integrated circuit conception: A wire optimization technic reducing interconnection delay in advanced technology nodes," *Electronics*, vol. 6, no. 4, 2017.

[41] C. Paul, *Analysis of Multiconductor Transmission Lines*. IEEE Press, Wiley, 2007.

[42] O. Gatous and J. Filho, "A new formulation for skin-effect resistance and internal inductance frequency-dependent of a solid cylindrical conductor," in *2004 IEEE/PES Transmision and Distribution Conference and Exposition: Latin America (IEEE Cat. No. 04EX956)*, pp. 919–924, 2004.

[43] F. Alimenti, U. Goebel, and R. Sorrentino, "Quasi static analysis of microstrip bondwire interconnects," *Proceedings of 1995 IEEE MTT-S International Microwave Symposium*, pp. 679–682, 1995.

[44] J. Chani-Cahuana, C. Fager, and T. Eriksson, "Lower bound for the normalized mean square error in power amplifier linearization," *IEEE Microwave and Wireless Components Letters*, vol. 28, no. 5, pp. 425–427, 2018.

[45] X. Ding and L. Zhang, "A high-efficiency gaas mmic power amplifier for multi-standard system," *IEEE Microwave and Wireless Components Letters*, vol. 26, no. 1, pp. 55–57, 2016.

[46] Y. Sun, X. Kang, Y. Zheng, J. Lu, X. Tian, H. Wu, W. Wang, K. Wei, X. Liu, K. Zhang, and G. Zhang, "Review of the recent progress on gan-based vertical power schottky barrier diodes (sbds)," *Electronics*, vol. 8, p. 575, 05 2019.

[47] L. Cupido, "Some wire bonding...." `https://www.qsl.net/ct1dmk/wbond_ex.html`.

[48] C. R. Paul, *Inductance: loop and partial*. John Wiley & Sons, 2011.

[49] Z. Xu, "A kind of potential practical sensors of metamaterial in electromagnetic flaw nondestructive testing," *Engineering*, vol. 3, no. 7, pp. 750–754, 2011. DOI:10.4236/eng.2011.37090.

# Appendix A

## HFSS SETUP

- Create Model Geometry

  HFSS offers three main solution types: Driven Modal, Driven Terminal Mode, and Eigenmode. The Driven Modal approach is often used to simulate passive high-frequency structures such as microstrips and waveguides. It specifically focuses on obtaining S-matrix findings, which quantify incident and reflected powers. On the other hand, the Driven Terminal Mode is used for signal integrity simulations that include multi-conductor transmission lines. It provides S-matrix findings in terms of terminal voltages and currents. The Eigenmode solver is a computational tool that is used to identify resonances and eigenmodes of structures. It provides information on the resonance frequencies and the accompanying field distributions.

- Assign Boundaries

  In HFSS, boundaries are critical for defining whether a model is open or enclosed. Closed models, such as cavity resonators or waveguides, confine energy within a structure and allow it to exit only through designated ports. Open models, like antennas or PCBs, permit energy to radiate freely. Boundaries also simplify the geometric and electromagnetic complexity of models by applying them internally or on symmetrical planes. Proper implementation of Conducting, Radiation, or Perfectly Matched Layer (PML) boundaries on all external surfaces is essential for accurately characterizing the model's behavior. [18].

  There are twelve boundaries in HFSS, but the most commonly used ones are PEC boundary and Radiation boundary:

  - PEC Boundary:

By default, in HFSS, all outside surfaces are assigned a perfect electric conductor (PEC) boundary condition since they are surrounded by the backdrop object that encompasses the whole solution space. The backdrop object, characterized as an ideal conductor, guarantees that no fields are computed within it. HFSS automatically populates any unoccupied areas inside the solution volume with Perfect Electric Conductor (PEC) material. The PEC boundary has multiple functions. It can create symmetry planes where the electric field components are perpendicular to the surface. It is applicable to 2D sheet objects made of lossless conductors, such as transmission line traces or patch antenna elements. Additionally, it can simulate infinite ground planes for antennas, thereby improving modeling accuracy [18].

- Radiation Boundary:

  A radiation boundary is used to simulate an open problem that allows waves to radiate infinitely far into space, such as antenna designs. HFSS absorbs the wave at the radiation boundary [49].

- Assign Excitation

  The most commonly used excitation types in HFSS are the wave port and lumped port. These ports provide field data and parameters such as S, Y, and Z parameters.

  - Wave Port

    A wave port is used to specify the location at which energy is introduced or extracted from the solution space. This product is particularly designed for optimal transmission lines and should only be applied to the external surfaces of the solution volume. The wave port offers characteristics such as S, Y, Z parameters, characteristic wave impedance, and propagation (gamma) and attenuation constants. The frequency-dependent characteristic wave impedance of the port is used to generalize and normalize the S-parameters produced by a wave port. HFSS computes the gamma value during port analysis, enabling the adjustment of findings by including or removing the length of the transmission line in the model. This modification therefore alters the S-matrix. In addition, it is necessary for the user to

establish an integration line inside the wave port. The integration line not only enables the computation of the voltage-based wave impedance on the transmission line, but also functions as a phase reference. So, the Wave port give the user ability of deembedding, as an example both integration line and deembedding is shown in Figure A.1.

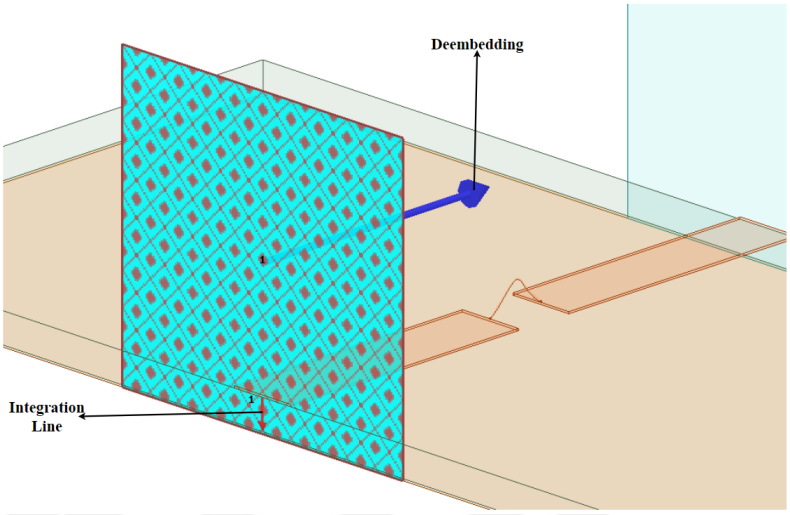



Figure A.1: Visualization of Integration Line and Deembedding for Waveport

One of the most important issue about wave port is size. The proper sizing limit is given in Figure A.2 [18].

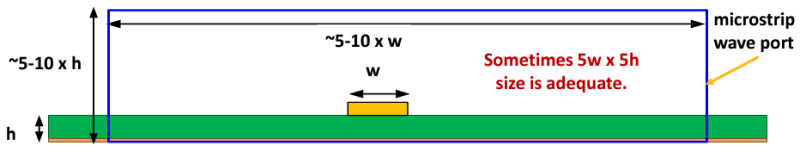



Figure A.2: Proper Waveport Sizing [18]

– Lumped Port:

In HFSS, lumped ports are used to provide internal energy sources in simulations and are simpler to design than wave ports, however they provide less detailed information. The S, Y, and Z parameters and fields are generated by them, but, no gamma or wave impedance data is included. Consequently, it is not feasible to extract the findings from their embedded state,

but it is conceivable to normalize them. Lumped ports are limited to a single mode and may be assigned to any 2D object that has edges touching two conductors. Edges that do not conduct electricity are given a perfect H boundary, which guarantees that there is no electric field perpendicular to the edge. When establishing a lumped port, it is necessary to create an integration line connecting the midpoint of the edges that come into contact with metal objects. In the figure below A.3, a lumped port setup is shown.

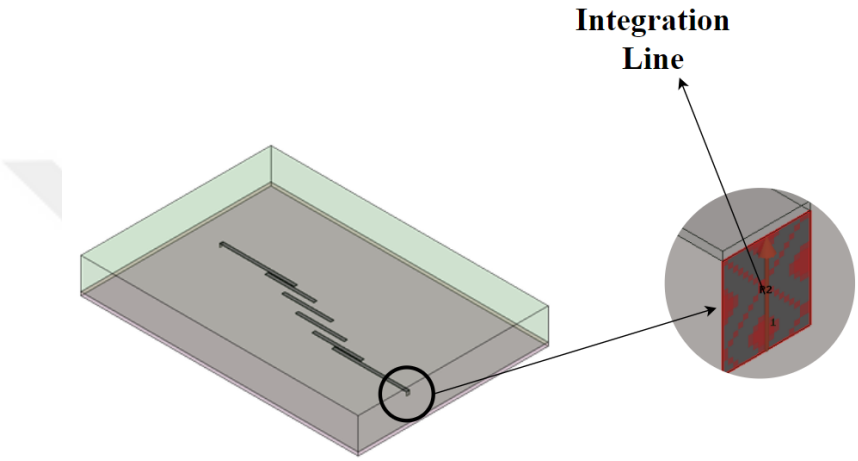



Figure A.3: Lumped Port Visualization

As a result, to compare wave port and lumped port, Table A.1 can be used.

Table A.1: Comparison of Wave Port and Lumped Port

| **Port** | **Applied** | **Gamma** | **Yields S,Y,Z** | **Renormalize** | **Deembedding** |
|---|---|---|---|---|---|
| **Wave** | Externally | Yes | Yes | Yes | Yes |
| **Lumped** | Internally | No | Yes | Yes | No |

- Setup The Solution
  - Solution Frequency Setting

    In HFSS, the solution frequency is the frequency at which simulations are explicitly solved, and model convergence is determined by the fields at

this frequency. The device's operating frequency should be used as the solution frequency. For frequency sweeps, the solution frequency should be set to the device's operating frequency, the center frequency of the sweep, or a frequency between 60 and 80 percent of the maximum desired frequency, depending on the type of sweep being used. The setting screen for frequency is shown in Figure A.4 with a red box.

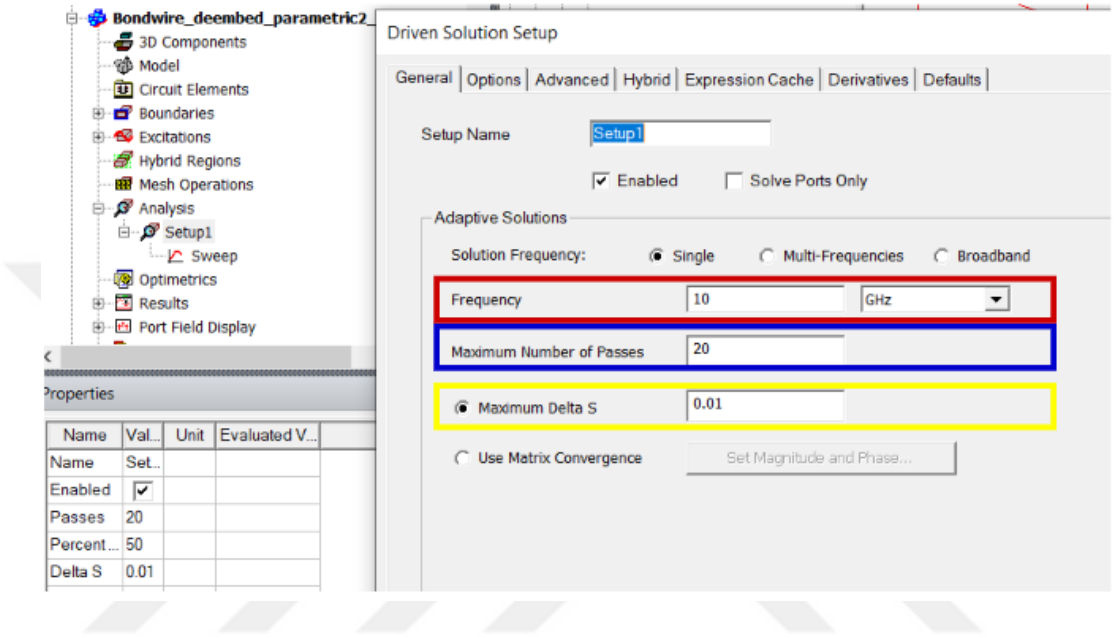



Figure A.4: Solution Setup for HFSS

– Delta-S Setting

  The adaptive process in HFSS ensures accurate results by correlating the electric fields in a simulation with the computed S-matrix. Convergence is assessed using the delta-S value, which measures the change in magnitude of the S-parameters between iterations. The simulation concludes when the magnitude of all changes in the S-parameters falls below the specified delta-S value, indicating convergence. If this criterion is not met, HFSS continues the simulation until the maximum number of passes is reached. Typically, delta-S values are set between 0.005 and 0.01 for most simulations [18]. It is shown with an yellow box in Figure A.4.

– The Maximum Number Of Pass and Maximum Refinement Per Pass

  In the adaptive solution process of HFSS, both the refinement percent-

age and the number of adaptive passes are used. The refinement percentage limits the number of tetrahedra that can be subdivided per pass. The maximum number of adaptive passes sets the limit on how many times the mesh will be refined to achieve convergence. This setting is shown in Figure A.4 with a blue box. The adaptive solution process is guided by delta-S, maximum refinement per pass, and the maximum number of passes to ensure convergence. The process is stopped when convergence is reached or when the maximum number of passes has been completed. If convergence is not achieved within the allowed passes, increasing the number of passes is recommended.

– Sweep Setup

HFSS offers three sweep types: discrete, fast, and interpolating. The fast sweep generates full-field solutions over a specified frequency range and is ideal for sharp resonances. It allows post-processing at any frequency within the range. The interpolating sweep estimates the S-matrix over a frequency range by solving at selected points until an error tolerance is met, It is used less RAM than the fast sweep, and It is suitable for broadband sweeps. However, it provides field data only at the solution frequency for post-processing. The discrete sweep generates explicit field solutions at specific frequency points, providing the most accurate results but requiring more time as the number of frequency steps increases. The type of the sweeps and range is shown in Figure A.5.

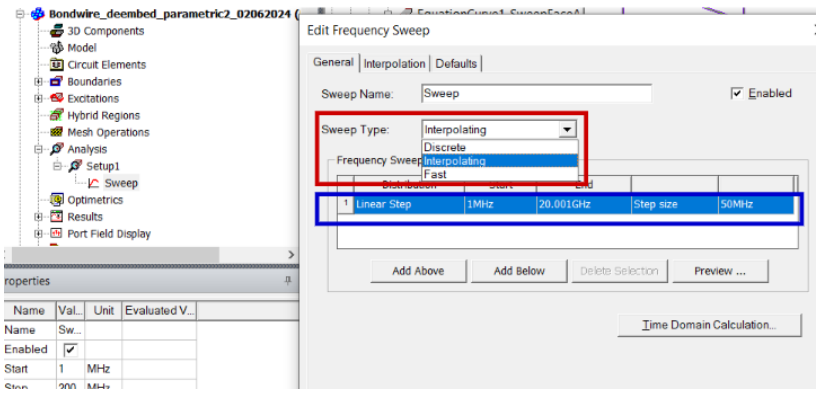



Figure A.5: Sweep Setup for HFSS

- Solve and Post Process The Results

  In HFSS, after creating setup and solving the geometry, as a post process, Scattering parameters (S21 and S11) can be plotted and exported. S21 gives the information about bond-wire inductance. This will help to understand what to do while creating a compensation or matching network for a die transistor.

  Also, after solution, distributed fields and meshing over geometry can be plotted.

# Appendix B

## Q3D SETUP

Steps to follow in Q3D for 3D simulations:

- Excitation

  After creating the geometry, a signal path is needed to be defined as a net. For a bond-wire geometry, the wire itself is assigned as signal net, shown in Figure B.1. In Q3D, a net is composed of source side and sink side. In the Figure B.1, two end of the signal net, the bond-wire, is chosen as source and sink. Also, the ground plane of the PCB is assigned as ground net.

  If there are two or more signal path, Q3D also has an ability of simulating mutual inductance between wires and ground plane.

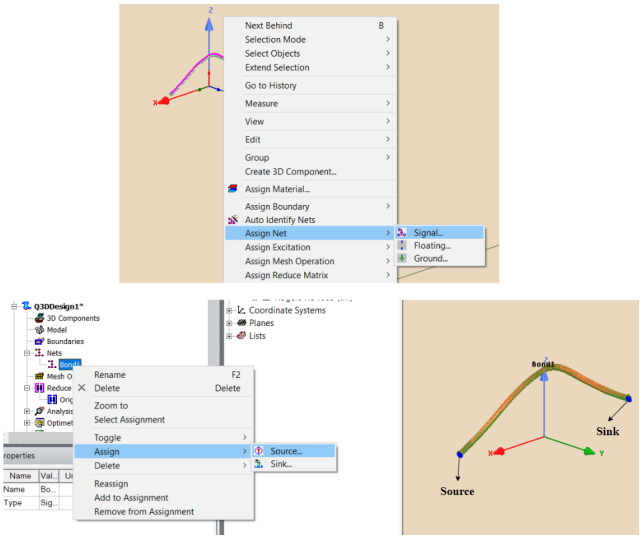



Figure B.1: Defining excitation in Q3D

- Setup The Solution

Like HFSS, in Q3D, a center frequency that solution will be done is set. Which of the capacitance, inductance and resistance will be solved are selected in the red box in Figure B.2. In the yellow box shown in Figure B.2, maximum number of passes, minimum number of passes, minimum converged passes, percent error and percent refinement pass are chosen.

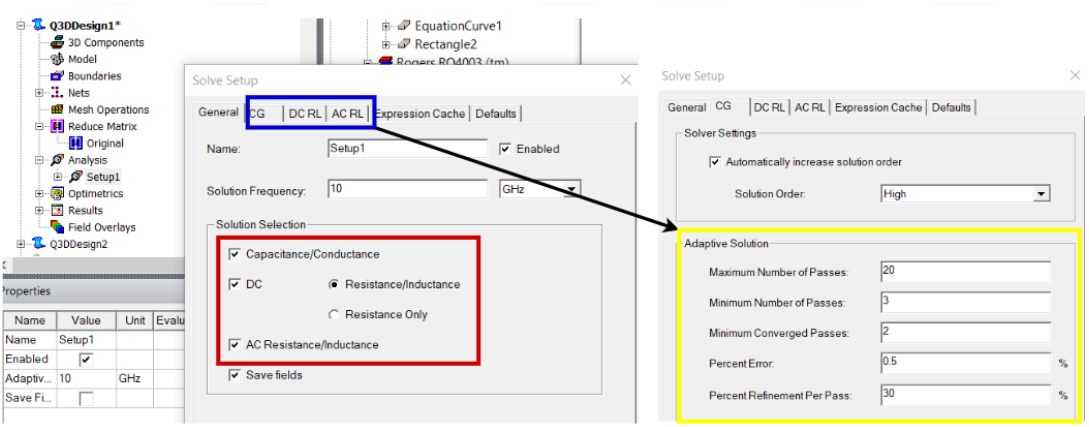



Figure B.2: Setup in Q3D

- Results Screen

After computing the solution, DC R, L, C and AC R, L and Mutual inductance can be plotted or exported using the screen in Figure B.3.

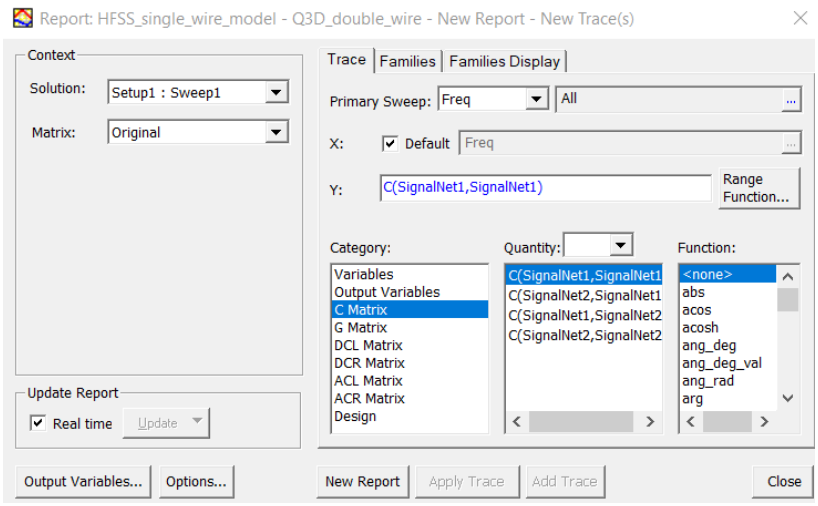



Figure B.3: Result Screen in Q3D

## Appendix C

## CAUSAL RELATIONSHIP BETWEEN RESISTANCE AND INTERNAL INDUCTANCE

The causal relationship between skin effect resistance, $R_{\text{AC}}$, in copper and internal inductance, $L_{\text{internal}}$, is investigated by first examining the surface impedance equation described in the Equation (C.1) [39].

$$Z_s(w) = R_{AC}(w) + jwL_{internal}(w) \tag{C.1}$$

For causality to be established, it is required that the function, $h(t)$ be zero for all negative times. So, the causality condition for the function:

$$h(t) = h_e(t) + sgn(t)h_e(t) \tag{C.2}$$

If Fourier Transform of $h(t)$ is $H(w)$, then Fourier transform of the Equation (C.3 is given below [39]. $\widetilde{H}_e(w)$ is defined as the Hilbert transform of the even component.

$$H(w) = H_e(w) - j\widetilde{H}_e(w) \tag{C.3}$$

Similarity between the Equations (C.1) and (C.3) leads to $H_{\text{e}}(w)$ = $R_{\text{AC}}$ and $\widetilde{H}_e(w)$ = $-wL_{\text{internal}}$. So, internal inductance implies that it is Hilbert transform of $\widetilde{R}_{\text{AC}}/w$

$$L_{internal}(w) = \frac{-\widetilde{R}_{AC}(w)}{w} \tag{C.4}$$

Therefore, if resistance of such a system is known, then, internal inductance o the system can be found by solving the Hilbert Transform relationship. This process is decribed in [39]. There are 2 ways to solve it: solve the Hilbert transform integral directly or use FFT and inverse FFT by applying Cauchy Principle [39].

At the end, high frequency internal inductance of a rough conductor is found by the Equation (C.5) for skin depth is lower than conductor thickness [39].

$$L_{internal}(w) = \frac{R_{AC}}{w} \tag{C.5}$$